

Ss. Cyril and Methodius University in Skopje



FACULTY OF MECHANICAL ENGINEERING - SKOPJE



Marija Lazarevikj

MODEL FOR DETERMINING THE INFLUENCE OF A VARIABLE-SPEED  
FRANCIS TURBINE ON GUIDE VANE STRUCTURAL AND STRESS  
PARAMETERS

-Doctoral Dissertation-

SKOPJE, 2022

Supervisor:

Prof. Zoran Markov, Ph.D.  
Faculty of Mechanical Engineering-Skopje  
Ss. Cyril and Methodius University in Skopje

Committee members:

Prof. Zoran Markov, Ph.D.  
Faculty of Mechanical Engineering-Skopje  
Ss. Cyril and Methodius” University in Skopje

Prof. Valentino Stojkovski, Ph.D.  
Faculty of Mechanical Engineering-Skopje  
Ss. Cyril and Methodius University in Skopje

Prof. Zlatko Petreski, Ph.D.  
Faculty of Mechanical Engineering-Skopje  
Ss. Cyril and Methodius University in Skopje

Prof. Darko Babunski, Ph.D.  
Faculty of Mechanical Engineering-Skopje  
Ss. Cyril and Methodius University in Skopje

Prof. Ole Gunnar Dahlhaug, Ph.D.  
Norwegian University of Science and Technology  
Trondheim

Date of public defense:

20.05.2022

TECHNICAL SCIENCE – MECHANICAL ENGINEERING

MARIJA LAZAREVIKJ, M.Sc. Mech. Eng.

## MODEL FOR DETERMINING THE INFLUENCE OF A VARIABLE-SPEED FRANCIS TURBINE ON GUIDE VANE STRUCTURAL AND STRESS PARAMETERS

### ABSTRACT:

The hydrodynamic conditions at the runner entrance depend to a large extent on the guide vanes system. Conducting experiments provides an opportunity to gain deeper knowledge about the water flow and the forces arising from it, which act on the blades. The numerical model for flow through the radial cascade segment is validated by verifying the results of simulations by comparing them with the experimentally obtained results. Relations between the forces distribution of a solitary airfoil and a cascade profile are derived based on parametrization.

The effect of the change in the runner speed on the blade pressure distribution is determined through a two-dimensional model. The unsteady fluid flow model enables the determination of pressure pulsations, ie consideration of dynamic loads at different runner speeds. The results and findings from these studies are in favor of determining the impact of speed on the strength condition of the blade. Parametrization of the guide vane torque is performed. Two approaches are presented to calculate the most favorable position of the guide vane axis of rotation, which show a reduction of torques and consequently minimization of loads under different operating conditions of the guide vanes system. The second approach is implemented in software for Computational Fluid Dynamics (CFD) and Finite Element Analysis (FEA), which establishes a methodology for developing an appropriate design with regard for the strength parameters.

### KEYWORDS:

Guide vanes, variable speed, loads, CFD, FEA

*”If you want to find the secrets of the universe, think in terms of energy, frequency and vibration”.*

*Nikola Tesla*

*Dedicated to my grandmother  
Prof. Dr. Marija Lazarevikj for  
her endless love, support and  
motivation.*

## Acknowledgement

I would like to express my deepest gratitude to my supervisor Prof. Dr. Zoran Markov for all the guidance, support, and trust he provided me with throughout this challenging work. Being part of the HydroFlex project was a great experience which highly contributed to my professional development.

I would like to express my sincere gratitude to the president of the evaluation committee, Prof. Dr. Valentino Stojkovski, for his valuable advice and shared knowledge. I would also like to thank the Committee members, Prof. Dr. Darko Babunski and Prof. Dr. Zlatko Petreski for their helpful advice and access to their professional experience. I would especially like to extend my appreciation and gratitude to Prof. Dr. Ole Gunnar Dahlhaug for his guidance and fruitful discussions during our collaboration.

I am also expressing my gratitude to my colleagues from the Faculty of Mechanical Engineering – Skopje who supported me in my work.

Special thanks to Dr. Igor Iliev and Dr. Chirag Trivedi for our collaboration in the framework of HydroFlex through exchanging ideas, especially during my study visit of NTNU.

Following this path was a lifetime experience which would not be possible without the patience and support from my family who were always there to encourage me. Also, thanks to my friends who were always there to motivate me and understand me.

This doctoral dissertation is realized within the project HydroFlex which is funded by the research and innovation programme of the European Union Horizon 2020 according to the grant agreement no. 764011.



This project has received funding from the European Union's Horizon 2020 research and innovation programme under grant agreement No 764011



# Contents

Acknowledgement .....	5
List of Symbols .....	9
1 Introduction .....	11
2 Literature review of previous relevant scientific research.....	15
2.1 Pressure distribution.....	15
2.1.1 <i>Theoretical research</i> .....	15
2.1.2 <i>Numerical research</i> .....	15
2.1.3 <i>Experimental research</i> .....	16
2.2 Guide vane torque and relation to its rotation axis.....	16
2.3 Fluid-structure interaction.....	17
2.4 Rotor-stator interaction (RSI).....	18
3 Theoretical foundations .....	20
3.1 Aerofoil and radial cascade of aerofoils – concept, basic geometric parameters	20
3.1.1 Concept of aerofoil, basic geometric parameters .....	20
3.1.2 Cascades of aerofoils.....	21
3.2 Flow around solitary aerofoil and cascade of aerofoils. Forces acting on a solitary aerofoil and aerofoil in a cascade.....	22
3.2.1 Forces that acting on a solitary aerofoil and aerofoil in a cascade.....	22
3.2.2 Influence of aerofoil cascade parameters on pressure distribution (forces)..	25
3.2.3 Model for calculating forces and moments acting on an aerofoil .....	27
3.3 Forces and moments acting on the blade of a guide vane system.....	29
3.3.1 Stationary radial cascade of hydrofoils – guide vane system.....	29
3.3.2 Forces and moments acting on the blade of a closed guide vane system.....	30
3.3.3 Forces and moments acting on the blade of open guide vanes .....	33
3.4 Guide vane stress distribution .....	36
3.4.1 Calculation of guide vane stresses .....	36
3.4.2 Rotor-stator interaction .....	37
4 Experimental research .....	39
4.1 Description of an experimental system for analysis of air flow around a profile placed in a circular cascade.....	39
4.1.1 Channel.....	39
4.1.2 Measuring section with a circular cascade of profiles .....	40
4.2 Measurement of flow technical parameters .....	42
4.2.1 Measuring the pressure.....	42
4.2.2 Flow measurement .....	45

4.3	Results of profile pressure distribution measurements. Determination of forces, moments, and attack point of the resulting force .....	50
4.3.1	Solitary aerofoil.....	51
4.3.2	Aerofoil in a radial cascade.....	56
5	Numerical research.....	72
5.1	Numerical modelling of flow around a solitary profile in a wind tunnel.....	72
5.2	Numerical modelling of the flow around the profile-blade in a radial cascade ..	74
5.2.1	Radial cascade with density $t/L > 1$ .....	75
5.2.2	Radial cascade with density $t/L < 1$ .....	76
5.3	Numerical modelling of fluid flow in Francis turbine guide vane system at different runner rotating speeds .....	77
5.3.1	Development of a 2D numerical model .....	77
5.3.2	Influence of inlet conditions on guide vane pressure distribution .....	81
5.3.3	Analysis of the runner blade position and variable speed influence on guide vane pressure distribution – quasi-steady conditions.....	84
5.4	Numerical modelling of unsteady flow through guide vanes at different runner speeds	87
5.4.1	Inlet conditions – guide vane inlet and outlet velocity variation .....	87
5.4.2	Guide vane torque pulsations .....	88
5.4.3	Guide vane pressure pulsations.....	94
5.4.4	Guide vane strength conditions .....	97
6	Guide vane strength analysis .....	99
6.1	Interaction between a fluid and a solid.....	99
6.2	Influence of the axis of rotation on the guide vane torque and static loads .....	99
6.2.1	Three-dimensional numerical model of flow through guide vanes.....	99
6.3	Influence of the guide vane axis of rotation on the torque.....	100
6.3.1	Selection of guide vane rotation axis position .....	103
6.3.2	Impact of rotation axis on the guide vane static loads .....	106
6.4	Influence of variable speed on static loads of the blade.....	108
6.5	Automated software implementation .....	110
7	Spiral casing hydraulic design.....	112
7.1	Introduction .....	112
7.1.1	Spiral casing in hydraulic turbines .....	112
7.1.2	Brief literature review of previous scientific research in the area of spiral casing design	112
7.2	Spiral casing hydraulic design methodology .....	113

7.2.1	Calculation methodology .....	113
7.2.2	Basics of the hydraulic design.....	115
7.3	Validation of the spiral casing hydraulic design .....	118
8	Conclusions and recommendations for further work .....	122
	References.....	127
	APPENDIX.....	131

## List of Symbols

Symbol	Measure unit	Description
$g$	$[m/s^2]$	Gravitational acceleration
$\rho$	$[kg/m^3]$	Density
$\mu$	$[Pa \cdot s]$	Dynamic viscosity
$\pi$	$[-]$	Mathematical Constant
$\omega$	$[rad/s]$	Angular Velocity
$n$	$[min^{-1}]$	Runner rotational speed
$Q$	$[m^3/s]$	Discharge
$H$	$[m]$	Net head
$x, y, z$	$[-]$	Coordinates
$t$	$[s]$	Time
$v$	$[m/s]$	Velocity
$p$	$[Pa]$	Pressure
$\Gamma$	$[m^2/s]$	Circulation
$R$	$[m]$	Radius
$D$	$[m]$	Diameter
$u$	$[m/s]$	Peripheral velocity
$F$	$[N]$	Force
$M$	$[Nm]$	Torque
$P$	$[W]$	Power
$\eta$	$[-]$	Efficiency
$\alpha$	$[^\circ]$	Aerofoil angle of attack
$\varepsilon$	$[-]$	Turbulence dissipation rate
$k$	$[^\circ]$	Turbulence kinetic energy
$L, l$	$[m]$	Length
$Z_{rv}$	$[-]$	Number of runner blades
$t_o$	$[m]$	Cascade pitch
$a_o$	$[m]$	Guide vane opening
$A_1, B_2$	$[-]$	Constants
$p$	$[Pa]$	pressure
$Sh$	$[-]$	Strouhal number
$f$	$[Hz]$	Frequency
$T$	$[s]$	(Wave) Period
$A$	$[m]$	Amplitude
RMS		Root mean square
PtP		Peak-to-Peak

CFD  
FSI  
FEM  
GV

Computational Fluid Dynamics  
Fluid-Structure Interaction  
Finite element method  
Guide vane

# 1 Introduction

In order to deal with climate change by reducing carbon dioxide emissions, the global and European energy systems have begun to shift to producing energy exclusively from sustainable and renewable sources. However, this transformation towards achieving the dominance of renewable energy sources over fossil fuels faces challenges arising from the instability of solar and wind energy sources that are not always able to meet the current energy demand.

Thanks to the rapid response to variable demand, hydropower plants can balance the supply of energy from intermittent renewable sources and thus contribute to the stabilisation of the electricity grid [1]. At the same time, hydropower is the largest and most economical renewable energy source in the world, with a tendency to remain the most competitive and fastest-growing technology due to the great technical potential that is available and can be used [2]. Therefore, the interest in hydropower is growing and the focus is on increasing the energy conversion efficiency, saving energy, and enhancing reliability and longevity of the equipment.

The highest energy efficiency is achieved at the optimal operating point of the turbine, defined by certain values of head and discharge [3]. But to meet the given energy demand, hydraulic turbines often operate outside the optimal operating point, which causes reduced efficiency and higher dynamic loads and stresses of the components, and the occurrence of vibrations. Since such variable loads can cause material breakdown (mechanical damage), there is a need for in-depth knowledge of the mechanical behaviour of turbine elements in different operating modes [4], [5].

Reducing dynamic loads and increasing turbine efficiency are the main goals of hydropower leading to the development of variable speed technology that would overcome such problems [6], [7]. Variable speed turbine operation is first implemented in reversible pump turbines that are typically designed and optimised to operate as pumps while operating in turbine mode with a lower efficiency. For higher efficiency in both operating modes, an adaptation of the speed of the machine itself was used [8].

The hydro-generating unit consists of a turbine connected to an electric generator. In a turbine whose runner rotates, the energy of the water is converted into mechanical energy of the rotating shaft. The turbine shaft is connected to a generator where mechanical energy is converted into electricity to supply consumers [9].

When the fluid interacts with the structural elements of the turbine, stresses occur that can lead to permanent deformation of the turbine components. The magnitude of the deformations depends on the pressure and velocity of the fluid and the properties of the material from which the turbine is made. If the deformations are small and almost constant over time, they will not significantly affect the fluid back and the focus can be shifted to the resulting stresses in the components, i.e. the analysis can be one-way.

Understanding the impact of water flow on the construction of turbines is of great importance due to the susceptibility of the turbine elements to loads caused by the fluid stream, which results in possible damage to the blades. In this regard, the safe operation of hydropower plants requires optimised turbine components in terms of loads. The hydrodynamic conditions at

the runner inlet largely depend on the guide vane system, which is a circular cascade of a certain number of blades. The function of the guide vane system is to regulate the flow of water and thus the power of the turbine, as well as to ensure the axisymmetric, even distribution of water in the runner with minimal energy losses and to create the necessary circulation at the runner inlet. By optimising the guide vane shape, as well as the location of its axis of rotation, satisfactory strength and minimal mechanical loads on the guide vane system can be achieved.

Conducting experiments provides an opportunity to get deeper knowledge of the fluid flow and the forces arising from it and acting on the blades. The main approach to studying the mechanical properties of turbines is based on a combination of computational and model tests. Given the cost of developing the model and establishing the necessary test conditions, it is often difficult to perform a large number of model tests.

Relatively fast computers with affordable prices and the development of specialised software have led to the emergence and rapid development of Computational Fluid Dynamics (CFD), the application of which significantly facilitates the study of fluid flow processes in hydraulic turbines and their static and dynamic characteristics.

The flow modelling of hydraulic turbines and the determination of their mechanical properties on the blades is a complex issue due to the need to address a number of interdependent factors. The real challenge is the complex approach to performance analysis and design optimisation, taking into account the hydraulic characteristics and strength performance of the guide vanes.

**The subject of the research** in this thesis is the stress analysis of the hydrofoil, through the influencing parameters during its operation in a circular cascade and especially when used in guide vanes of a variable-speed Francis turbine. The need for this analysis originates from the stator-rotor interaction of the guide vane and the turbine runner, with the aim to predict the guide vanes dynamic loads taking the emerging variable speed technology into account.

**The research goals** are focused on the determination of the correlation of the cascade geometry parameters, blade pressure distribution, rotational axis position, runner rotational speed, and the forces and torques as influencing stress parameters on the blade, using numerical and experimental investigations.

**The idea for the research in the doctoral dissertation** comes from participating in the project HydroFLEX (Increasing the value of hydropower through increased flexibility), in the framework of the Horizon 2020 program of the European Commission and led by the Norwegian University of Science and Technology in Trondheim (NTNU).

The doctoral dissertation is divided into eight chapters. After the short introduction of the thesis and definition of aims and research subject in the first chapter, the **second chapter** presents an overview of the up-to-date relevant achievements in the field, taking into account the theoretical, experimental and numerical research connected with the forces that have an effect on the guide vanes, the correlation of the vane shape and the pressure distribution on its surface. The variable speed of the runner on the stress performance of the guide vane system is investigated in order to present the situation with the current state-of-the-art.

The **third chapter** presents the theoretical background of the forces acting on a hydrofoil (both single and in cascade), with the added forces and torques on a guide vane, which represents a stationary circular blade cascade and the corresponding loads. The focus is aimed at the

influence of the cascade geometry parameters on the pressure distribution, the interaction between the guide vanes and the rotational runner blades behind them. The developed calculation model for determination of the forces and torques on the hydrofoil - taking into account the discrete pressure distribution around it - is presented, implementing the governing fluid flow laws.

The **fourth chapter** is dedicated to the conducted experimental research. The designed experimental test rig for measurements of the pressure distribution of a single hydrofoil and hydrofoil in a circular cascade segment is described. Details on the parts of the test rig – wind tunnel and measurement section are presented. The implemented methodology, the measurement system for the flow field parameters (pressure, flow velocity, and temperature), and the used measurement equipment are presented. Three procedures for defining the wind tunnel velocity profile and three approaches to discharge measurement using the experimental data are analysed. The concept on which the test rig is designed enables shock-free fluid flow on the hydrofoil when set as a part of the cascade for different cascade positions and with a free flow at the exit. The measurement data on the hydrofoil pressure distribution and their application on the developed model for force, torque, and point of attack calculations are shown. Based on all the acquired data, final conclusions on the influencing parameters on the pressure distribution, which are used for the stress analysis, are presented.

In the **fifth chapter**, the numerical investigations are presented, starting with the modelling of a single foil and a foil in a circular cascade. The development of a 2D numerical model for steady-state fluid flow analysis through a guide vane system is described. The initial conditions and the turbulence models are presented and the model validation using experimental data is performed. The numerical models involve analyses for quasi-steady-state conditions which indicate the influence of particular stationary turbine parts on the guide vane system. The discharge influence is taken into account using two different spiral case designs, the influence of the runner and the stator-rotor interaction and the relative positions of the stay vanes, as well as the influence of the runner variable speed on the guide vane pressure distribution. The focus of the unsteady flow investigations is set on the numerical results that take into account the different rotational speeds of the runner and its influence on the forces and torques on the guide vanes as a circular cascade. The dynamic conditions are defined for the rotor-stator interaction of the stationary guide vanes and rotational runner blades. The pressure variations trends in time depending on the rotational speed are discussed.

The guide vane stress analysis is presented in **chapter six**. The emphasis is set on the influence on the point (axis) of rotation and the vane loads using the results acquired from the 3D turbine model. The torque variation data led to an approach to determine the position of the rotational axis of the vane. The proposed methodology is implemented in a corresponding software code.

The **seventh chapter** describes the novel methodology that has been developed for the hydraulic design of the spiral casing (as a component of the Francis turbine that provides the inlet conditions for the guide vane system), with a priority for circular cross-sections and transition to elliptic cross-sections. The calculation method is validated by fulfilling the set hydraulic performances, and comparisons of the existing with the novel design are performed.

**Chapter eight** summarises the results, the applied techniques and methodologies, as well as the conclusions and recommendations for further work. Generic conditions for the loads on a hydrofoil are set, and the stress parameters are defined for fluid flow through a circular cascade used as a Francis turbine guide vane system. A detailed overview is given of the entire research and the corresponding results, stressing the scientific contribution, the possibilities for data application, and recommendations for further work.

## **2 Literature review of previous relevant scientific research**

### **2.1 Pressure distribution**

#### *2.1.1 Theoretical research*

The fluid flow around a hydrofoil in a cascade is closely related to the flow around the hydrofoil placed in an unlimited and uniform flow field. Therefore, the problem of finding the pressure distribution around the hydrofoil in a cascade or determining the appropriate shape of the hydrofoil to obtain a given pressure distribution comes down to the problem of solitary profile, which is solvable by applying already tested and validated methods.

Katzoff S. and other authors [10] developed a method for determining the pressure distribution of a hydrofoil in a cascade in the case of two-dimensional, incompressible and inviscid flow, taking into account the influence of the hydrofoil itself on other hydrofoils in the cascade through an iterative process. For a certain angle of attack, a solution is generated that is used for conformal transformation.

Allen J. H. and Spurr R. A. [11] [12] propose a method for determining the velocity (pressure) distribution of a given aerofoil with a slight curvature, but also for predicting the shape of the aerofoil at a predetermined velocity distribution. They determine the relationship between the aerofoil shape and the pressure distribution of the same aerofoil when set in a cascade, starting from the comparison between the pressure distribution for the aerofoil in a cascade and the solitary profile and independently treating the camber-line impact and the thickness distribution.

Bohle [13] describes a modification of an existing method of inverse cascade design, applying a finite boundary layer calculation by the finite difference method and applying the potential flow theory to determine the cascade geometry. The velocity distribution on the pressure side of the blade is attributed to achieving the set angles in front of and behind the cascade.

#### *2.1.2 Numerical research*

A method of inverse design of 2D and 3D linear cascades through which compressible fluid flows has been described and validated by Daneshkhan and Ghaly [14]. The ultimate goal is to obtain the required pressure distribution by modifying the initially generated geometry through an iterative process. The effectiveness of the proposed procedure has been proven by the successful redesign of compressor cascades and a turbine in which a certain pressure profile was desirable to reduce adverse effects.

Pascoa J. C. et al. [15] presented an improved variant of the method of inverse design of the blade in a cascade by iteratively modifying the blade shape until a predetermined pressure distribution was achieved. The calculation is performed numerically, so that with each iteration the cross-section of the blade is modified, a new grid is generated, and the flow field is solved. The algorithm for generating the blade is upgraded with an expression for the distribution of the thickness of the aerofoil that gives more realistic camber-lines.

Duan Y., Zheng Q. and Jiang B. [16] also applied CFD technology to implement the method of inverse design of the blade in a cascade. Milder loads on the blade, i.e. flattening the pressure profile which reduces the pressure losses in the cascade was successfully obtained by modifying the design.

### **2.1.3 Experimental research**

Dunavant J. C. and Erwin J. R. [17] experimentally examined cascade sections with 5 blades in a wind tunnel at different fluid inlet angles, at different operating modes, and at different cascade positions. Obtaining the required camber-line at a given input parameter and building the aerofoil through the well-known theoretical method of superimposing the thickness distribution of the middle camber-line was achieved. Experimental data were used to predict pressure distribution profiles.

Assassa G. and Ghany M. [18] performed experimental measurements of the pressure distribution of an isolated hydrofoil (NACA 0015) and a hydrofoil in a cascade under different flow conditions (different attack angles / different fluid flow inlet angles). Based on the theoretical methods, they developed a code for calculating the two-dimensional flow through the cascade whose results they compared with their experimental results, other experimental data, and other prediction methods, which showed the efficiency of the code for different flow conditions and cascades configurations. In this way, the relation between the geometric and aerodynamic parameters of the hydrofoil was reached. Additionally, they measured the velocity distribution behind the hydrofoils, concluding that it was symmetrical only at the zero position of the hydrofoil, while increasing the attack angle of the hydrofoil made the arrangement more asymmetric but becoming more uniform as the distance from the trailing edge of the hydrofoil increased [19].

## **2.2 Guide vane torque and relation to its rotation axis**

In a reversible pump-turbine, the flow is unsteady, primarily due to the viscous effects, i.e. the detachment of the boundary layer, the appearance of vortices and the rotor-stator interaction. Lipej A. [20] conducted a numerical analysis of the guide vanes' torques in a reversible pump-turbine in non-stationary flow mode. The analysis during operation in turbine mode was made for 6 openings of the guide vane system. The comparison between the numerical and experimental results shows the correlation between the minimum and maximum values of the torque and the amplitude of the torque oscillations, which is greater for unsteady flow because the effect of the interaction between the runner and the guide vane system is not negligible. For turbine mode, the torque oscillations are smaller and changing around an average value, which indicates that it can be considered stationary.

Schweiger F. and Gregori J. [21] performed experimental torque measurements on the guide vanes of Francis and Kaplan turbines, expressing the final results through the dimensionless moment coefficient. Their results show that the guide vane moment depends on the operating mode and the position of the blades in relation to the spiral casing. The measured moment for each blade was different, and the largest changes in the values were observed near the tooth of the spiral, i.e. from the spiral tooth to enveloping angle  $\varphi = 120^\circ$ . In addition to the blade shape, the position of the rotation axis significantly affects the moment. Guide vanes

located just behind the stay vane are less loaded. Larger changes in the moment coefficient are observed at larger openings. There is a higher coefficient of the moment at runaway speed rather than at other operating conditions. The maximum moment is when the guide vane system is closed. Under optimal operating conditions, there is a moment of self-closing, while at runaway there is a tendency to open the blades. It has been observed that in terms of dynamic characteristics, the oscillation of the moment value is 10 times greater at runaway speed than in optimal operating conditions.

Kovalev N. [22] used the experimentally obtained data on pressure distribution of symmetrical and asymmetrical guide vanes to determine the magnitude and direction of the hydrodynamic force and its point of attack for different openings of the guide vane system. It was concluded that the moment is the highest for a closed guide vane system; with its opening, the moment decreases to 0, then increases in the opposite direction, and then drops again to 0. Additionally, the study of 3 blade designs showed that the magnitude and direction of the moment depend on the blade position in relation to the spiral and the angle of the spiral tooth.

Muntean S. et al. [23] performed numerical optimisation of the position of the rotation axis of the Francis turbine guide vane. The introduced optimisation criterion means minimising the mechanical loads of the guide vane system by obtaining a minimum value of the extreme moment on the blade shaft. The conditions at 4 different positions of the rotation axis, including the existing one, are numerically examined. The developed methodology shows that there is an improvement compared to the original design, i.e. the newly selected guide vane rotation axis provides a smaller magnitude of the moment and less load on the structure. This is performed by obtaining the same absolute value of the extreme (minimum-negative and maximum-positive moment) moments.

Using the CFD software package, Devals and other authors [24] developed a fully automated numerical procedure for predicting guide vane moments. The automation of the spiral casing and guide vane system mesh generation, numerical simulation and data processing is achieved with the help of scripting. The standard  $k-\epsilon$  model of turbulence is applied. 2D and 3D stationary stream flow over a wider turbine operating range are considered (9 different guide vane openings and different turbine speeds, including runaway speed.). Two distributors with 20 and 24 guide vanes were tested. The results of the numerical simulations are consistent with the experimentally obtained results for the moment values of several selected guide vanes.

By experimental measurements, Qifei L. and other authors [25] determined the change in the moment of the pump-turbine guide vane at the opening in the range of 18.4 to 100%. Among the conclusions drawn are: consistency of the moment coefficient with increasing openness at minimum, nominal, and maximum net head. For openings less than 43%, the moment of the guide vane has a small intensity, and, at openings greater than 43%, it begins to gradually increase.

### **2.3 Fluid-structure interaction**

Budiman B. A. [26] and other authors used a software package for CFD calculation and analysis with a finite element method to predict static loads of guide vanes at different openings of a guide vane system with 16 blades. The specific case of static overload is also considered when an external object obstructs the rotational movement of the blades as a system defect. The

third case is the dynamic load at the moment of closing the guide vane system in the event of turbine failure. The guide vane has to overcome all cases. Based on the numerically obtained results for maximum moments and stresses, the appropriate blade material is selected. The strength analysis is performed on the blade-shaft system by setting the appropriate boundary conditions - fixing the bearings.

Several cases of runner blade breaking have contributed to increased interest in the investigation of dynamic loads in hydraulic turbines, the occurrence of which is mainly due to the interaction between the stator and the rotor [27]. Prediction of these impacts can be done experimentally and numerically. Previous research has focused on Francis turbine runners, while a small number have examined the impact of these phenomena on guide vanes.

Zobeiri A. and other authors [28] experimentally and numerically investigated the interaction between stationary parts and the rotor of a pump-turbine model with 20 stator blades, 20 guide vanes, and 9 runner blades. Because the intensity of the impact of this interaction depends on the distance between the guide vane and the runner blade, i.e. from the relative mutual placement, the most significant are the effects that would occur at the maximum openness of the guide vane system when the distance is the smallest and the trailing edge of the guide vane is closest to the runner blade; so, the tests are made only for this operating point. Measurements of (fluctuations of) pressure were made with 48 pressure sensors placed in the channels of the stay vanes and the guide vanes and in the zone between them. The numerical domain includes all the turbine elements in order to take into account the unevenness of the fluid flow coming from the spiral casing. The standard  $k$ - $\epsilon$  model of turbulence is used to simulate 3D unsteady flow. The results of the numerical calculation are compared with the experimental data obtained at the measuring points in the distributor channels and they are validated. The highest pressure amplitude is obtained at the point closest to the runner, which indicates the influence of the interaction between the guide vanes and the rotating blades.

The finite element method has also been applied by Myrvold [29] for strength analysis of a guide vane. Modal analysis was performed in air and water to obtain the modal shapes and natural frequencies of the blade. The natural frequency of the same mode in water compared to air is 11% lower due to the impact of the added mass. Additionally, an analysis was performed by applying pressure to the guide vane to calculate the deformations and the moment acting on the blade. The blade shaft with fixing in the bearings is also taken into account.

## **2.4 Rotor-stator interaction (RSI)**

In order to achieve the safety and security of the structural elements of the Francis turbine, it is important to predict the response to the frequencies caused by the flow. Pulsations with large amplitudes lead to blade fatigue and there is a danger of their breaking after a while. The amplitudes depend on the flow conditions, the type of turbine, and the number of blades of the guide vane system and the runner. The structural behaviour will also depend on the properties of the material, the natural frequencies, and the stiffness caused by the flow [30].

According to the numerical results of Laouari and Ghenaïet [31] who simulated the non-stationary flow through the Francis turbine by monitoring the pressure over time at several points, the interaction between the rotor and the stator can cause large pressure and moment oscillations, especially at small flows when the amplitude of the dominant frequencies is greater

than at the optimal operating point. The authors concluded that pressure fluctuations in the vaneless space also depend on the interactions between the runner and the diffuser. They also concluded that the RSI has an impact up to the runner. A similar conclusion is reached that the pressure oscillations caused by the interaction between the guide vane system and the runner spread to the trailing edge of the runner in the experimental and numerical studies of the high-pressure Francis turbine in its entire operating range by Trivedi et al. [32].

Pressure oscillations due to RSI in Francis turbine partial load mode are the subject of numerical analysis by Anup KC, Thappa B. and Lee Y. [33], who monitored pressure and moment variations over time at selected points in the channels on the guide vane system and the runner. They noticed periodicity in the change of the pressure distribution of the guide vanes, as well as in the change of the pressure distribution and the moment of the runner blades. The presence of one of the dominant frequencies corresponding to the number of guide vanes is confirmed by simulations.

Zhou and other authors [34] numerically analysed the pressure pulsations in the vaneless space between the guide vane system and the Francis turbine runner at 4 partial load operating modes. 3D unsteady flow through all elements of the turbine is modelled and simulated. Pressure oscillations are obtained at multiple monitoring points in the vaneless space. Their results show that the largest amplitude of the pressure oscillations in this space corresponds to the frequency of runner blade passing, while the next largest amplitude is the frequency of the vortex rope which indicates that the pressure wave originating from the vortex in the diffuser travels upwards in the runner and then in the vaneless space. The obtained pressure amplitudes in the monitoring points of the runner are of lower intensity than those in the diffuser. Also, there is not much difference between the pressure amplitudes in the vaneless space for different operating modes.

Iliev et al. [35] experimentally investigated the effect of the variable speed of a Francis turbine model on the reduction of pressure pulsations, which are measured in the guide vanes channels and in the vaneless space. The pressure amplitudes are the result of the interaction of the rotor and the stator during different operating modes. When operating a variable-speed turbine at the optimum curve, the amplitudes are less or the same as when operating a synchronous speed at an optimum drop for the entire range. The smallest pressure pulsations when working with synchronous speed are obtained at a 10% lower drop than the optimum, which indicates that, with a slight reduction in efficiency, the speed can be adjusted to have the smallest pressure fluctuations in the vaneless space.

Trivedi and other authors [36] have experimentally investigated the non-stationary phenomena of a Francis turbine model with varying runner speed. Characteristic frequencies and amplitudes of pressure over time are obtained at multiple measuring points in the vaneless space, runner and diffuser, where pressure sensors are placed. The measurements were performed for constant openness of the guide vanes, when changing the number of revolutions in the range  $\pm 30\%$  of the nominal one. Four operating modes were tested. The authors concluded that the amplitudes of pressure fluctuations in the vaneless space and in the runner increase with the number of revolutions.

### 3 Theoretical foundations

#### 3.1 Aerofoil and radial cascade of aerofoils – concept, basic geometric parameters

##### 3.1.1 Concept of aerofoil, basic geometric parameters

An aerofoil is a solid body that, when set in a fluid flow field or moving in a fluid medium, generates an aerodynamic force whose component in flow direction is very small compared to the flow component perpendicular to the flow. The aerofoils nomenclature is standardised according to NACA (National Advisory Committee for Aeronautics), which in 1930 conducted a series of experiments on derived aerofoils [37][38].

The ordinates of the aerofoil are measured relative to the x-axis corresponding to the aerofoil chord line  $c$ , which is a straight line joining the leading and trailing edges of the aerofoil. The middle camber line  $y_c(x)$  is obtained by connecting the centres of the inscribed circles in the aerofoil, i.e. it is located at half distance between the upper and lower surface, measured normal/perpendicular to the middle camber line itself (Figure 3-1).

Aerofoil thickness is the distance between the upper ( $x_u, y_u$ ) and lower contour ( $x_l, y_l$ ), perpendicular to the chord line. The shape of the aerofoil is obtained by defining the middle camber line and symmetrically "distributing" the thickness  $y_t(x)$  around it. The aerofoil leading edge is usually round, with a radius  $r_0$  of 2% of the chord length; the trailing edge may be rounded/flat or, more often, sharp.

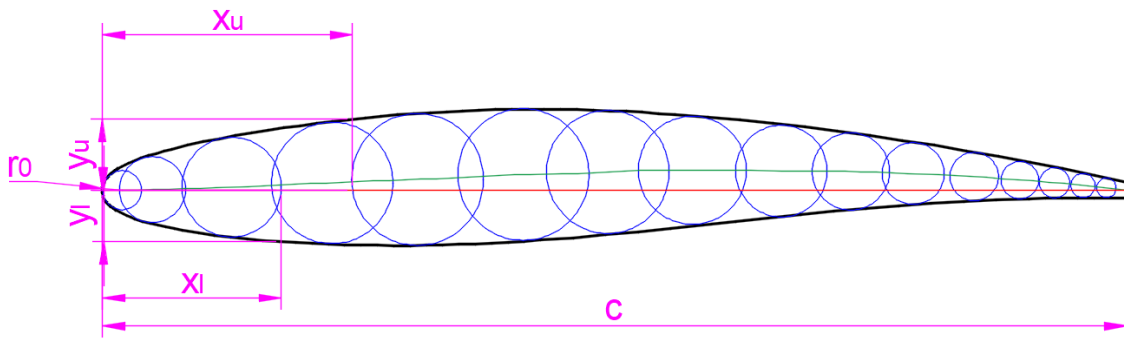


Figure 3-1. Defining an aerofoil - geometric parameters

The coordinates of the upper contour of the aerofoil are calculated according to:

$$x_u = x - y_t \sin \gamma; \quad y_u = y_c + y_t \cos \gamma \quad 3-1$$

$$x_l = x + y_t \sin \gamma; \quad y_l = y_c - y_t \cos \gamma \quad 3-2$$

where  $\gamma = \arctan\left(\frac{dy_c}{dx}\right)$ , and the functions  $y_c(x)$  and  $y_t(x)$  are known for a particular family of NACA aerofoils.

Relative parameters are often used to describe the aerofoil in relation to its length  $l$ : maximum relative thickness  $(\delta/l)_{max}$  and its location  $(x/l)_\delta$ , maximum relative curvature  $(s/l)_{max}$  and its location  $(x/l)_s$ . The largest curve can be expressed by the angle  $\theta$  between the tangent lines drawn from the starting and ending points of the camber line.

Aerofoils can be symmetrical or asymmetrical. In symmetrical aerofoils, the camber line coincides with the chord, while asymmetric profiles are obtained by applying the relative thickness of the symmetrical profile, perpendicular to the camber line (Figure 3-2).

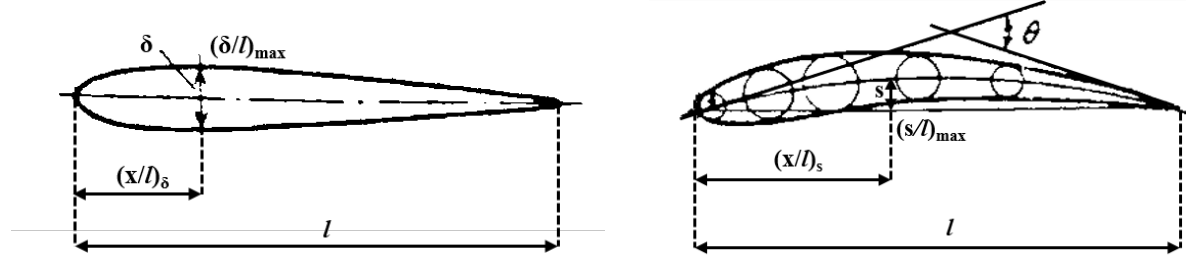


Figure 3-2. Symmetrical (left) and asymmetric aerofoils (right) and their description through relative parameters [37]

The aerodynamic characteristics of the aerofoil depend on its shape and the angle of attack  $\alpha_0$  defined as the angle between the aerofoil chord line and the flow velocity direction.

### 3.1.2 Cascades of aerofoils

The aerofoil characteristics will change by placing it in cascades of aerofoils. Aerofoil cascades are integral part of turbomachines and can be either axial or radial (Figure 3-3 and Figure 3-4). When the axis of the cascade connecting the same points of the aerofoils is a straight line, the cascade is axial, and when the cascade axis is circular, it is a radial cascade. A cascade can be stationary or rotating around axis, and, depending on whether it is a turbine or another type of turbomachine, it can be accelerating and decelerating cascade, respectively.

The length of the line (straight or circular) that coincides with the direction of the cascade axis between two adjacent aerofoils is called the cascade pitch  $t$ . The aerofoil position in the cascade is defined by the relative pitch  $t/l$  and the angle of inclination of the cascade  $\beta_R$  which is defined as the angle between the axis of the cascade and the perpendicular to the chord.

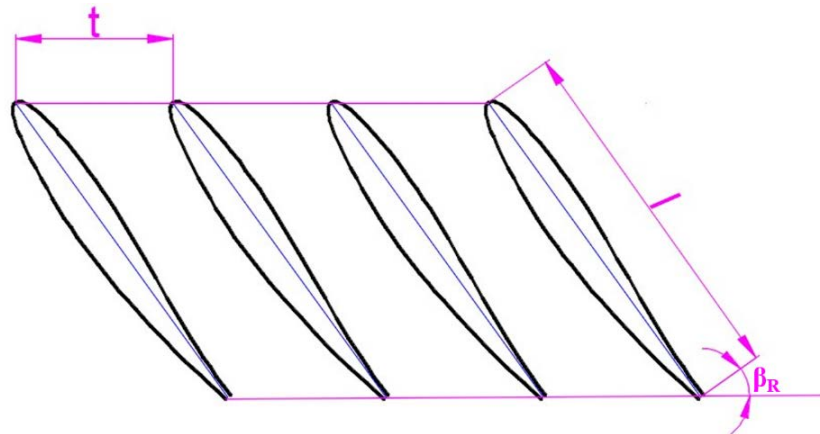


Figure 3-3. Axial cascade of aerofoils

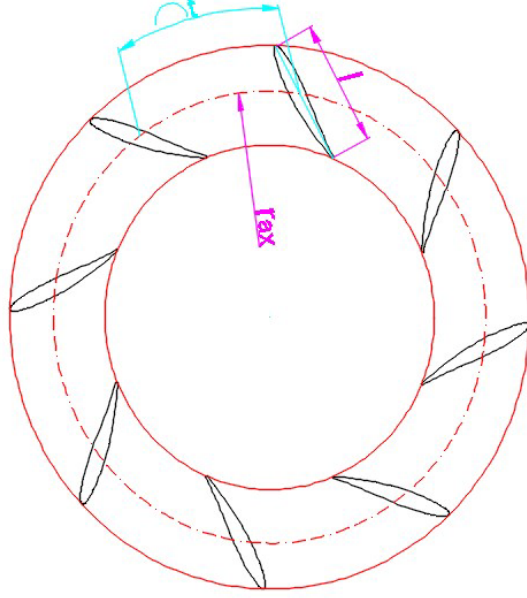


Figure 3-4. Circular cascade of aerofoils

## 3.2 Flow around solitary aerofoil and cascade of aerofoils. Forces acting on a solitary aerofoil and aerofoil in a cascade

### 3.2.1 Forces that acting on a solitary aerofoil and aerofoil in a cascade

When flowing around a solitary aerofoil or flowing through a cascade of aerofoils, an aerodynamic (resultant) force is generated which can be divided into two components: lift force  $F_L$ , perpendicular to the flow direction, and drag force  $F_D$ , parallel to the flow direction.

$$F_R = \sqrt{F_L^2 + F_D^2} \quad 3-3$$

Also, the resultant force can be represented as the sum of the normal force  $F_N$ , with direction normal to the chord, and the axial force  $F_A$ , parallel to the chord (Figure 3-5). The relation between these forces is through the aerofoil angle of attack  $\alpha$ .

$$F_L = F_N \cos \alpha - F_A \sin \alpha \quad 3-4$$

$$F_D = F_N \sin \alpha + F_A \cos \alpha \quad 3-5$$

By analysing the flow around a solitary aerofoil, it is concluded that the flow away from the aerofoil is parallel (undisturbed) and is defined by a velocity  $v_{E\infty}$  infinitely far in front of and behind the aerofoil, while disturbance of the fluid flow exists near the contour of the aerofoil. By introducing the dynamic pressure of the fluid flow at an infinite distance from the aerofoil  $q_\infty = \frac{1}{2} \rho_\infty v_{E\infty}^2$ , the forces (per unit width) acting on the aerofoil are defined:

$$F_{DE} = c_{DE} \frac{\rho}{2} v_\infty^2 l = c_{DE} q_\infty l \quad 3-6$$

$$F_{LE} = c_{LE} \frac{\rho}{2} v_{\infty}^2 l = c_{LE} q_{\infty} l \quad 3-7$$

where  $c_{DE}$  and  $c_{LE}$  are dimensionless coefficients of drag force and lift force, respectively, in a solitary aerofoil; they depend on the angle of attack and are determined experimentally.

According to the theory of circulation flow of a solitary aerofoil around which inviscid fluid flows, the lift force acting on a unit length of the aerofoil with infinite width defined by the velocity circulation is  $F_{LE} = \rho \Gamma_{1E} v_{E\infty}$ . This way of determining the lift force can also be applied to viscous flow around solitary aerofoil if the drag force  $F_{DE}$  is small (small angle  $\theta_E$ ).

The fluid flow through a cascade of aerofoils differs from the flow around a solitary aerofoil. Generally, the velocities of the fluid flow in front of and behind the cascade are different, as opposed to the velocities of the fluid infinitely far in front of and behind the solitary aerofoil which are the same. The term (fictitious) average velocity of the working fluid is used for a cascade of aerofoils which corresponds to the notion of the fluid velocity at an infinite distance from the solitary aerofoil:  $v_{\infty} = \frac{v_1 + v_3}{2}$ .

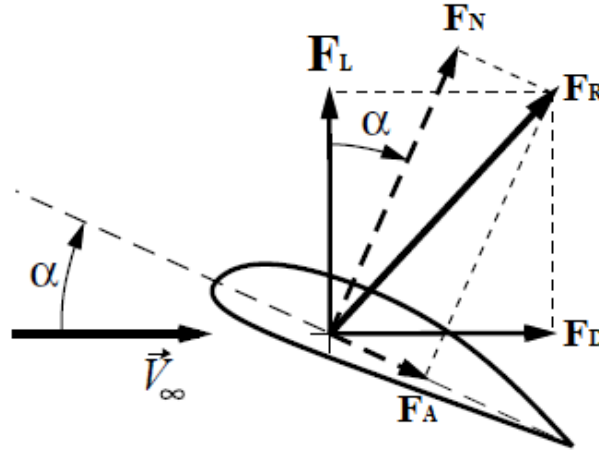


Figure 3-5. Forces that act on an aerofoil set in a flow field [39]

The lift force acts perpendicular to the direction of the vector of the fictitious mean velocity of the working fluid in the aerofoils cascade. The lift force is a result of the pressure difference between the upper and lower surface of the aerofoil, which means that the velocities along the contour of the aerofoil change, i.e. there is a velocity circulation around the aerofoil  $\Gamma_1$ . The elementary lift force acting on the aerofoil in a cascade is:  $dF_L = \rho \Gamma_{1E} v_{\infty} dr$ . (Figure 3-6).

On each of the aerofoils in the cascade acts a drag force  $dF_D$ , which has the same direction as  $v_{\infty}$ , and the same intensity and opposite direction of the force with which each aerofoil resists the displacement, caused by fluid particles which are drawn to the outer walls of the aerofoil as a result of the viscous forces.

The elemental lift and drag forces that act on the aerofoil in a cascade are:

$$dF_L = C_L \frac{\rho}{2} v_{\infty}^2 l = C_L q_{\infty} L dr \quad 3-8$$

$$dF_D = C_D \frac{\rho}{2} v_{\infty}^2 l = C_D q_{\infty} L dr \quad 3-9$$



flow field come from the distribution (change) of pressure and tangential stress across its surface. Thereby, the pressure acts perpendicular to the surface, while the tangential stress caused by friction between the aerofoil and the fluid acts tangentially (parallel) to the surface of the aerofoil.

Tangential stress can often be neglected, so the origin of the forces and moments arises from the distribution of pressure across the upper and lower surfaces of the aerofoil which is different for the same aerofoil placed in an unlimited fluid medium and in a cascade (Figure 3-7).

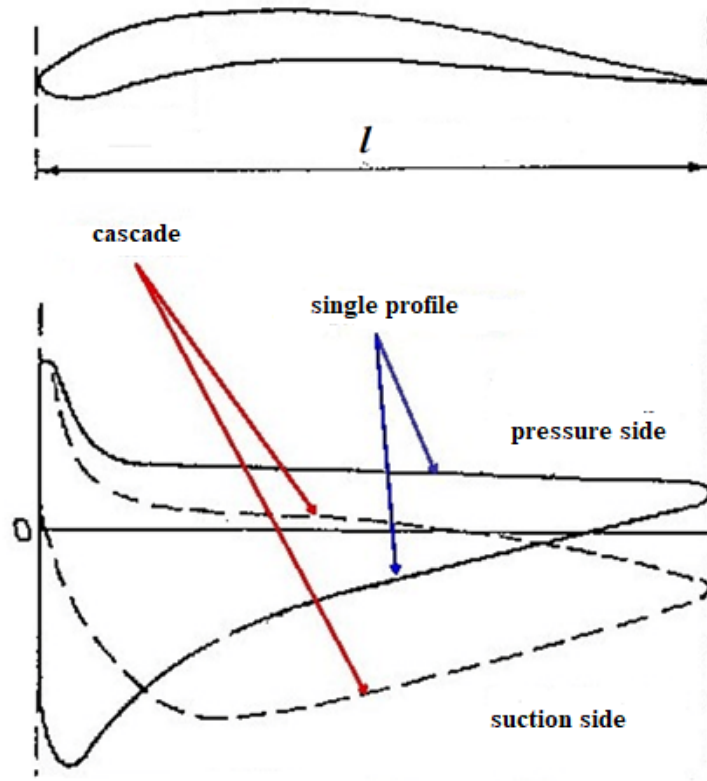


Figure 3-7. Example of a Kaplan turbine blade pressure distribution: in unlimited fluid medium and in a cascade [41]

### 3.2.2 Influence of aerofoil cascade parameters on pressure distribution (forces)

Influential parameters are the angle of attack, the inclination, and the cascade pitch. The aerodynamic properties of the aerofoil at a given angle of attack put in a cascade depend on the aerofoil shape - its properties as a solitary aerofoil - and from the cascade parameters (the relative cascade pitch and the angle of inclination).

In an axial cascade of symmetrical aerofoils with  $\alpha_0=0$  (shock-free inlet) and  $\beta_R=0$ , the flow is symmetrical because at the corresponding points on the upper and lower surface of the aerofoils there are the same pressures and velocities; the velocity in front of and behind the cascade is the same, i.e. there is no lift force. Only drag force occurs due to flow losses in the cascade - there is a pressure difference between the front and behind the cascade (Figure 3-7, left).

By changing  $\alpha_0$  (Figure 3-8, right) or  $\beta_R$  (Figure 3-9, left) the flow is no longer symmetrical, i.e. there is a pressure difference between the aerofoil surfaces, which causes the occurrence of a lift force. The velocity in front of the cascade is not in the direction of the axis because  $\alpha_0 \neq 0$ , as well as behind the cascade (there is a deflection of the fluid stream at the outlet  $\Delta\beta_2$ ).

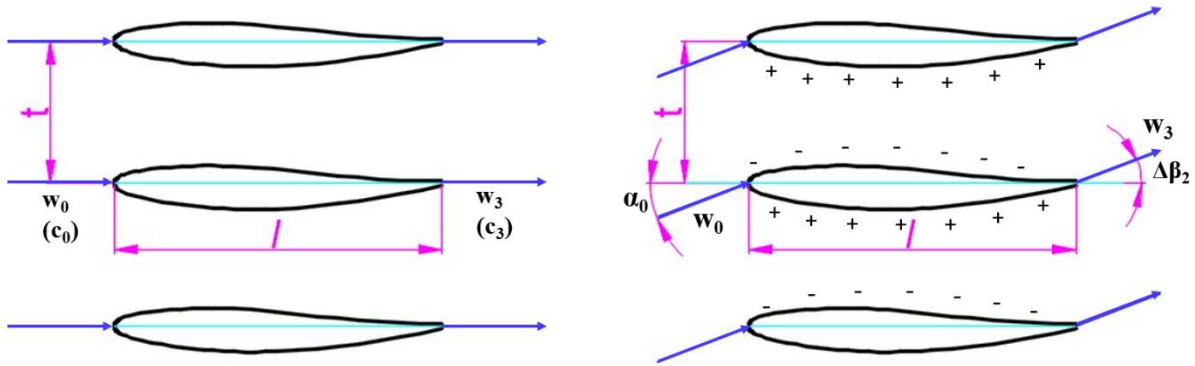


Figure 3-8. Cascade of symmetrical aerofoils without inclination with:  $\alpha_0 = 0$  (left) and  $\alpha_0 \neq 0$

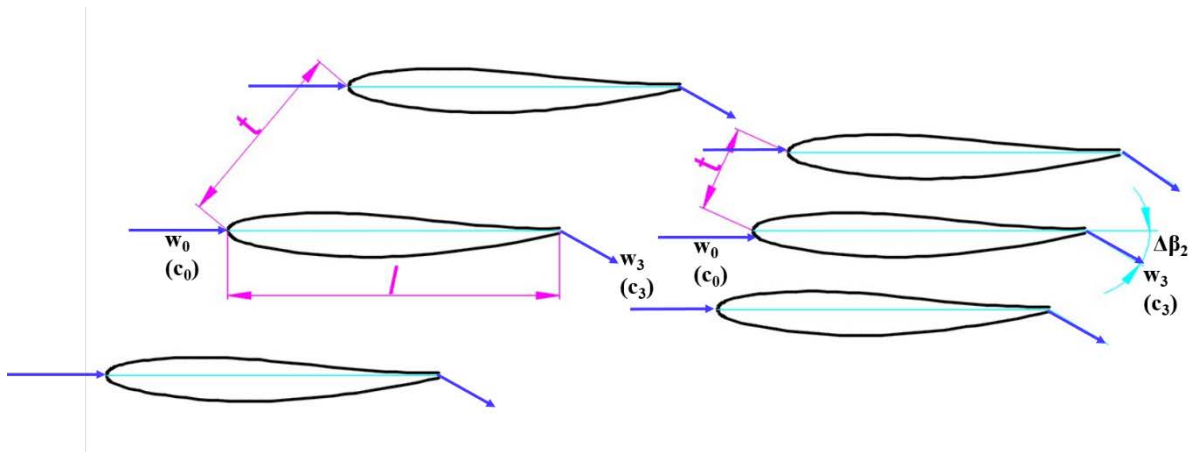


Figure 3-9. Cascade of symmetrical aerofoils with slope and different pitch

The lift force increases with decreasing inclination and the relative cascade pitch, which can be seen in Figure 3-10, where with increasing the relative pitch of the cascade the absolute values of the pressures on the aerofoil surfaces also increase [42].

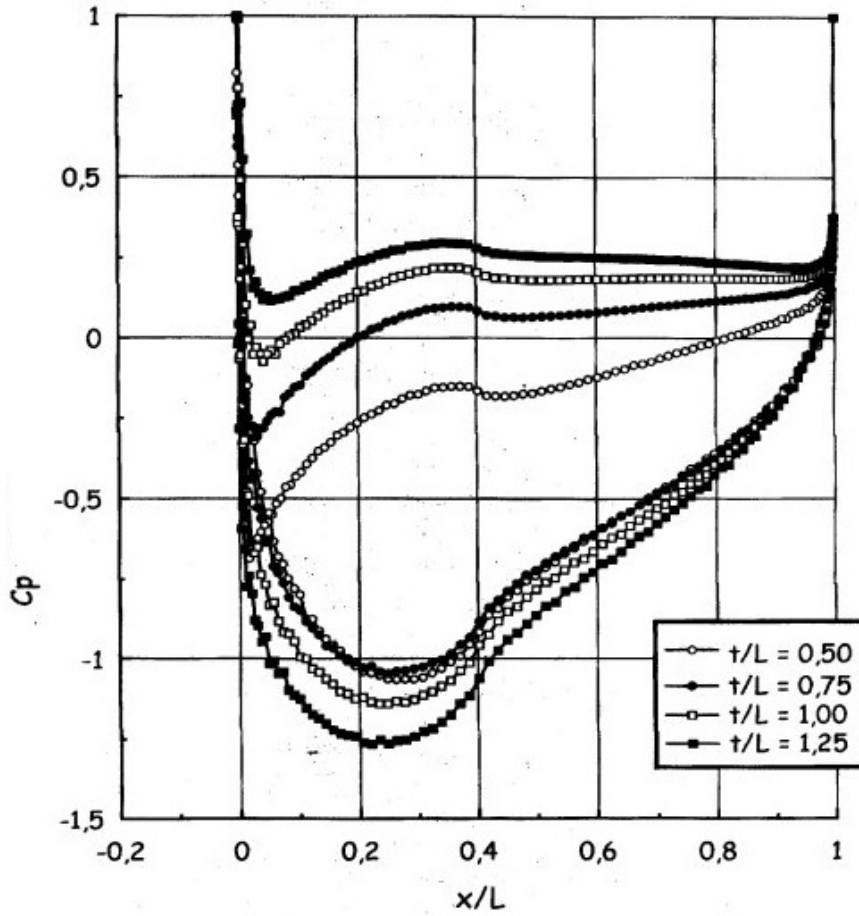


Figure 3-10. Relative pressure distribution of an asymmetric aerofoil in an axial cascade at different pitches [42]

### 3.2.3 Model for calculating forces and moments acting on an aerofoil

Normal and axial forces are obtained by integrating pressure and tangential stresses.

The elementary normal and axial forces on the upper surface are:

$$dF_{N'_u} = -p_u dl_u \cos\theta - \tau_u dl_u \sin\theta \quad 3-13$$

$$dF_{A'_u} = -p_u dl_u \sin\theta - \tau_u dl_u \cos\theta \quad 3-14$$

while on the lower surface of the aerofoil are:

$$dF_{N'_l} = p_l dl_l \cos\theta - \tau_l dl_l \sin\theta \quad 3-15$$

$$dF_{A'_l} = p_l dl_l \sin\theta + \tau_l dl_l \cos\theta \quad 3-16$$

The total normal and axial force per unit width of the aerofoil, respectively, are obtained by integrating the corresponding elemental forces along the contour (curvature) of the aerofoil from the leading to the trailing edge (Figure 3-11):

$$F_N' = - \int_{LE}^{TE} (p_u \cos\theta + \tau_u \sin\theta) dl_u + \int_{LE}^{TE} (p_l \cos\theta - \tau_l \sin\theta) dl_l \quad 3-17$$

$$F_A' = \int_{LE}^{TE} (-p_u \sin\theta + \tau_u \cos\theta) dl_u + \int_{LE}^{TE} (p_l \sin\theta + \tau_l \cos\theta) dl_l \quad 3-18$$

The moment of unit width around the aerofoil leading edge, on the upper and lower surface of the aerofoil, respectively, is:

$$dM'_u = (p_u \cos\theta + \tau_u \sin\theta) x dl_u + (-p_u \sin\theta + \tau_u \cos\theta) y dl_u \quad 3-19$$

$$dM'_l = (-p_l \cos\theta + \tau_l \sin\theta) x dl_l + (p_l \sin\theta + \tau_l \cos\theta) y dl_l \quad 3-20$$

The moment per unit width around the leading edge of the aerofoil is:

$$M'_{LE} = \int_{LE}^{TE} [(p_u \cos\theta + \tau_u \sin\theta)x - (p_u \sin\theta - \tau_u \cos\theta)y] dl_u + \int_{LE}^{TE} [(-p_l \cos\theta - \tau_l \sin\theta)x + (p_l \sin\theta + \tau_l \cos\theta)y] dl_l \quad 3-21$$

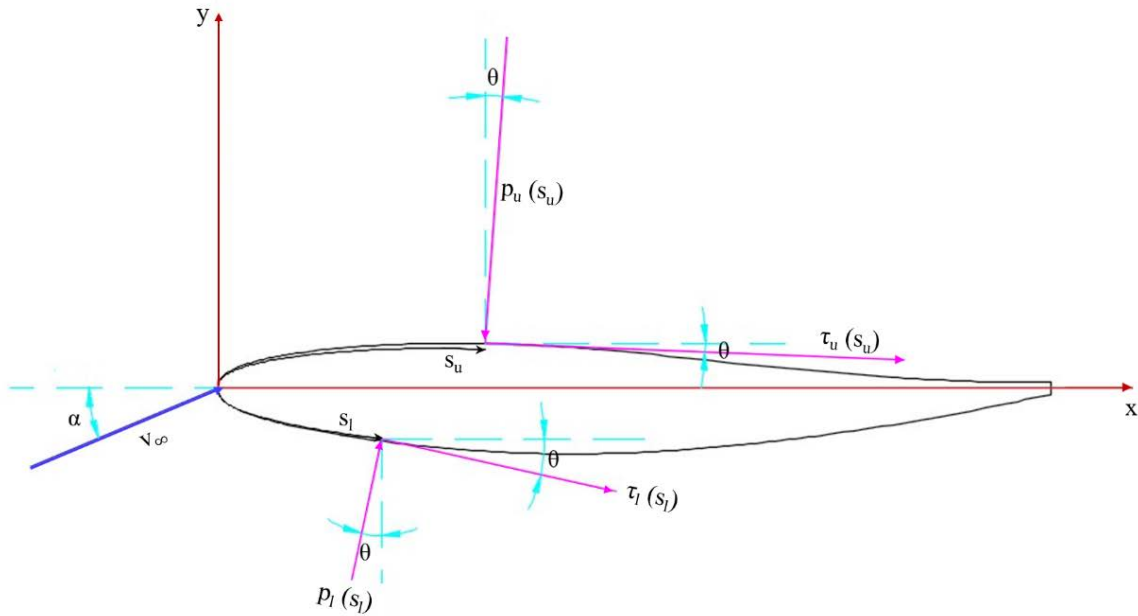


Figure 3-11. Variables in integrating pressure and tangential stress along the aerofoil contour

Thus,  $l_u$  is the distance from the leading edge of the aerofoil to the point on the upper surface in which the pressure  $p_u$  and the tangential stress  $\tau_u$  are calculated, while  $l_l$  is the distance from the leading edge of the aerofoil to the point on the lower surface in which the pressure  $p_l$  and the tangential stress  $\tau_l$  are calculated. For a point under consideration, the pressure is normal to the surface and acts at an angle  $\theta$  with respect to the vertical axis, while the tangential (shear) stress is parallel to the surface and acts at the same angle  $\theta$  with respect to the horizontal axis. Given that  $\theta$ ,  $x$ , and  $y$  are known functions of the aerofoil contour (curve) length  $l$  with a given shape, and  $p_u$ ,  $p_l$ ,  $\tau_u$ ,  $\tau_l$  are also functions of the aerofoil curve length  $l$  that can be

obtained experimentally, the integrals can be solved. For a given aerofoil shape that is set in a flow field, the problem of determining the forces and moments acting on it reduces to defining the functions  $p(s)$  and  $\tau(s)$ .

In the case of known pressure distribution along the contour of the aerofoil placed in the cascade, the forces acting on it are determined by applying the procedure described above. The described procedure is applied to the results of the experimental research.

### **3.3 Forces and moments acting on the blade of a guide vane system**

#### **3.3.1 Stationary radial cascade of hydrofoils – guide vane system**

The work exchanged in hydraulic turbines is the result of the interaction of the fluid flow with the rotating radial cascade of profiles called runner or impeller, while the direction of the working fluid in the runner/impeller is provided by the guide vanes system that is stationary cascade of a hydrofoils [40], [43].

The guide vane system of the Francis turbine is a stationary radial cascade of hydrofoils, evenly distributed around the main axis of the turbine, which directs the water in the runner and forms as even an as possible flow field with minimal energy losses [26].

The guide vane system achieves the necessary hydrodynamic conditions, i.e. it provides the necessary circulation at the runner inlet, taking into account the assumption that the circulation of a free stream does not change from the guide vane outlet to the runner inlet [44]. This is achieved by the guide vane outlet angle designed for the optimal turbine operating point. Turbine operation in other modes is made possible by changing the opening of the guide vane by simultaneously turning the blades at the same angle around its own axis of rotation by means of an external control mechanism. The opening of the guide vane  $a_0$  is the smallest distance from the trailing edge of a blade to the surface of the adjacent blade and defines the position of the guide vanes in the regulation of the turbine because its change regulates the water flow through the turbine according to the power [9] [22]. In all operating modes of the turbine, the guide vane system has to provide uninterrupted flow without creating vortex structures behind the blades [45].

The basic geometric parameters of the guide vane system (Figure 3-12) are: diameter of the circle which connects the axes of rotation of the blades  $D_0$ , number of blades  $z_0$ , blade height  $b_0$ , chord length  $L$ , maximum blade thickness  $\delta$ , distance between the points where two adjacent blades touch in the closed position  $L_0$ , relative eccentricity  $n_0$ , blade shape and cascade pitch  $t$ , all of which constant for a given guide vane system [46] [22].

A variable parameter is the openness of the guide vane system that is defined as the width of the inter-blade channel equal to the diameter of the largest inscribed circle in the inter-blade space. The guide vane system openness can also be defined by the blade angle of rotation relative to the reference position [44].

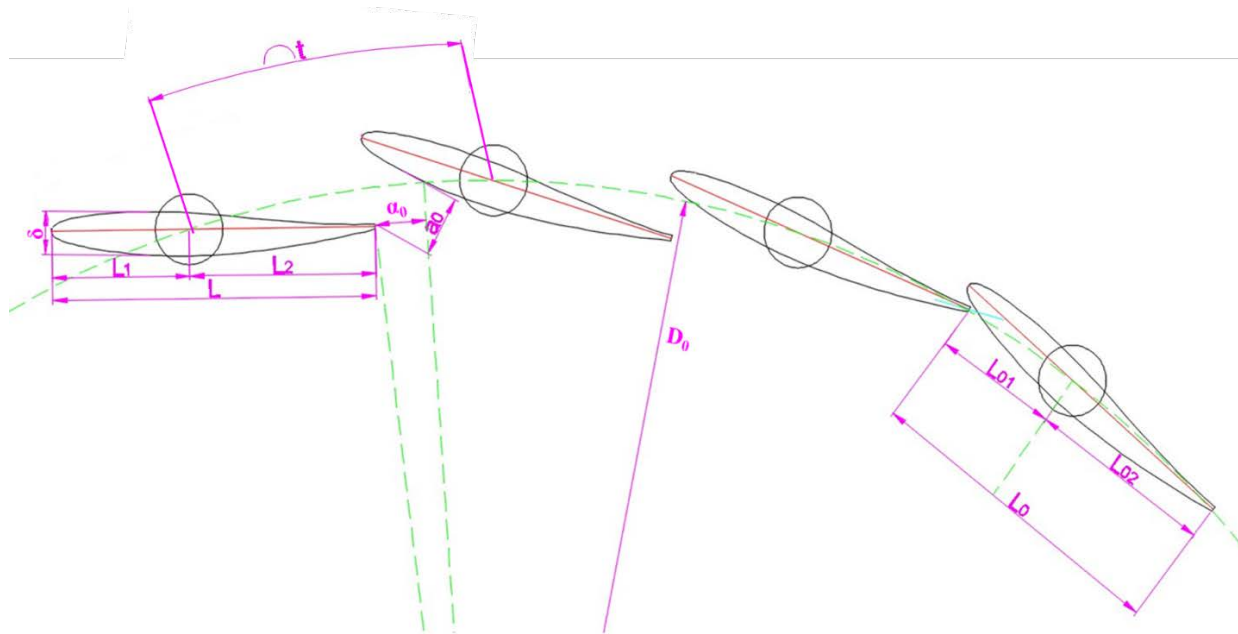


Figure 3-12. Basic geometric parameters of a guide vane radial cascade

Proper dimensioning of the guide vane system requires knowledge of the loads - the blade stresses that arise from the hydrodynamic forces and moments. The magnitude and direction of the hydraulic forces and moments on the guide vanes caused by the water flow depend on their shape, position (openness), and axis of rotation [47]. The greatest loads occur when the guide vane system is in the closed position, so the strength calculation should be performed for that case.

### 3.3.2 Forces and moments acting on the blade of a closed guide vane system

In a closed guide vane system, the pressure acts evenly on the effective surface of the blade  $B_0 \cdot L_0$  where  $B_0$  is the height of the blade and  $L_0$  is the distance between two adjacent blades, which is approximately equal to the cascade pitch  $t$ :

$$L_0 \cong t = \frac{D_0 \pi}{z_0} \quad 3-22$$

On the blade, the pressure from the water net head acts on one side and the pressure in front of the runner on the other side. Depending on the value of the pressure before the runner, the following cases are possible [48]:

- a) If the guide vanes are already closed ( $w_1 = w_2 = 0$ ), while the turbine is decelerating (but still operating) and the diffuser is filled with water that creates a vacuum pressure on the internal part of the blades equal to the difference between the water column  $H_d$  (Figure 3-13) and the overpressure in the runner  $h_p = \frac{u_1^2 - u_2^2}{2g}$ . The pressure difference:  $\rho g H_n - \rho g (-H_d + h_p) = \rho g (H_n + H_d - h_p) = \rho g \left( H_n + H_d - \frac{U_1^2 - U_2^2}{2g} \right)$  is the overpressure acting on the effective surface of the blade. Therefore, the resulting force acting on the blade is equal to:

$$P = \rho g \left( H_n + H_d - \frac{U_1^2 - U_2^2}{2g} \right) B_0 \cdot \frac{D_0 \pi}{z_0} \quad 3-23$$

- b) When the turbine is already stopped ( $u_1 = u_2 = 0$ ), but the diffuser is left filled with water, the overpressure from the runner does not exist ( $h_p = 0$ ), so the resultant force acting on the guide vanes is equal to:

$$P = \rho g (H_n + H_d) B_0 \cdot \frac{D_0 \pi}{z_0} \quad 3-24$$

- c) When after stopping the turbine air enters the diffuser, then the vacuum pressure from the diffuser  $H_d = 0$ , i.e. the resulting force on the guide vane is equal to:

$$P = \rho g H_n B_0 \frac{D_0 \pi}{z_0} \quad 3-25$$

The greatest force and moment will be obtained in the second case, so the strength calculation should be performed for such an extreme case [46].

By introducing the dimensionless quantities - relative blade height  $\overline{B_0} = \frac{B_0}{D_1}$  and relative diameter of the guide vanes system  $\overline{D_0} = \frac{D_0}{D_1}$ , the resulting force can be expressed according to [45]:

$$P = \frac{\pi \rho g H_{st} D_1^2 \overline{B_0} \overline{D_0}}{z_0} \quad 3-26$$

while according to [22],  $\overline{L_0} \overline{B_0} = A_0$ , a  $A_0 \rho g = A$ , so the resultant force is:

$$P = \rho g H_n B_0 L_0 = \overline{L_0} \overline{B_0} \rho g H D_1^2 = A_0 \rho g H D_1^2 = A H D_1^2 \quad 3-27$$

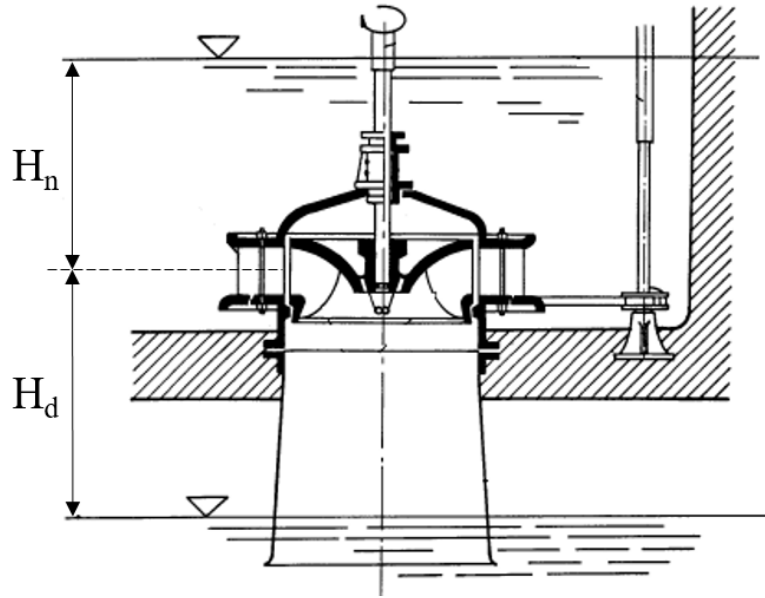


Figure 3-13. Pressure acting on a guide vane [49]

The resulting force is decomposed into two components, along the  $x$  and  $y$ -axis, respectively [22]:

$$P_x = \rho g H B_0 (y_2 - y_1) \quad 3-28$$

$$P_y = \rho g H B_0 (x_1 - x_2) \quad 3-29$$

where  $(x_1, y_1)$  and  $(x_2, y_2)$  are the coordinates of the contact points at the trailing and leading edges of the two adjacent blades, respectively.

The intensity of the resultant force is:

$$P = \sqrt{P_x^2 + P_y^2} \quad 3-30$$

and the angle it intersects with the horizontal is:

$$\alpha = \arctg \frac{P_y}{P_x} \quad 3-31$$

The coordinates of the attack point of the resultant force in a closed guide vane system according to a coordinate system with origin at the rotation point is:

$$x = \frac{x_1 + x_2}{2} \quad 3-32$$

$$y = \frac{y_1 + y_2}{2} \quad 3-33$$

i.e. the resulting force will act practically in the middle of the height  $B_0$ , near the middle of the length  $L_0$  between two blades, at a distance  $x_z$  from the point of rotation (Figure 3-13), which is called the absolute eccentre of the closed guide vane system  $s_0$ :

$$x_z = s_0 = \frac{L_{01} - L_{02}}{2} \quad 3-34$$

The resulting force tends to turn the blade with a moment [47], [48]:

$$M_z = P \cdot x_z = \rho g H B_0 L_0 s_0 \quad 3-35$$

or by applying dimensionless quantities, the moment is calculated according to [45]:

$$M_z = \rho g H B_0 L_0 n_0 L_0 = \rho g H B_0 \frac{\pi^2 D_0^2}{z_0^2} n_0 = \frac{\rho g H_{st} \pi^2 D_1^3 \overline{B_0} \overline{D_0^2}}{z_0^2} n_0 \quad 3-36$$

where  $n_0$  is the relative eccentre determined by:

$$n_0 = \frac{s_0}{L_0} = \frac{L_{01} - L_{02}}{2L_0} \quad 3-37$$

and its value is usually 0.05. According to [22], the distance between the point of attack of the force and the point of rotation of the blade can be represented by the reference diameter of the turbine, i.e.  $x_z = k_3 D_1$ , and by introducing the coefficient  $B_0 = A_0 k_3$ , and then the coefficient =  $B_0 \rho g$ , the moment can be expressed by:

$$M_z = Px_z = Pk_3D_1 = A_0\rho gHD_1^2k_3D_1 = B_0\rho gHD_1^3 = BHD_1^3 \quad 3-38$$

The moments of the forces along the x and y-axis are:

$$M_{P_x} = xP_y \quad 3-39$$

$$M_{P_y} = -yP_x \quad 3-40$$

i.e. the moment of the resultant force is determined by:

$$M_P = M_{P_x} + M_{P_y} = xP_y - yP_x \quad 3-41$$

It can be noticed that the dominant influence on the magnitude of the moment in a closed guide vane system has the position of the axis of rotation which affects the value of the relative eccentricity [47].

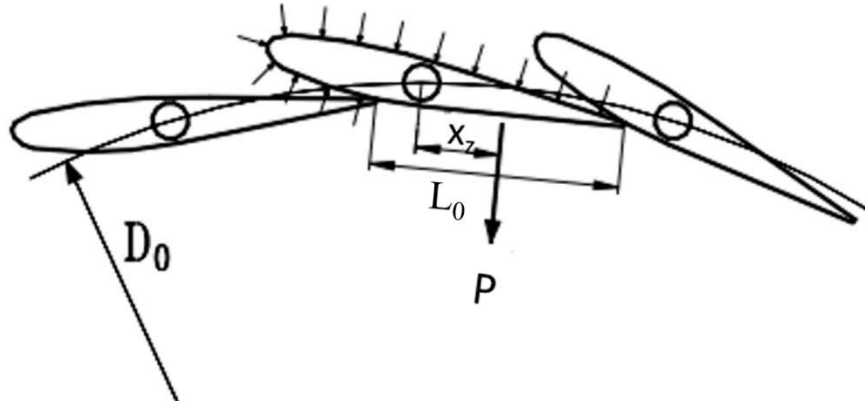


Figure 3-14. Forces acting on the blade of a closed guide vane system [47]

### 3.3.3 Forces and moments acting on the blade of open guide vanes

In the open position of the guide vanes system, water flows between the guide vanes and the water pressure varies along the curved surface of the blade. The pressure distribution over the blade surfaces will depend on the local water velocity, so a force P will act on the guide vane:

$$P = \gamma \int_0^{B_0} \int_0^L \frac{c^2}{2g} dz ds \quad 3-42$$

where  $L$  - blade length,  $dz$  and  $ds$  are sections of the blade length, in the direction of the axis and perpendicular to it, respectively,  $c$  is the local velocity of the fluid flow.

The pressure distribution (local velocity) changes depending on the opening of the guide vane, and thus the magnitude and direction of the resulting force. To get a complete picture of the guide vane loads, the calculation of the forces and moments acting should be performed for different openings of the guide vane system [47], [48].

Taking at least three blades in the considered open position, the streamlines in the inter-blade channels and the trajectories perpendicular to them are drawn, for which flow surfaces can be calculated ( Figure 3-15). For a known flow corresponding to the openness, from the

continuity equation, the (local) velocity through the flow cross-section with an area determined by the normal distance between adjacent blades  $a'$  follows:

$$c = \frac{Q}{a'B_0} \quad 3-43$$

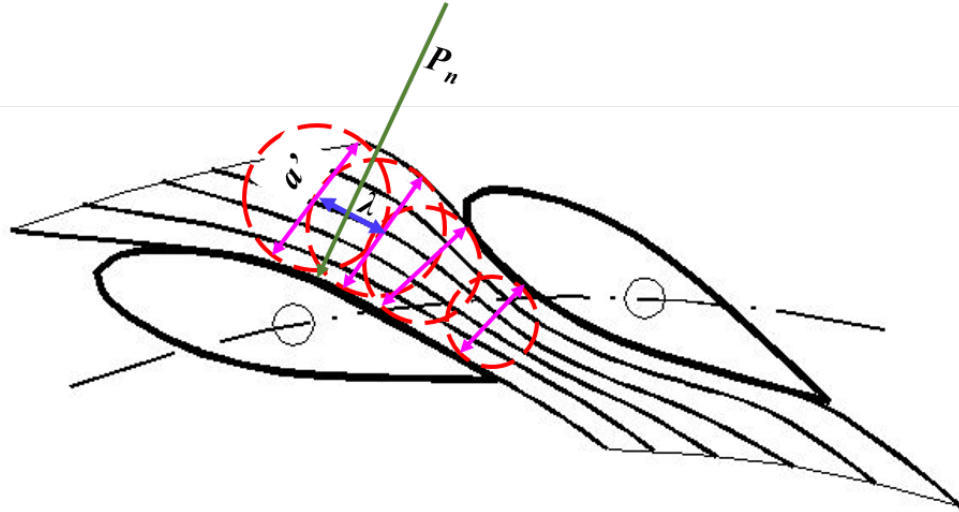


Figure 3-15. Forces acting on the blade in an open guide vane system [48]

Knowing the velocity  $c$  in points of the inter-blade flow domain, by applying the Bernoulli equation, the corresponding pressure in those points can be determined, which will obtain the pressure profile (distribution) on the blade surface (Figure 3-16). For velocity  $c$  in the selected cross-section of the inter-blade channel, the pressure (in meters of water column) is:

$$h = H_n - \frac{1}{2g} (c^2 + \sum (\xi c^2)) \quad 3-44$$

If we neglect the hydraulic losses, i.e.  $\sum (\xi c^2) = 0$ , then the pressure is:

$$h = H_n - \frac{c^2}{2g} \quad \text{i.e.} \quad p = \rho g (H_n - \frac{c^2}{2g}). \quad 3-45$$

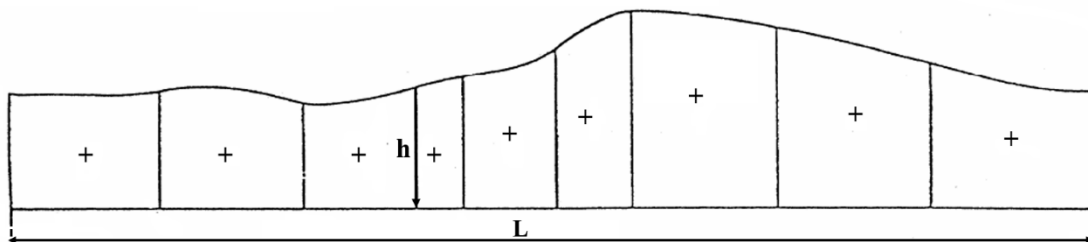


Figure 3-16. Pressure distribution over the blade surface [47]

The blade surface is divided into a number of elementary surfaces, of which in the centre of gravity an elemental force  $P_n$  acts whose magnitude is:

$$P_n = \rho g B_0 \int_{L_{n-1}}^{L_n} h dl \quad 3-46$$

If each elementary surface has the same length  $\lambda$ , a pressure force acts on each:

$$P_n = p B_0 \lambda \quad 3-47$$

In this way, the elemental forces acting perpendicular on the surfaces of the blade with length  $\lambda$  are determined, and they can be graphically summed into a resulting force by creating a polygon of forces whose intensity, direction, and location can be determined (Figure 3-16). The resulting force will act at a normal distance from the axis of rotation of the blade  $x_z$ , and with a moment:

$$M = \gamma \int_0^{B_0} \int_0^L \frac{c^2}{2g} x_z dz ds \quad 3-48$$

i.e.

$$M = P \cdot x_z = \sum P_n x_n \quad 3-49$$

where  $x_n$  is the distance at which the elemental pressure force acts relative to the point of rotation of the blade.

In this way, moments are determined for several openings of the guide vane system to which a certain flow corresponds (Figure 3-17). The point of rotation of the blade can then be determined so that the moments in the closed position and in the open position are approximately of the same order of magnitude.

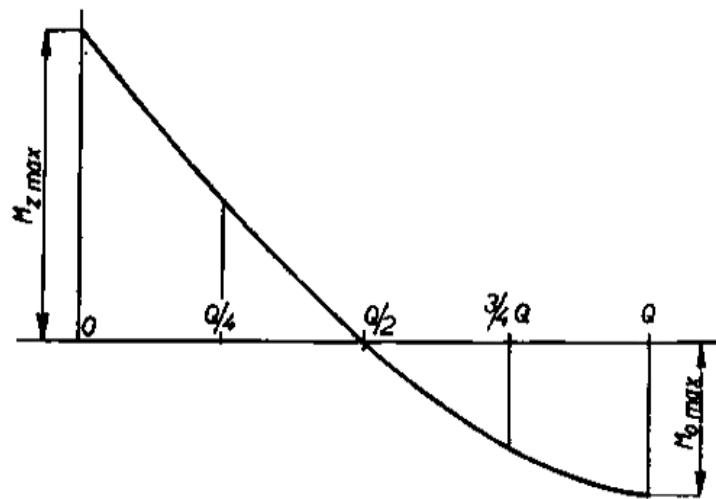


Figure 3-17. Changing the moment on the guide vane at different openings [48]

The total force as well as the moment must be proportional to the square of the velocity  $c^2$ , i.e. the square of the flow  $Q^2$ . The relative pressure distribution of the blade does not change with the change in flow. It is therefore convenient to introduce dimensionless coefficients of force and torque.

The force of the blade and the torque depend on the water flow or the velocity of the flow in the guide vane system, which, on their part, depend on the guide vane opening, the turbine operating mode, the position of the axis of rotation, as well as the shape of the blades. Therefore, when optimising the guide vane system, it is often necessary to change the position of the axis of rotation and the value of the eccentric within small limits.

In order to be able to properly dimension the guide vane mechanism, it needs to be known how the torque of the guide vane varies depending on the opening. As mentioned earlier, the resulting hydraulic force on the blades also changes the magnitude, direction, and point of attack with the opening. Hence, it is clear that by properly selecting the location of the blade shaft, the torque varies to some extent depending on the position of the blade. This variation can be determined according to the hydraulic calculations given above.

### **3.4 Guide vane stress distribution**

Stress analyses are important in the design of hydraulic turbines, especially because of the tendency to make as thinner as possible blades that have better hydraulic performance, reduce the mass of the structure, and thus the cost.

#### **3.4.1 Calculation of guide vane stresses**

The guide vane is designed to withstand both the bending stress resulting from the forces acting perpendicular to the blade axis and the torsional stress due to the moments acting on the lever.

Initial blade performance studies suggest that the guide vane is a beam supported by three bearings, subjected to a load  $q$  of water pressure distributed over most of the beam and a concentrated load  $P$  on the lever to calculate the bending stresses [22], [50]. The change in the moment of inertia along the blade is taken into account, and the torsional stresses are neglected because they are small.

The stress calculation is performed with a closed guide vane system where the loads are greatest because the pressure is maximum (Figure 3-18). In that case, the load distributed over the surface of the blade is uniform. The maximum stresses in the guide vane system are limited and must not exceed the allowable stress under maximum normal operating conditions (even distribution of the maximum load on all blades) [51].

Mathematical modelling of a blade as a beam does not take into account their complex shape, i.e. aerodynamic profile. More precise modelling of the blade is possible by applying the finite element method (FEM) and by modal analysis. A detailed picture of the stress changes in the blades can then be obtained and local changes in specific parts of the blade considered. Modal analysis can be used to obtain the change of natural frequencies and to analyze the forced vibrations in case the frequency of the forced frequency is close to one of the natural frequencies of the blade - resonance.

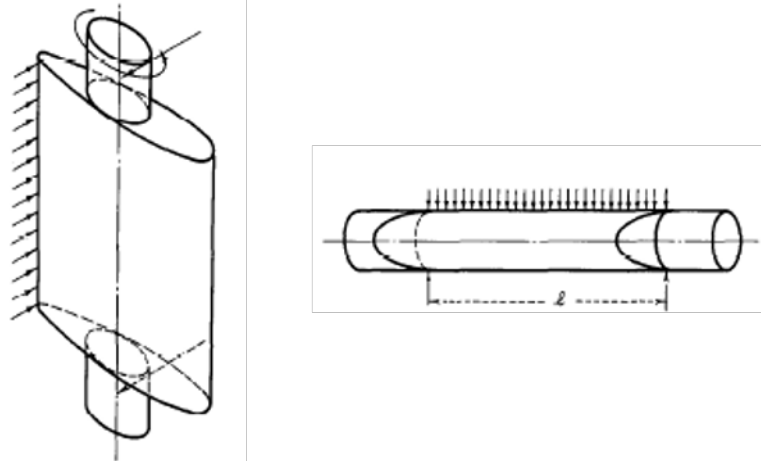


Figure 3-18. Strength calculation of a guide vane as a beam with even load [51]

### 3.4.2 Rotor-stator interaction

Changes can also be considered in the time domain, especially when flow disturbances are of interest, i.e. non-stationary phenomena that may occur in guide vanes such as rotor-stator interaction (RSI), pressure gradient disturbances, and vortices behind the blade. The effects of rotor-stator interaction (RSI) arise from flow interaction between the non-uniform flow distribution at the outlet of the wicket gates and the rotating runner blades passing through this flow i.e. pressure pulsations are caused by relative movement between the rotor and the stator [29], [52]. By rotating the runner blades, the water entering the runner is constantly moving. Thereby, the fluid velocities on the pressure and suction sides of the blade are different, causing vortices at the trailing edge of the blade.

The pressure fluctuations are significantly large especially in high head Francis turbines as a result of the slightly high guide vane outlet velocity in relation to the small radial gap between the blade cascades [53].

Figure 3-19 shows the impact of the runner blades (a) and the guide vanes on the flow field in the vaneless space (b), as well as their simultaneous impact (c).

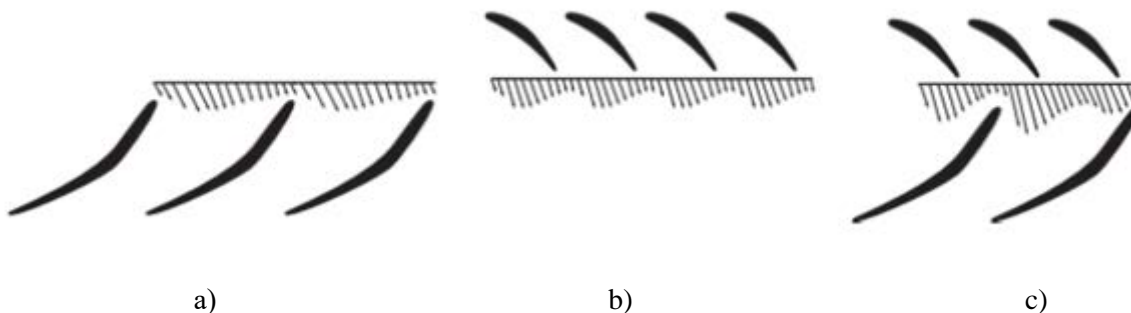


Figure 3-19. Impact of the runner blades and guide vanes on the vaneless space [29]

The unsteady flow field and the response of the structure to the forcing by the unsteady flow field are two aspects of RSI considered in Francis turbines [54].

On the runner, pressure fluctuations occur at the guide vanes passing frequency:

$$f_{gv} = z_0 f_n \quad 3-50$$

depending on the number of guide vanes  $z_0$  and runner rotational frequency  $f_n$ .

On the stationary components upstream of the runner the pressure fluctuations occur at the blade passing frequency:

$$f_{rb} = z_{rb} f_n \quad 3-51$$

where  $z_{rb}$  is the number of runner blades.

The pressure fluctuations in the vaneless space propagate in all directions upstream and downstream. The RSI between the guide vanes and runner blades in a Francis turbine is shown in Figure 3-20.

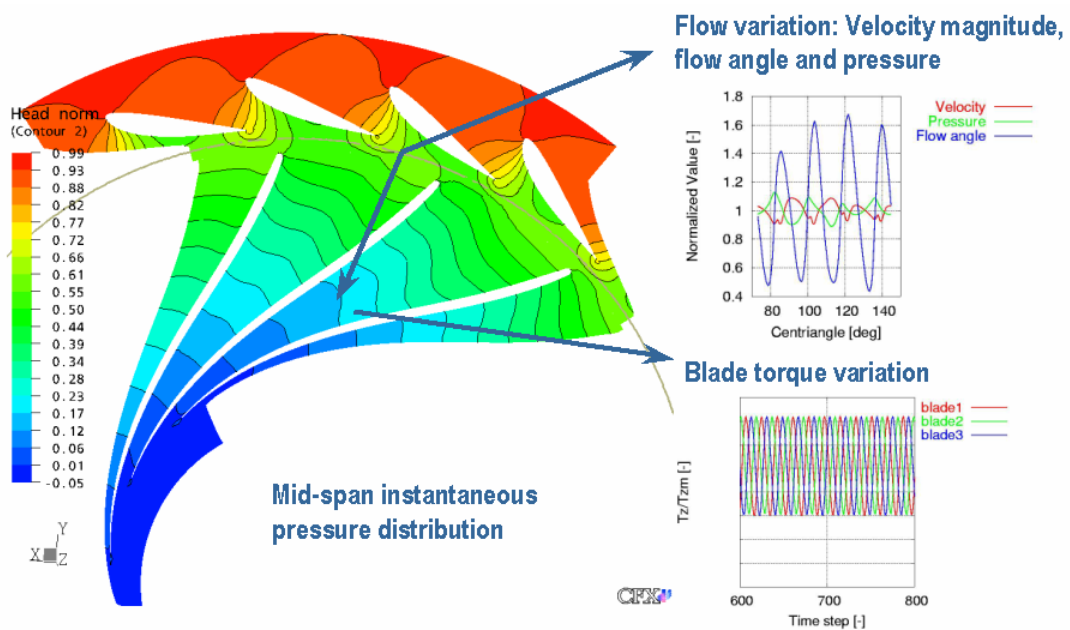


Figure 3-20. Rotor stator interaction between Francis turbine runner blades and guide vanes [55]

## 4 Experimental research

After setting the theoretical foundations, it is necessary to complete the key triangle of science: theory-numerical part-experiment. In-depth knowledge of the flow process in the cascade, the pressure distribution, and the forces acting on the aerofoil that are the subject of research in this dissertation can be obtained through experimental tests.

Conducting experimental research requires the preparation of an experimental system for measuring certain physical quantities of a constructed physical model using appropriate measuring equipment [56], [57]. Flow analysis in cascades continues with numerical modelling and simulations. The validation of the numerical model and the verification of the results of the numerical simulations were performed by comparison with the results of the experimental measurements.

### 4.1 Description of an experimental system for analysis of air flow around a profile placed in a circular cascade

The experimental research in this dissertation was conducted on a new purpose-designed experimental system installed in the Laboratory for Fluid Mechanics and Hydraulic Machines at the Faculty of Mechanical Engineering in Skopje. The designed experimental system consists of two main parts: a channel (Figure 4-1, left) and a measuring section with a circular grille of profiles (Figure 4-1, right).



*Figure 4-1. Components of the experimental system: channel and measuring section*

#### 4.1.1 Channel

As a part of the experimental installation, there is a horizontal pressure channel of closed type, made of Plexiglas, with steel construction. The cross-section of the channel is rectangular with dimensions - height  $h = 280\text{mm}$  and width  $w = 150\text{mm}$ , and length  $10 \cdot D_h = 2\text{m}$  (Figure 4-2). The airflow through the duct is provided by a centrifugal fan. At the junction between the pressure side of the fan and the inlet of the duct, a steel mesh with square openings (dimensions  $1\text{mm} \times 1\text{mm}$ ) is placed to calm the flow. Different modes of airflow through the duct are achieved by dimming the suction side of the fan. The channel is intended for measuring the airflow and achieving an even velocity profile at the measuring section entry.

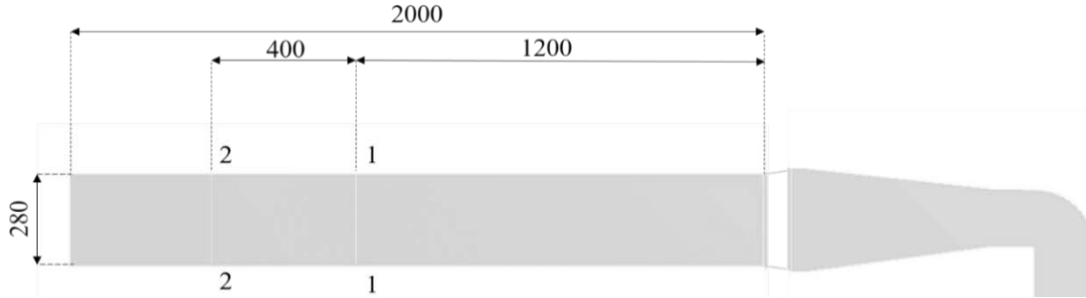


Figure 4-2. Geometric parameters of the channel

#### 4.1.2 Measuring section with a circular cascade of profiles

The measuring section at the outlet of the channel contains a segment of a circular cascade of five profiled aerodynamic blades whose axes are placed on a radius of the dividing diameter (Figure 4-3). The space for air inflow to the radial cascade segment is limited by adjustable boundary walls. The entry of airflow from the duct into the cascade is axial. The blade on which the pressure distribution measurements are performed on its lower and upper surface - measuring blade is the central blade (no. 3) in the cascade. The blades adjacent to the central (blades no. 2 and no. 4) are called control blades because they control the symmetry of the flow in the two inter blade channels formed by the central blade. The end blades (no. 1 and no. 5) are boundary blades that form the inlet part of the channel, and through their adjustment, a smooth entry of shock-free flow is provided, i.e. maximum pressure on the leading edge of the central blade (and control blades).

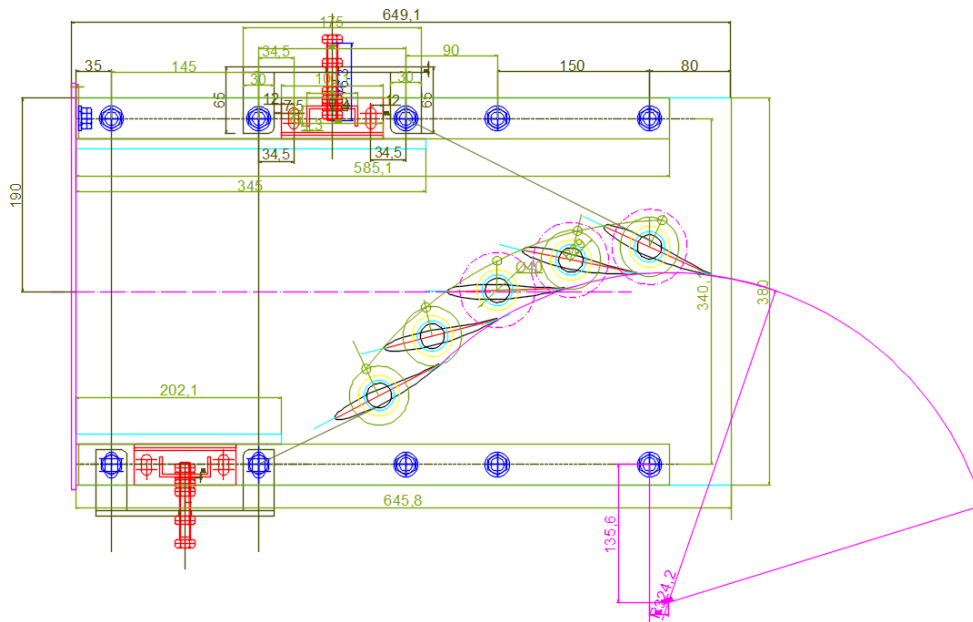


Figure 4-3. Measuring section with a segment of a circular grid of five profiles

The blade has a length of 115mm and a width of 130mm, inlet angle  $7.53^\circ$  and outlet angle  $1.66^\circ$ , shaft with a diameter of 30mm and centre at 40% of the length of the blade, with its

axis on the aerofoil camber line (Figure 4-4). The dimensions of the blade have been adopted to correspond to available space for the guide vanes of the Francis-99 turbine model in the Hydropower Laboratory of the Norwegian University of Science and Technology in Trondheim [58].

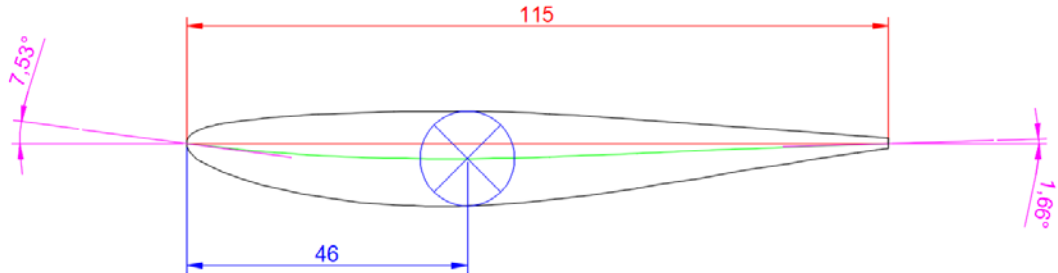


Figure 4-4. Basic parameters of the blade

The construction of the blade is made to be produced with 3D printing technology (Figure 4-5, left). The construction concept is set to obtain a homogeneous construction, with internally constructed channels that connect the openings on the lower/upper surface of the blade and through the sleeves to provide connections for pressure measuring instruments. The profile has 10 measuring points on the lower side and 10 measuring points on the upper side, i.e. 20 internal channels (with an opening of 2 mm) that lead from the measuring point to its outlet opening of the corresponding sleeve, Figure 4-5, right. Two front pressure gauges are placed on the leading edge of the blade. The measuring region of the blade covers 40 mm of the width of the blade, symmetrically to the blade axis.

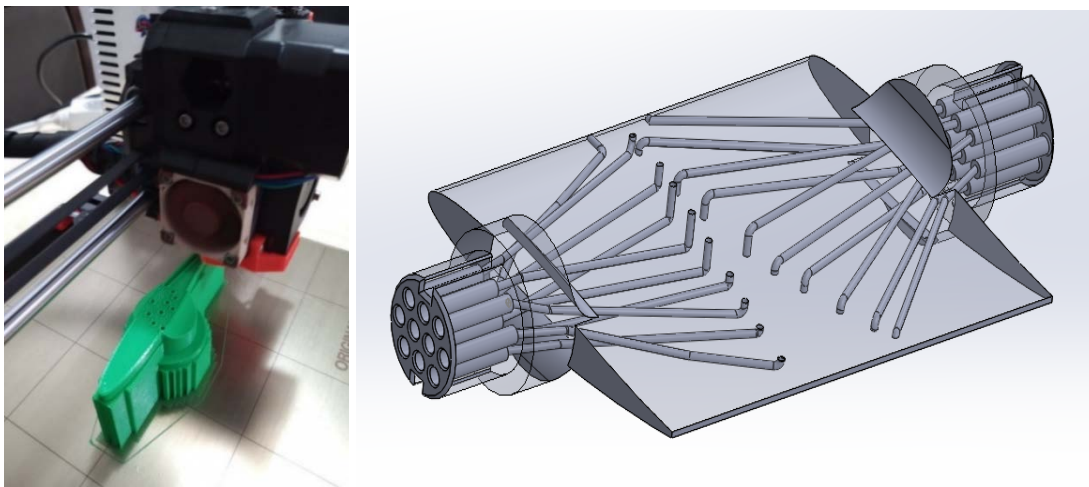


Figure 4-5. Process of making the blade with 3D printing (left) and its construction with arrangement of internal channels (right)

To check the uniformity of the real construction (parameters according to the technical drawing) and the manufactured physical model [59], control of the blade geometry (Figure 4-6) was performed on a calibrated numerical machine - comparator, with a spherical head of 6 mm,

according to which the deviations are  $-0.1959$  mm,  $+0.0073$  mm (Figure 4-7). As the differences are within tolerance, no correction or development of a new blade model was required.

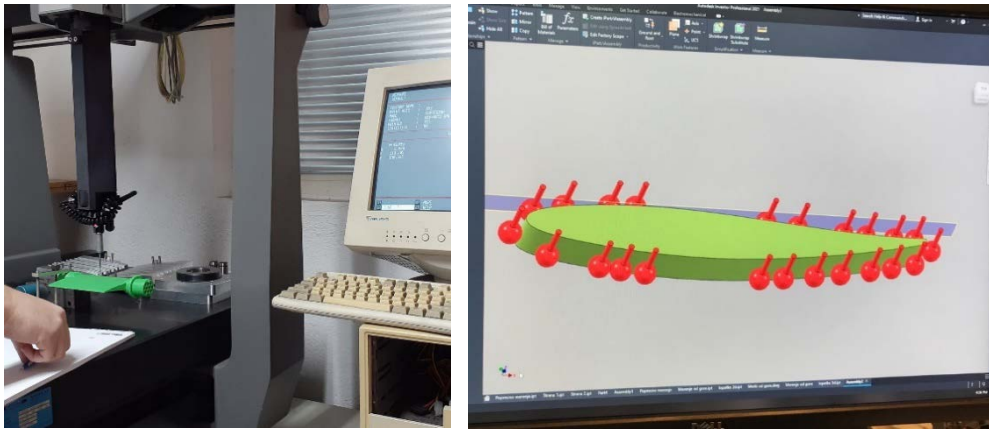


Figure 4-6.. Control of manufactured blade geometry using calibrator

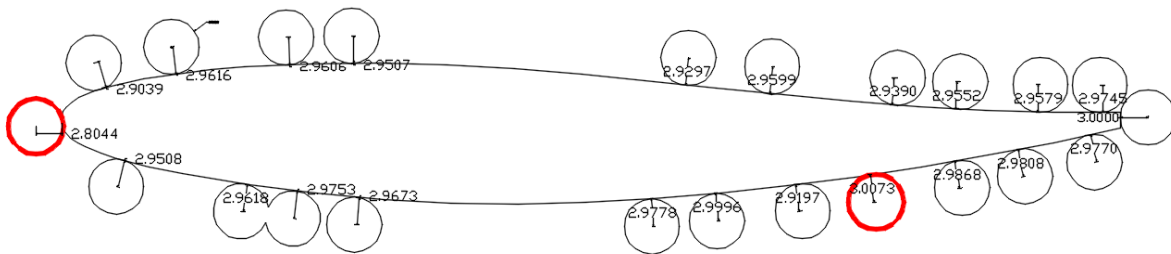


Figure 4-7. Results from the conducted blade geometry control

## 4.2 Measurement of flow technical parameters

In the experimental research, measuring instruments were used to measure the following flow parameters: pressure, flow, temperature, and the mechanical quantity: torque.

### 4.2.1 Measuring the pressure

The pressure is measured in the measuring sections of the channel and in the measuring points of the blade (central and control blades, separately). The pressure is measured with a set of 10 digital sensors with a range of  $\pm 1000$  Pa and with U-tubes with manometric liquid - water. For each given measuring point, the corresponding digital sensor and U-tube are connected in parallel. The digital sensors are connected to a pressure acquisition system with the ability to change the sampling time, monitor the pressure values at the measuring points in real time, and archive the data obtained from all sensors simultaneously in a tabular overview (Figure 4-8).

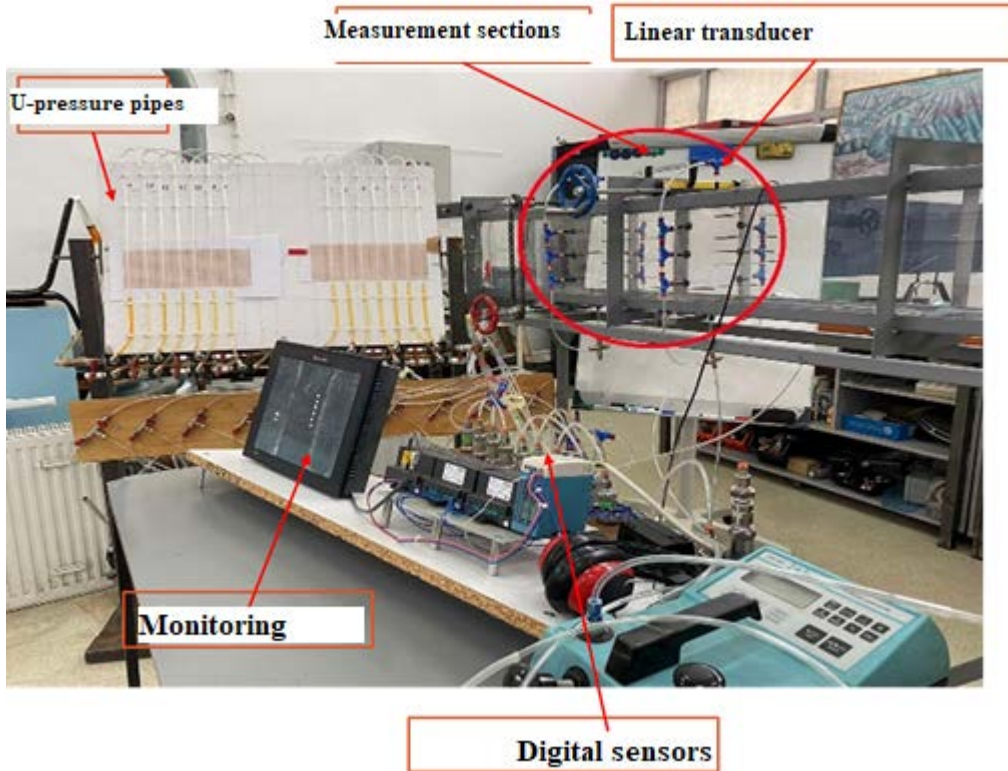


Figure 4-8. Pressure measuring system

For the installed pressure measuring system, test sets were performed in terms of showing the measured pressures and sampling time. Comparative measurements were performed by announcing the external gauge pressure and vacuum pressure of the simultaneously connected 12 sensors and the U-tube. It was concluded from the testing that there are no deviations in the intensity of the measured pressure values over time in the sensors with each other (Figure 4-9).

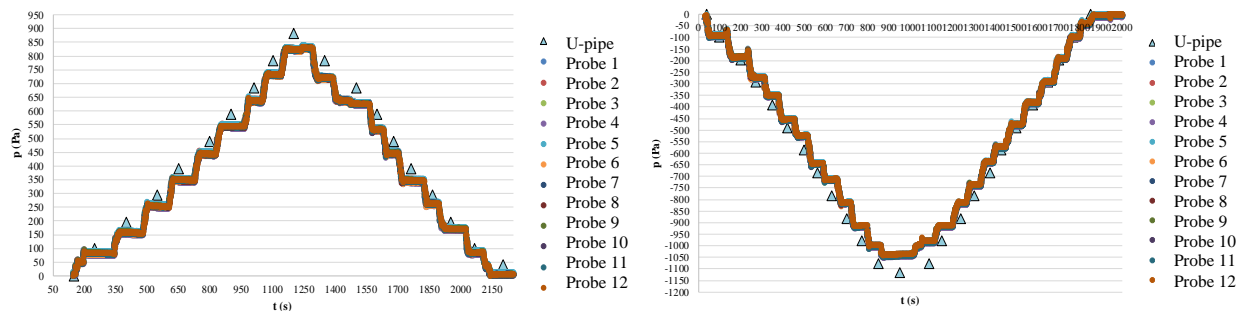


Figure 4-9. Comparative measurements for testing digital sensors

The test for the selection of sampling time is made on the basis of the measurements of total air pressure in the measuring section of the duct. Figure 4-10 shows the time-averaged values of the measured pressure at a sampling time of 0.01s, 0.05s, 0.1s, 0.2s, and 0.5s to see the effect of the presence of pulsations in the flow on the created values of the measured pressure. Based on the measured results and their analysis using a filter with fineness 10, it was determined that the sampling time of 0.01s, 0.05s, 0.1s, and 0.2s give a similar trend of change of

the mean pressure values in the same rank in relation to the mean value unlike 0.5s; the conclusion is that the sampling time of 0.2s is sufficiently precise. Based on the obtained test results for sampling time, further, in one operating mode, the pressure is measured with digital sensors for a period of 5 minutes where the data acquisition is performed with a sampling time of 0.2s.

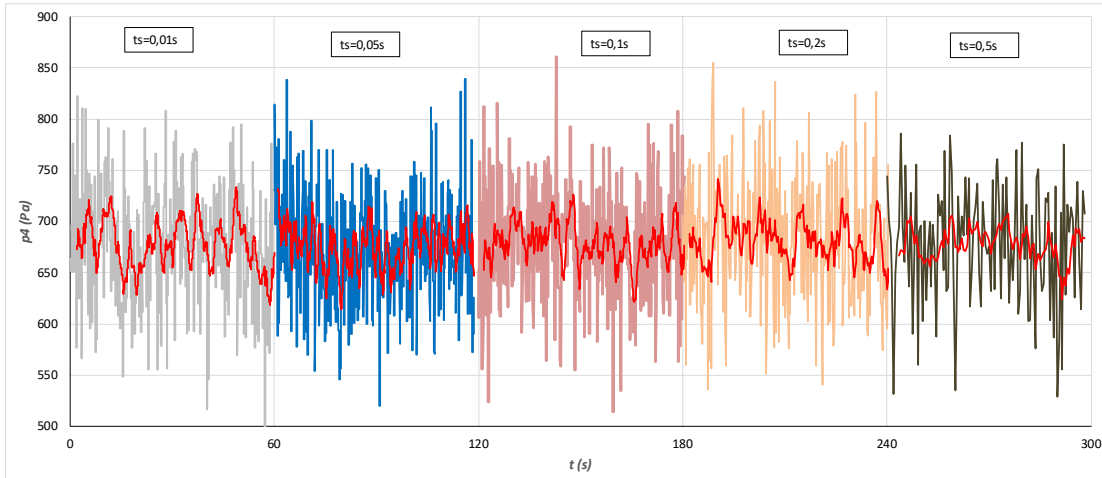


Figure 4-10. Time-averaged values of the measured total pressure by applying different sampling time

The error in measuring pressure with digital sensors is determined by the method of least squares error through the expressions [57] [60]:

- mean value:

$$\bar{x} = \frac{1}{n} \sum_{i=1}^n x_i \quad 4-1$$

- approximate error:

$$v_i = x_i - \bar{x} \quad 4-2$$

- absolute mean error:

$$\varepsilon = \sqrt{\frac{1}{n-1} \sum_{i=1}^n v_i^2} \quad 4-3$$

- relative mean error:

$$\varepsilon_p = \frac{\varepsilon}{\bar{x}} \cdot 100 \% \quad 4-4$$

where  $x_i$  represents measured pressure value, and  $n$  is the number of measurements.

## 4.2.2 Flow measurement

The methodology for determining the volume flow of air flowing in a duct under stationary conditions is based on calculation of local velocities by the measured differential pressures and the integration of the velocities.

### 4.2.2.1 Defining a velocity profile

To define the velocity profile, the local velocities (velocities at the measuring points) are calculated. To measure the velocity profile in the flow space of the channel, two measuring sections are placed perpendicular to the axis of the channel and at a distance of 1200 mm, i.e. 1600 mm from the beginning of the channel. In each measuring section, there is a vertical set of 7 (seven) Pitot tubes with predefined positions along the channel height for simultaneous monitoring of the speed profile. Pitot tubes are connected to digital sensors to measure pressure.

The arrays can be translated, and their location across the width of the channel is monitored and controlled by a linear transducer (Figure 4-11, left). Having 7 pitot tubes vertically positioned, at 7 points along the channel width, the air velocity is calculated at 49 measuring points (Figure 4-11, right) in order to more accurately determine the velocity profile.

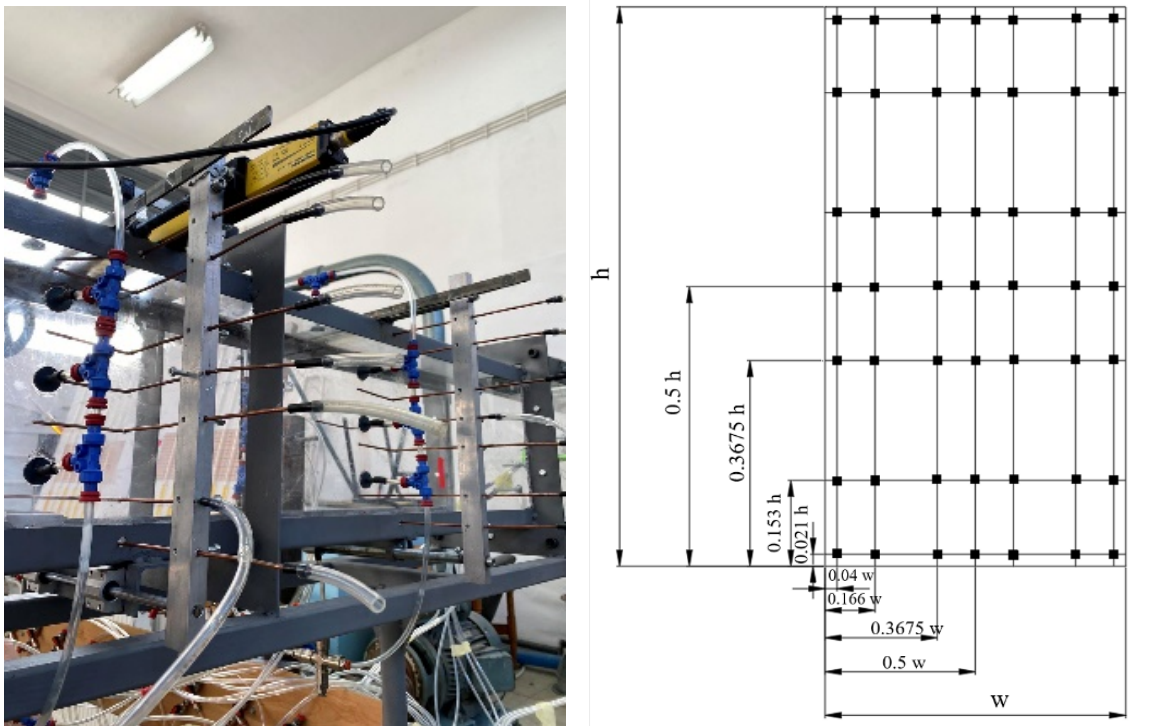


Figure 4-11. Measuring sections with pitot pipes and linear transducer (left) and measuring points in the channel section (right)

Static pressure is measured through the channel walls with a digital sensor.

Considering that the total pressure  $p_t$  is the sum of the static pressure  $p_{st}$  and the dynamic pressure  $p_d$  of the air:

$$p_t = p_{st} + p_t = p_{st} + \frac{\rho v^2}{2} \quad 4-5$$

the local velocity  $v$  of the air, averaged over a small area around the nose of the pitot tube, can be calculated as:

$$v = \sqrt{\frac{2(p_t - p_{st})}{\rho}} \quad 4-6$$

considering that the flow is compressible in the case of a small Mach number  $M < 0.2$ , when the air compressibility is not affected.

The density  $\rho$  of air is calculated according to the equation of state of an ideal gas:

$$\rho = \frac{p_{atm} + p_{st}}{RT} \quad 4-7$$

where the atmospheric pressure is  $p_{atm} = 101325 \text{ Pa}$ , and the gaseous constant of the air is  $R = 287 \text{ J/kgK}$ . The temperature is measured using a resistance thermometer.

Isolating the zone of the measurement point under consideration, the mean value of the indirectly measured local velocity is calculated according to the equation:

$$\bar{v} = \frac{v_1 + v_2 + \dots + v_n}{n} = \frac{\sum_{i=1}^n v_i}{n} \quad 4-8$$

#### 4.2.2.2 Procedure for defining the velocity profile

Three procedures have been applied to define the velocity profile in the channel cross-section. The first procedure (sequential method) involves measuring the local velocity at predefined positions (defined as a percentage of height and width) at the intersection, according to the standard [53]. The row of Pitot pipes is placed for a certain time in 7 points along the width of the channel in which the total pressure is measured. The mean values of the velocities at these points are calculated for different flow modes. Figure 4-12 on the left shows a horizontal velocity profile across the channel width, represented by local velocities in the measuring section of 1200 mm channel length. Taking into account that at the same time the vertical velocity profile is measured, a network of measuring points in the whole section can be determined, defined by the positions (coordinates) of the probes in the section.

The second procedure (continuous method) consists of continuous monitoring and acquisition of velocity profile data, where the stopping is in the previously defined measuring points along the channel width; but in this case, all measured pressure values are used during the measurement (not only at the stopping points but also at the transition between two consecutive measuring points) providing a more complete view of the profile. Figure 4-12 on the right shows a speed profile obtained by applying this kind of speed measurement, where at the same time the average values of the speeds at the fixed points are given (according to the first procedure).

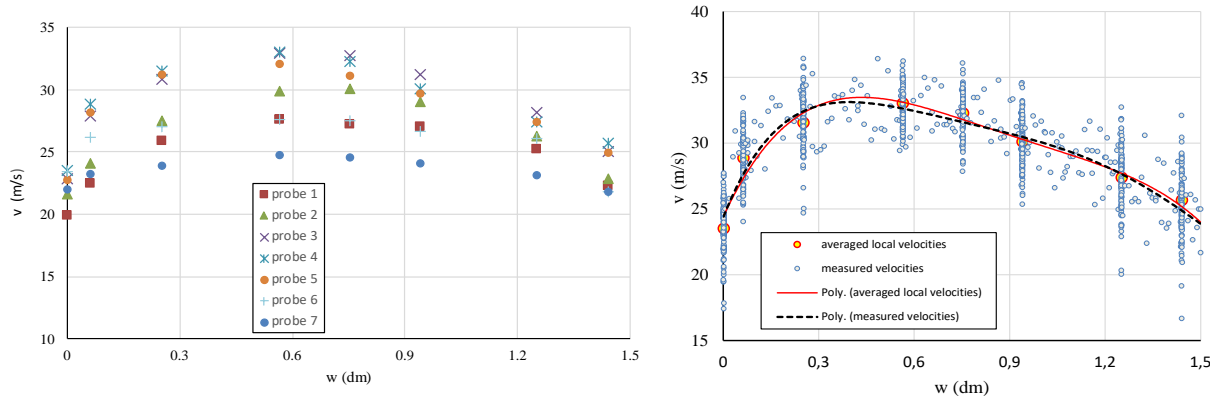


Figure 4-12. Horizontal velocity profile obtained through: mean velocities at fixed points across channel width (left) and semi-continuous velocity measurement (right)

The third procedure (continuous method) consists of continuous movement of the Pitot tubes without stopping along the cross-section of the channel, at different speeds of movement given in Table 1. The measurements were performed for both measuring sections.

Table 1. Different speeds of movement of Pitot pipes in the measuring sections of the channel

Speed:	$v_1$ [m/s]	$v_3$ [m/s]	$v_5$ [m/s]
Measuring section 1200 mm	0.03	0.041	0.0535
Measuring section 1600 mm	0.009	0.021	0.044

Figure 4-13 a) and b) show comparisons of the measured velocity profiles with continuous movement of the Pitot tubes (procedure 3) and the mean velocities at the stop points (procedure 1) for the central probe, for measuring cross-sections of 1200 mm and 1600 mm.

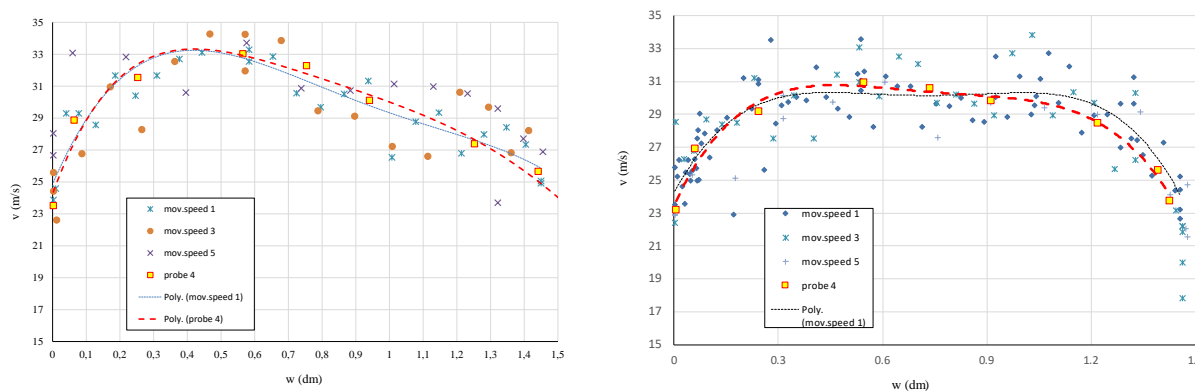


Figure 4-13. Horizontal speed profile obtained by continuous measurement for cross section of: a) 1200 mm; b) 1600 mm

At the same time, the speeds obtained with a lower speed of movement more accurately describe the shape of the velocity profile in the cross-section of the channel.

From the comparison of the results obtained with the three procedures, it can be concluded that there is alignment between the results for the velocity distribution.

### 4.2.2.3 Flow rate calculation

The obtained (measured) velocity profiles in the measuring section are used to determine the airflow in the closed duct in three different ways.

The first way to determine the airflow is by discretizing the cross-section of the duct in which average local velocities are calculated through the first procedure of defining the velocity profile. Discretizing the cross-section of the duct, the air flow is calculated as the sum of the elementary flows  $Q_{ij}$  which are products of the mean local velocity  $v_{ij}$  and the elementary area  $S_{ij}$  for the measurement point under consideration, i.e.:

$$Q = \sum Q_{ij} = \sum (v_{ij} S_{ij}) = \sum (v_{ij} \cdot \frac{w_i + w_{i+1}}{2} \cdot \frac{h_j + h_{j+1}}{2}) \quad 4-9$$

where  $i, j=1,2, \dots 7$  is an ordinal number of the measuring point along the width  $w$  and height  $h$  of the channel, respectively.

Calculation models are set in Excel, as well as in MATLAB, whereby a flow of  $1,157\text{m}^3/\text{s}$  and  $0.622\text{m}^3/\text{s}$  is obtained in two different operating modes.

The second method of calculation is based on the discretization of the channel cross-section and the application of interpolation polynomial equations that describe the profile of air velocities along the measuring line. By interpolating the values of the local velocities at the stopping points across the width of the channel (Figure 4-14), a 6<sup>th</sup> order polynomial function is obtained:

$$v = C_6 w^6 + C_5 w^5 + C_4 w^4 + C_3 w^3 + C_2 w^2 + C_1 w \quad 4-10$$

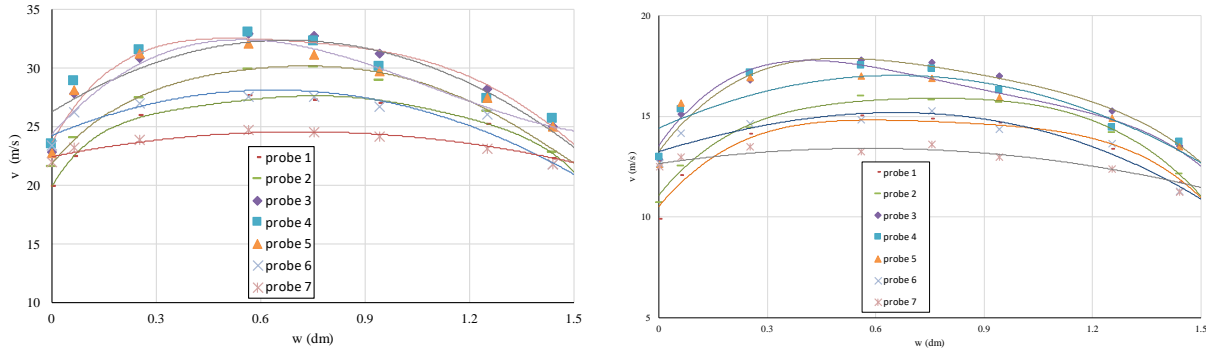


Figure 4-14. Polynomial function performed for the measured local velocities in the flow mode: a) 1 and b) 2

The obtained polynomial coefficients  $C_6, C_5, C_4, C_3, C_2, C_1$  and  $C_0$  are used to calculate the air velocity at numerous points along the channel width. With discretization as in the first case, the total air flow in the duct is calculated. Additionally, the polynomial equations are inserted in MATLAB where a 3D network of points is presented in which the velocity  $v$  is calculated depending on the coordinates of width  $w$  and height  $h$  in the intersection (Figure 4-15). By applying a function for numerical integration with a trapezoidal method, the volume flow is calculated. Because the velocity depends on the position of the measuring point in the measuring section, i.e.  $v = f(w, h)$ , the flow in MATLAB is calculated by the equation:

$$Q = \iint v(w, h) dw dh \quad 4-11$$

The third way to determine airflow involves use of graphic software to calculate the volume enclosed between interpolation curves. Using graphic software, from the network of polynomial curves that describe the velocity profile in width and height, a curved 3D surface is formed whose base overlaps a volume whose value is equal to the flow (Figure 4-15).

A comparison of the results for the volume airflow in the duct using the three calculation methods for two different flow modes is given in Table 2.

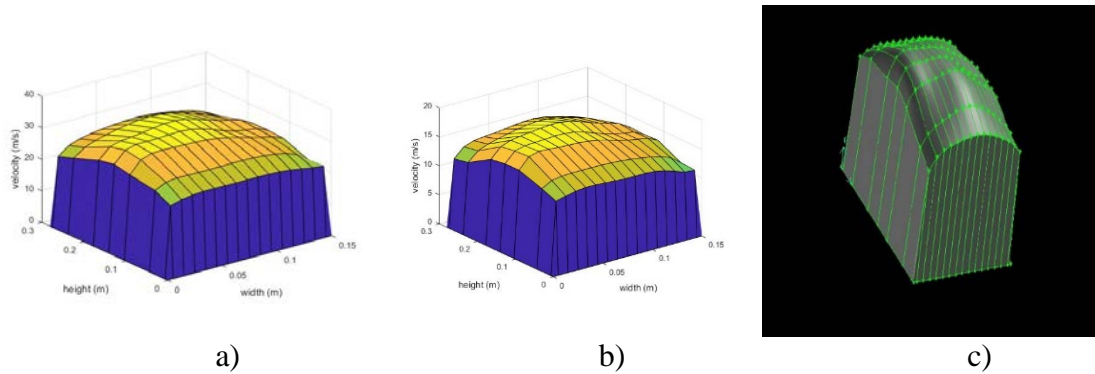


Figure 4-15. Graphical representation of the volume in MATLAB for a) mode no. 1 and b) no. 2 of 1200 mm and c) in GAMBIT software for mode no. 1

Table 2. Calculated volume flow values in three different ways

Mode no.	1 Q (m <sup>3</sup> /s)	2 Q (m <sup>3</sup> /s)	3 Q (m <sup>3</sup> /s)	Q <sub>sr</sub> (m <sup>3</sup> /s)	1 ΔQ (%)	2 ΔQ (%)	3 ΔQ (%)
1	1.157	1.1	1.12	1.125	2.8	-2.22	-0.44
2	0.622	0.603	0.612	0.6123	1.58	-1.52	-0.049

The differences in the flow values in relation to the obtained mean value do not indicate compliance in the three different calculation methods.

#### 4.2.2.4 Average velocity calculation

After calculating the airflow, the average velocity of the duct is calculated according to the obtained flow  $Q$  and the cross-sectional area of the duct  $A$ :

$$v_{ave} = \frac{Q}{A} = \frac{Q}{w \cdot h} \quad 4-12$$

The obtained average velocities in the channel cross-section for the two flow modes are given in Table 3.

Table 3. Calculated value of average velocity in the channel cross-section

Mode no.	$v_{ave}$ (m/s)
1	26,82
2	14,57

The required position (width and height) of the Pitot tube for measuring the average velocity in the channel can be obtained at the intersection of the velocity profile with the mean velocity value. This allows further application of only one probe in a fixed position instead of the entire string of Pitot tubes. By analysing the location of the average velocity in relation to the velocity profiles, set for different measuring lines and different flow modes, it is obtained that in the measuring section of 1200mm the probe no.2 can be used set at 20mm width of the channel (Figure 4-16, left). In the measuring section of 1600 mm, the central probe (no.4) is used, placed in the axis of the channel (75mm width) with the intention to be used as a control probe for the intensity of the flow.

#### 4.2.2.5 Uniformity of the flow field

The uniformity of the flow is presented for the velocity profile in the measuring cross-sections. Evenness is stated in the core of the flow, which is symmetrical horizontally and vertically (Figure 4-16 on the right), i.e. it is a zone where the measuring blade is placed and which covers the measuring zone of the blade. According to the obtained results, at the exit of the channel, i.e. at the entrance to the measuring section where the grid of profiles is placed, the uniformity of the velocity profile is achieved.

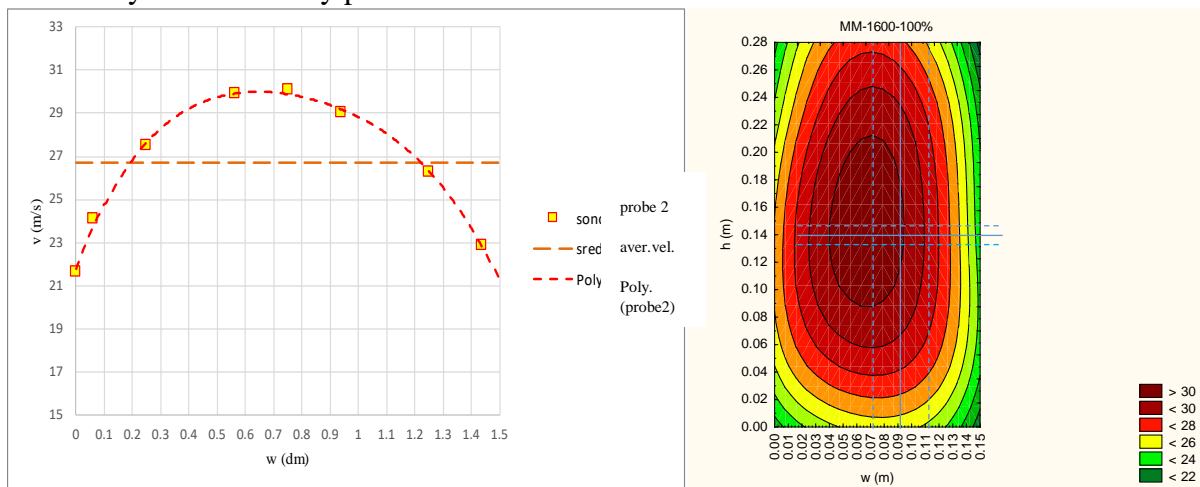


Figure 4-16. Velocity profile at measuring section at 1200mm (left) and 1600mm (right)

### 4.3 Results of profile pressure distribution measurements. Determination of forces, moments, and attack point of the resulting force

After achieving an even flow at the inlet in the measuring section where the profile/circular cascade of profiles is placed, a pressure measurement was performed on the surface of the profile. The results are processed in order to obtain the magnitude and direction of the aerodynamic forces and the coordinates of the attack point of the resultant force.

### 4.3.1 Solitary aerofoil

The distribution of pressure on the surface of the aerofoil, around which air flows, depends on the angle of attack of the aerofoil, i.e. its position in the flow/stream field. The pressure distribution is measured at different attack angles with respect to zero, i.e.  $\pm 5^\circ$ ,  $\pm 10^\circ$ ,  $\pm 20^\circ$  и  $\pm 30^\circ$  (Figure 4-17). The aerofoil in the tunnel is set with the pressure surface up and the suction surface down. For each attack angle of the aerofoil, pressure measurements were made at four different flow modes.

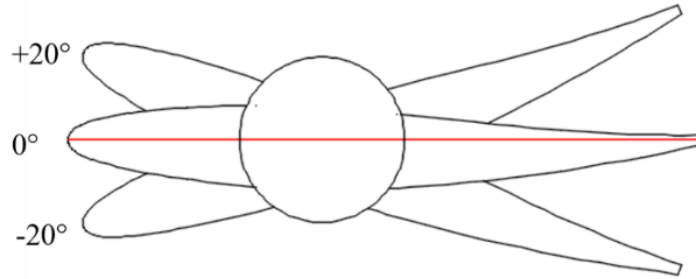


Figure 4-17. Aerofoil positions in which the pressure distribution is measured

In case the aerofoil is set to zero position (Figure 4-18), vacuum pressure occurs on the upper and lower side of the aerofoil. This position of the aerofoil corresponds to the uninterrupted (shock-free) inlet of air stream, with the greatest pressure on the leading edge of the aerofoil.

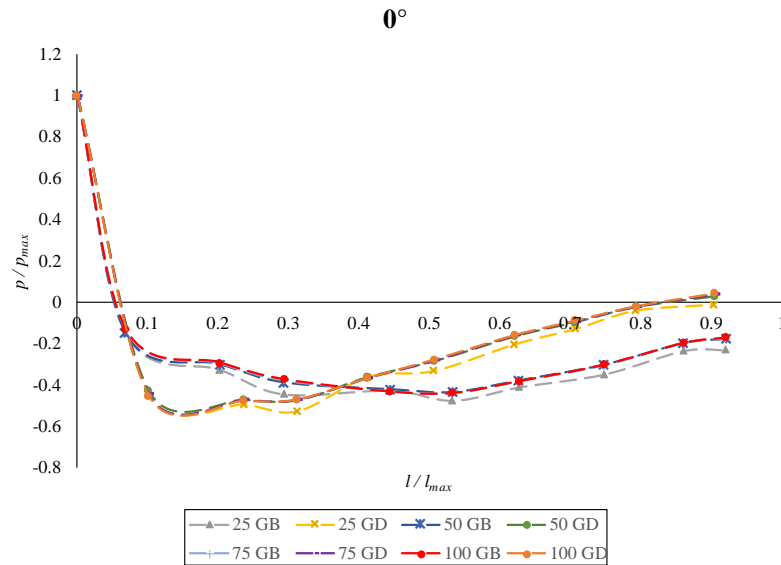


Figure 4-18. Aerofoil pressure distribution at zero-position

The measured pressures in the ten points distributed along the upper and lower surface of the aerofoil are given in relation to the maximum achieved pressure in the respective mode, i.e. as relative values so that the obtained forms of pressure distribution can be comparable. Thereby,

the position of the measuring points is given relatively in relation to the unit length of the aerofoil. The relative pressure distribution on the aerofoil, i.e. unit pressure profiles, reduced to unit total aerofoil length for different attack angles is presented in Figure 4-19, Figure 4-20, Figure 4-21 and Figure 4-22.

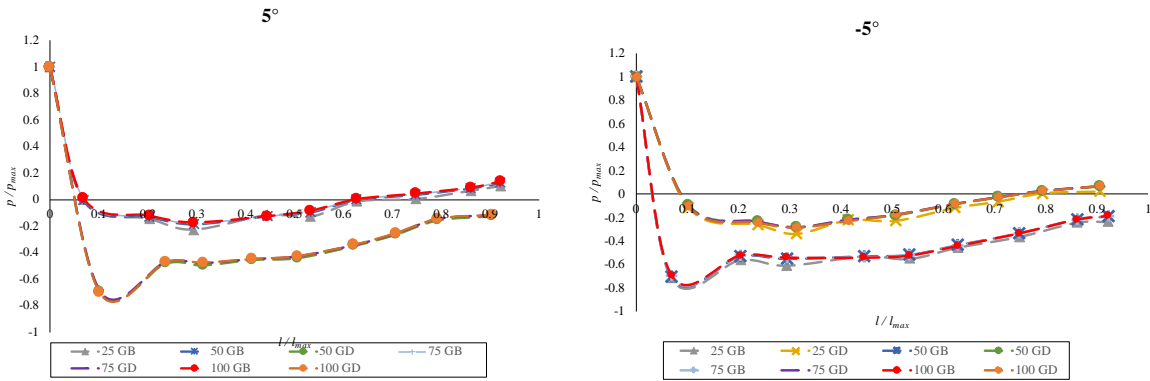


Figure 4-19. Unit pressure profile at attack angle + 5 ° (left) and -5 ° (right)

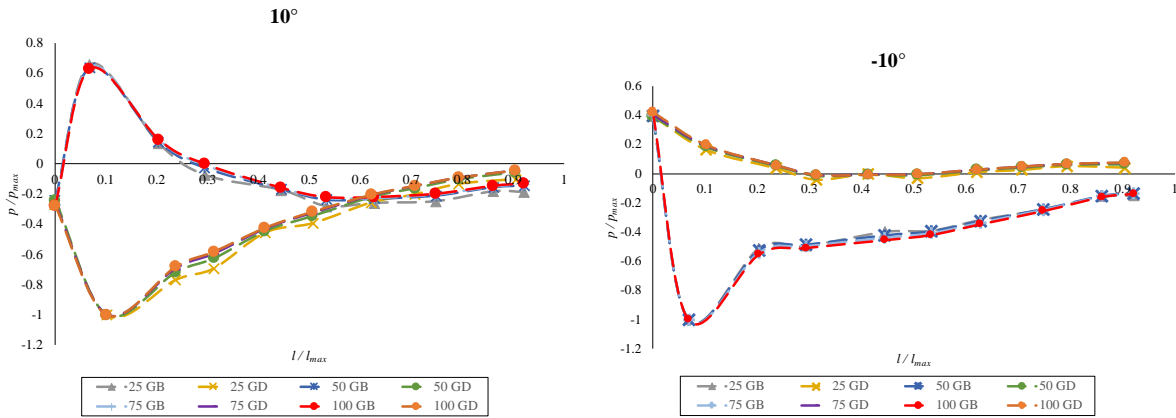


Figure 4-20. Unit pressure profile at attack angle + 10 ° (left) and -10 ° (right)

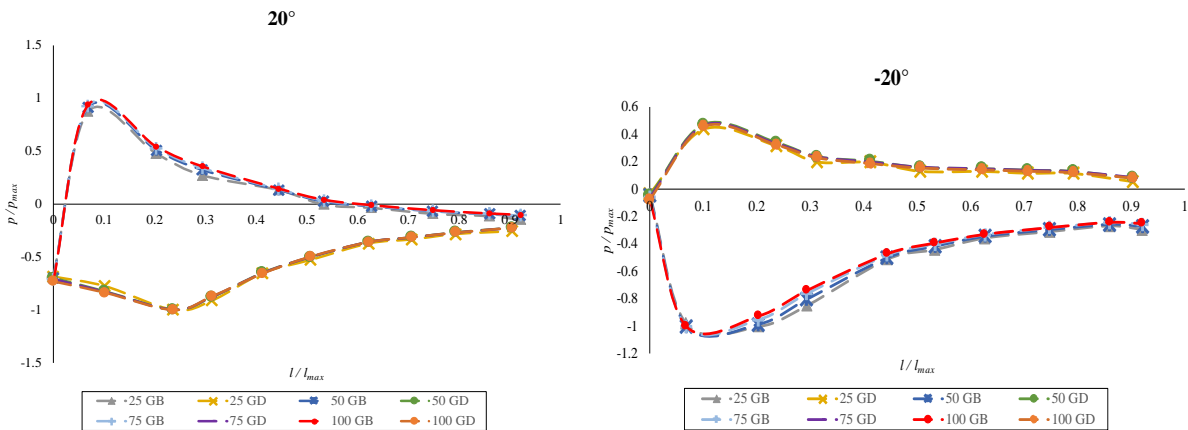


Figure 4-21. Unit pressure profile at attack angle + 20 ° (left) and -20 ° (right)

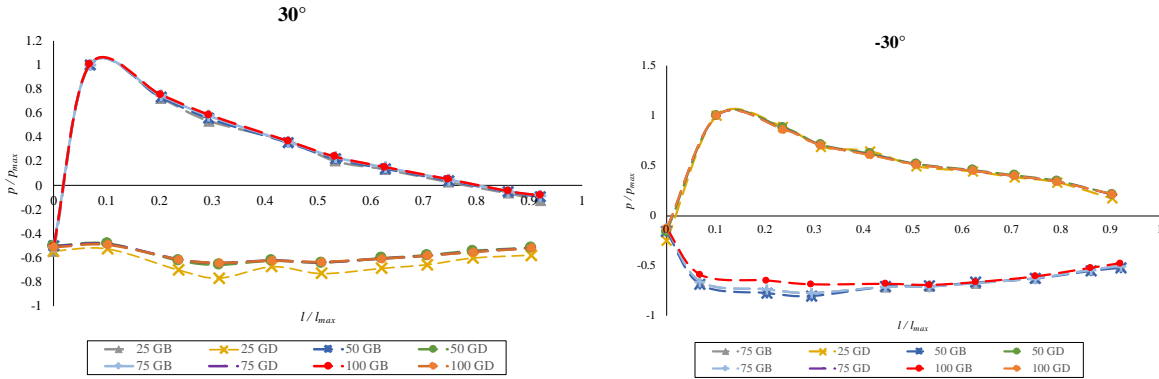


Figure 4-22. Unit pressure profile at attack angle  $+30^\circ$  (left) and  $-30^\circ$  (right)

The solitary aerofoil results demonstrate the influence of the aerofoil placement in the flow field on the magnitude and direction of the aerodynamic forces.

At larger positive angles ( $+20^\circ$  and  $+30^\circ$ ) there is overpressure almost on the entire lower (in this case back) surface of the aerofoil where the impact point - the highest overpressure - occurs at about 7% of the length of the aerofoil. At an angle of  $+10^\circ$ , there is overpressure in the first 30% of the aerofoil length, with the highest intensity at 7% of the profile length, as well as for  $+20^\circ$  and  $+30^\circ$ , and then leading to vacuum pressure. For these attacking angles, vacuum pressure occurs on the upper (front) side of the aerofoil along its entire length. Existence of overpressure on the lower side and vacuum pressure on the upper side will cause a positive lift force.

At larger negative attack angles ( $-20^\circ$  and  $-30^\circ$ ), there is overpressure on the entire upper side with an impact of 9% of the aerofoil length. At an attack angle of  $-10^\circ$ , there is less pressure on the upper side with impact on the leading edge. For these negative attack angles, there is vacuum pressure on the entire lower (back) surface, which for  $-30^\circ$  is with almost the same intensity, and for  $-10^\circ$  and  $-20^\circ$  is greater than 7% of the length of the aerofoil. The presence of overpressure on the lower side and overpressure on the upper side indicates the occurrence of a negative lift force.

At small angles of  $\pm 5^\circ$  there is mainly overpressure on both sides of the profile, except in the initial part where there is overpressure - impact on the leading edge. For  $+5^\circ$ , the intensity of the pressure is higher on the upper (front) than on the lower (back) side, due to which a positive lift force will appear. At an attack angle of  $-5^\circ$ , there is more vacuum pressure on the lower side, due to which the lift force will be negative. The induced lift force at such small attack angles will be less intense because there is a similar trend of pressure change between the two sides and without significant differences.

From the comparison between the forms of pressure distribution for the solitary aerofoil for a given angle of attack, it can be seen that at different flow modes (100% - highest air flow, 25% - lowest air flow) similar shapes of pressure profiles are obtained on pressure, both on the lower and on the upper surface. The differences are in the intensity of the values of the absolute pressures for different flow modes. Therefore, it can be concluded that the forms of pressure distribution remain the same for the same position (attack angle) of the aerofoil in the flow field, regardless of the fluid flow. Therefore, for a solitary aerofoil at a given angle of attack, unit

pressure profile is defined, which is the mean value of the unit pressure profiles obtained under different operating modes.

For the analytical determination of the resulting aerodynamic force of the aerofoil, the calculation model described in Chapter 3 is applied (Chapter 3.2.3). To define a (solitary aerofoil) pressure function depending on the length of the aerofoil curve for a given angle of attack, the experimentally obtained values of pressure at the measuring points are used to obtain four polynomial functions  $p(l)$  each of which applies to a given segment of the aerofoil surface (two polynomial functions  $p(l)$  for each side of the aerofoil), Figure 4-23. At the same time, the aerofoil is described by polynomial functions for different intervals of curve length.

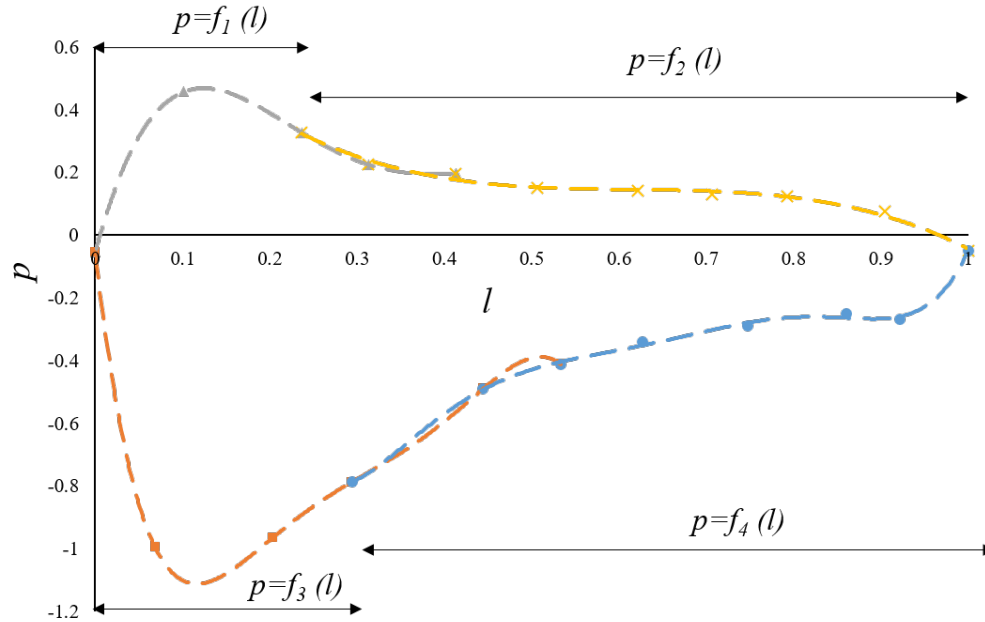


Figure 4-23. Defining functions of a unit pressure profile for individual segments of the aerofoil length, for a given angle of attack

After integrating according to the model for calculating forces and moments, the lift force (Figure 4-24), the drag force (Figure 4-25), and the moment relative to the leading edge of the aerofoil (Figure 4-26) are obtained for different attack angles. At positive attack angles, there is a positive resultant force, and, therefore, a negative moment in relation to the leading edge of the aerofoil and the lift force is in a positive direction. At negative attack angles, there is a negative resultant force and a positive moment in relation to the leading edge of the aerofoil, and a lift force with a negative direction. The lift force and drag force increase with increasing angle of attack (in both directions) relative to the zero position.

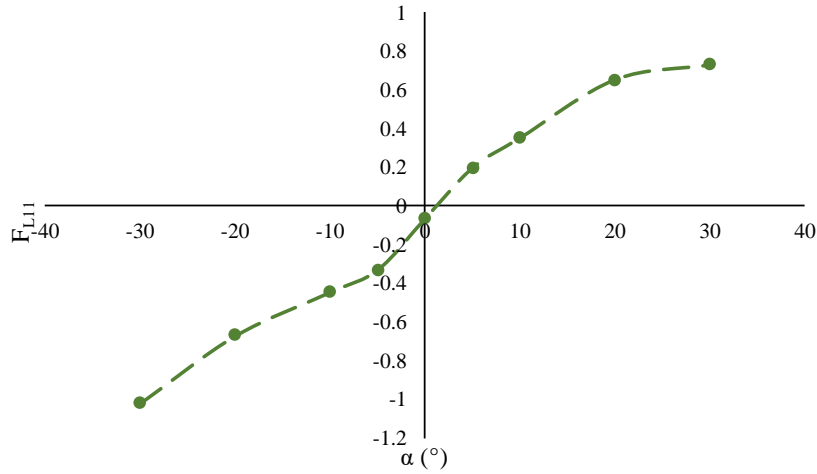


Figure 4-24. Change of lift force depending on the aerofoil attack angle

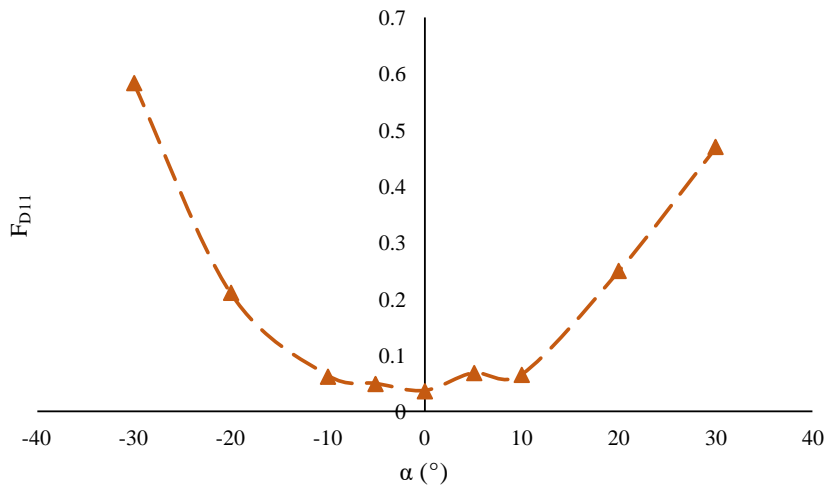


Figure 4-25. Change of drag force depending on the aerofoil attack angle

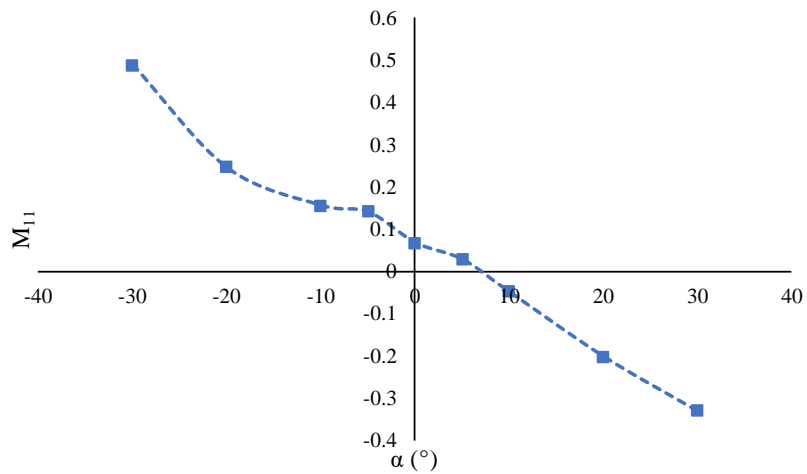


Figure 4-26. Moment change at different attack angles of the aerofoil

### 4.3.2 Aerofoil in a radial cascade

The aerofoil is set in cascade with different pitch i.e. cascades with the following density are experimentally investigated:

- Cascade with density  $t/L > 1$ : the position of the aerofoil in the flow field is such that it can be considered as a solitary aerofoil set in a space with radial boundaries (walls);
- Cascade with density  $t/L < 1$ : the existence of the neighboring blades affects the forces acting on the aerofoil.

#### 4.3.2.1 Radial cascade with density $t/L > 1$

The cascade with low density  $t/L > 1$ , i.e. higher pitch  $t$  is equivalent of a single airfoil in a radial channel. The investigation of air flow in such cascade is performed by changing the inlet and outlet radius of the cascade  $R_1$  и  $R_2$ , so as the flow stream inlet angle  $\alpha_1$  and consequently the angle  $\beta_1$  depending on the upper control blade position and the lower horizontal wall of the channel (Figure 4-27).

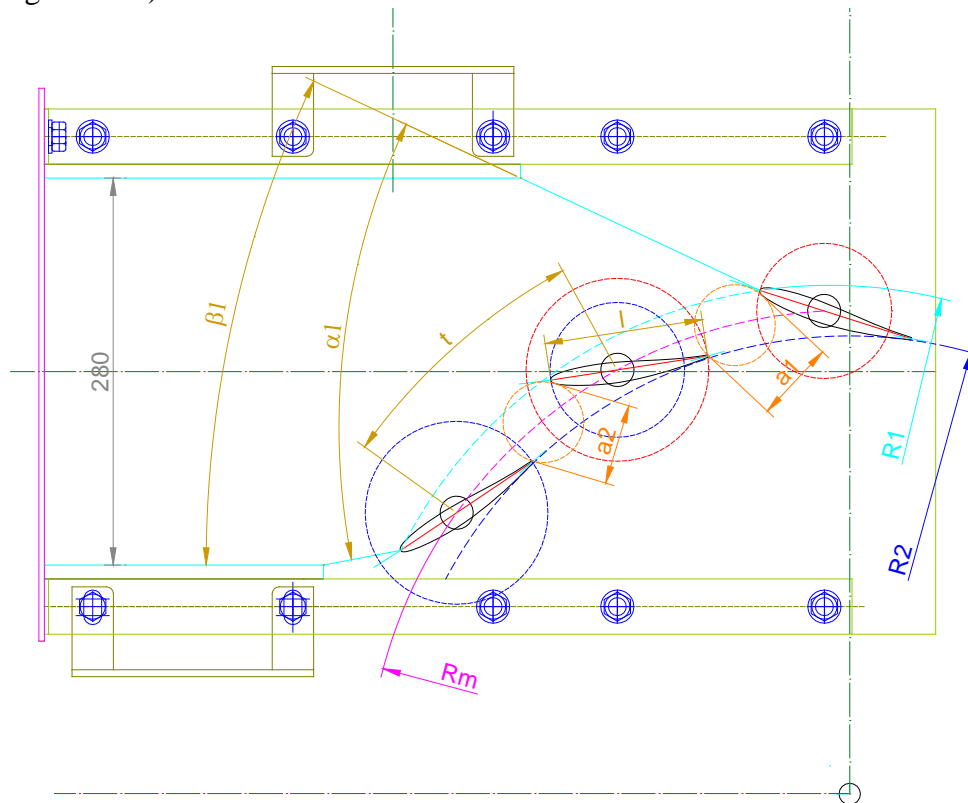


Figure 4-27. Position of aerofoils on a lower density cascade and geometric parameters

The fluid flow domain is defined by setting a different position of the end blades while the central (measuring) blade is positioned to be provided with shock-free inflow by ensuring highest pressure at the leading edge measuring point. Applying this procedure, shock-free inlet flow conditions for the aerofoil in different radial cascade configurations are provided. The low density radial cascade configurations examined are described by their geometric parameters given in Table 4.

Table 4. Geometrical parameters for different case position (model)

MODEL	$R_1$	$R_2$	$a_1$	$a_2$	$\alpha_1$	$\beta_1$
	(mm)	(mm)	(mm)	(mm)	(deg)	(deg)
SR-80	387,9	303,9	106,9	98,4	52,1	18,5
SR-77	383,8	310,2	97,8	90,9	47,8	20,1
SR-68	370,9	331,1	84,6	69	35,9	25,1
SR-01	392,7	295,9	100,5	107,9	56,7	16,5
SR-03	380,7	315,2	81	80,7	44,5	21,5
SR-02	368,7	334	59	61	34,2	26

The measured values of the aerofoil pressure distribution are given in relation to the maximum achieved pressure in the respective radial cascade configuration i.e. as relative values  $p/p_{max}$ , given in Figure 4-28.

The obtained results show that the shock-free entry is achieved and that the suction side is more affected by the radial channel than the pressure side for which the pressure distribution is slightly aligned. These results are confirming the influence of the radial channel geometric parameters on the aerofoil pressure distribution.

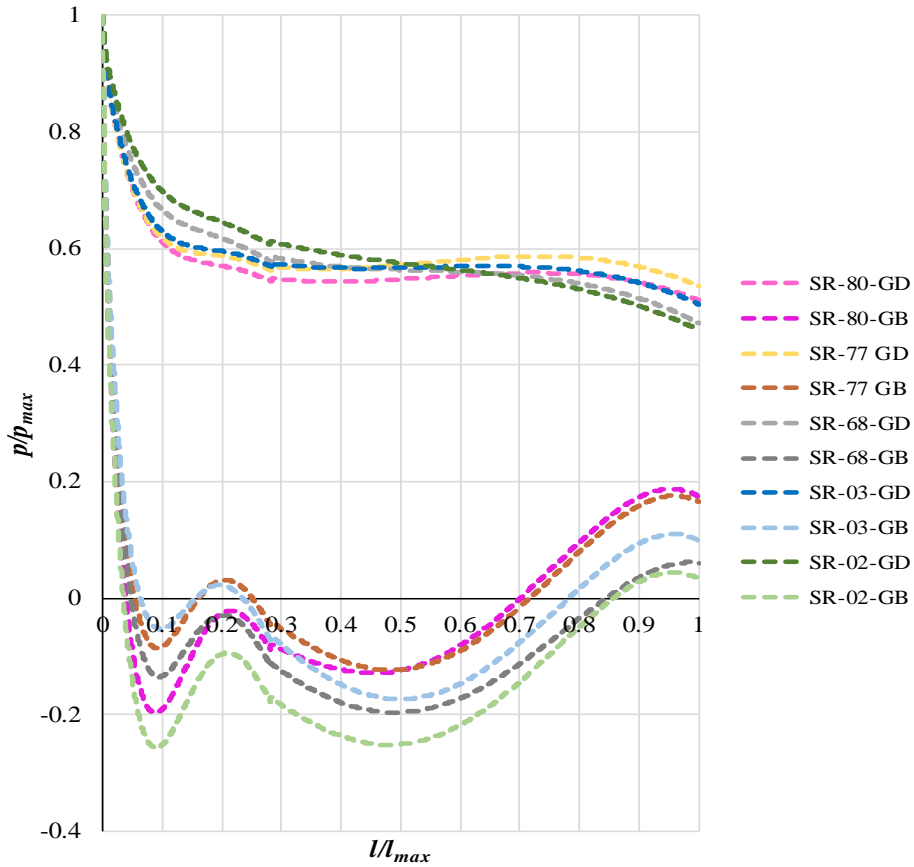


Figure 4-28. Aerofoil pressure distribution for different lower density radial cascade configurations

The law of forces distribution along the aerofoil set in a radial cascade with high pitch is presented in Figure 4-29.

A big difference between the force distribution along a single aerofoil in a straight channel and the same aerofoil set in radial channel for shock-free inflow conditions can be noted. From point of view of strength analysis, higher loads are obtained by setting the aerofoil in the low density radial cascade because of the radial boundaries.

The law of force distribution along the aerofoil in the radial channel is identical for every cascade configuration, however, there is no exact matching, but certain difference ('layering') resulting from the different geometric parameters between the configurations.

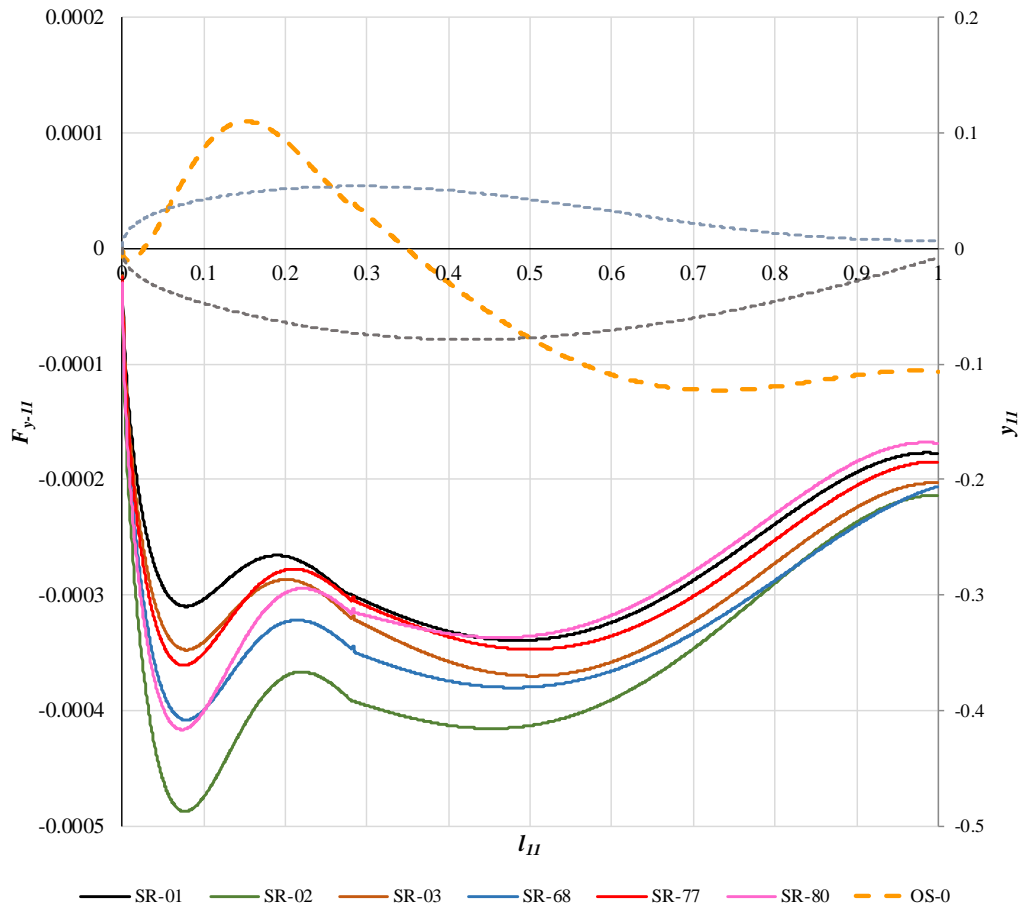


Figure 4-29. Normal force distribution along the aerofoil in lower density cascade

The magnitude of normal force  $F_{y11}$  and moment  $M_{11}$  are determined by the developed calculation model presented in Chapter 3. Their dependence on the inlet and outlet radius ratio  $R_1/R_2$  (i.e. on the cascade relative width) is shown in Figure 4-30 and Figure 4-31.

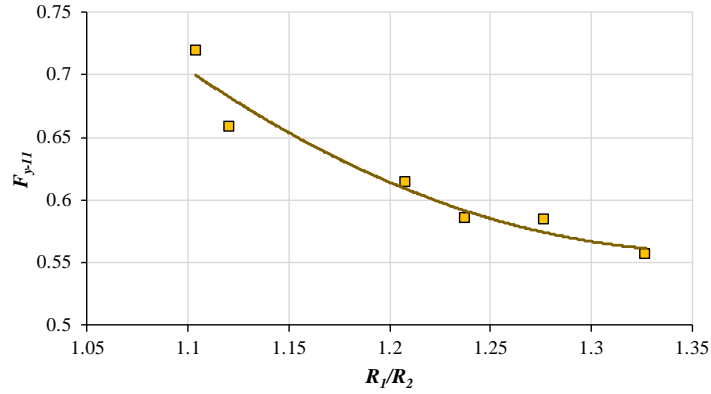


Figure 4-30. Aerofoil normal force magnitude for different lower density cascade relative width

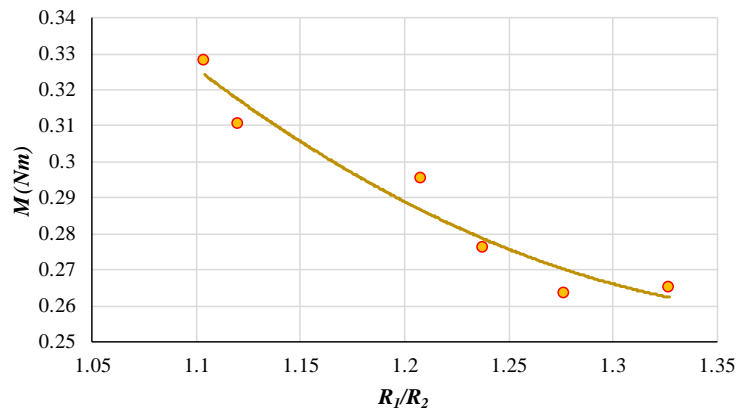


Figure 4-31. Aerofoil moment magnitude for different lower density cascade relative width

By increasing the cascade relative width, the normal force and the moment are decreasing.

The dependence of the magnitude of the normal force and moment acting on the aerofoil on the ratio of opening to aerofoil length  $a/l$  (i.e. relative opening) is given in Figure 4-32 and Figure 4-33.

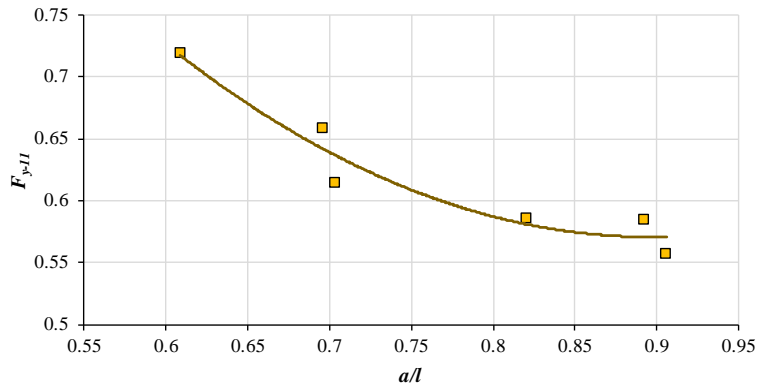


Figure 4-32. Aerofoil normal force magnitude for different relative opening of lower density cascade

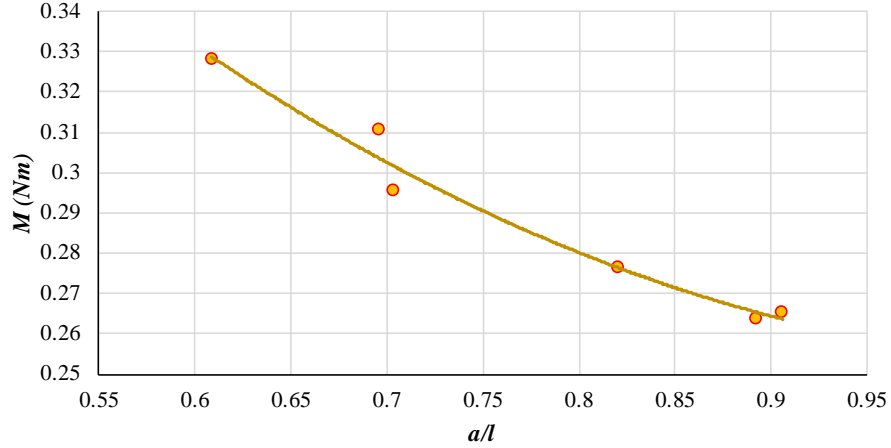


Figure 4-33. Aerofoil moment magnitude for different relative opening of lower density cascade

It is noted that the relative opening increment also leads to loads reduction.

From the obtained results, it can be concluded that there is a dependency between the mechanical quantities  $F_{y11}$  and  $M_{11}$ , and the radial channel geometric parameters which can describe the different conditions.

Taking into account the different radial cascade configurations given in Table 4, a radial cascade coefficient  $K_R$  is introduced to describe the conditions in the cascade by its geometric parameters (relative width  $R_1/R_2$  and relative opening  $a/L$ ):

$$K_R = \left[ \left( \frac{a}{L} \right)^{R_1/R_2} \right]^n \quad 4-13$$

A corrected normal force distribution  $F_{y11-k}$  can then be established by dividing the normal force values with the radial cascade coefficient:

$$F_{y-11-k} = \frac{F_{y-11}}{K_R} \quad 4-14$$

The results for  $F_{y11-k}$  for different low density radial cascade configurations is given in Figure 4-34.

Comparison between the calculated normal force distribution (solid line) and corrected normal force distribution (dashed line) along the aerofoil in the low density radial cascade is given in Figure 4-35. The value of the exponent  $n$  in the radial cascade coefficient expression is determined by trials to be  $n=0,45$ .

By introducing the radial cascade coefficient, better alignment of the law of the normal force distribution along the aerofoil in radial cascade is achieved i.e. defining of the aerofoil strength conditions.

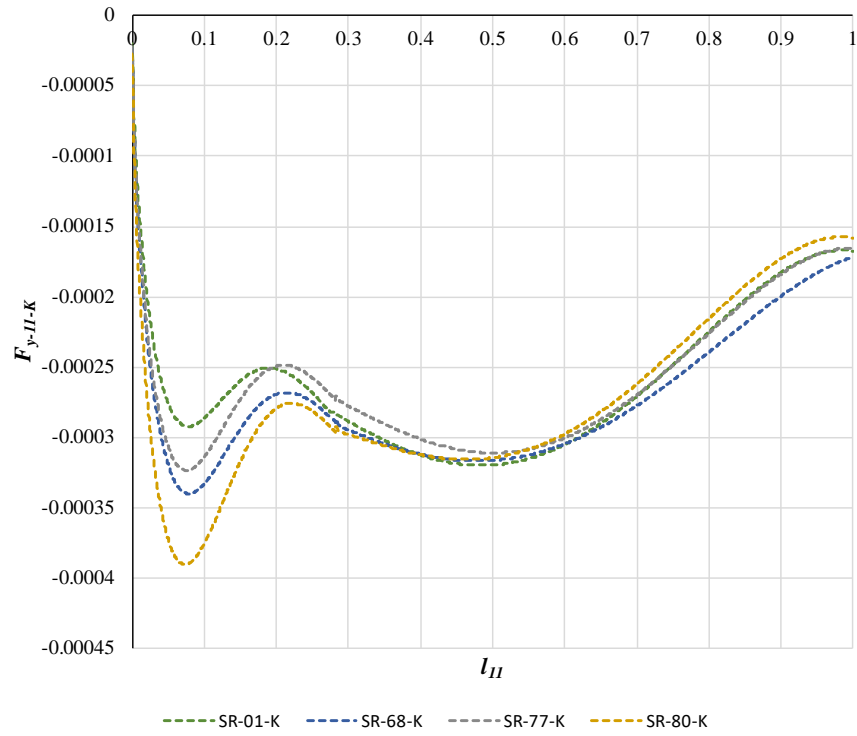


Figure 4-34. Corrected normal force distribution for different cascade configurations

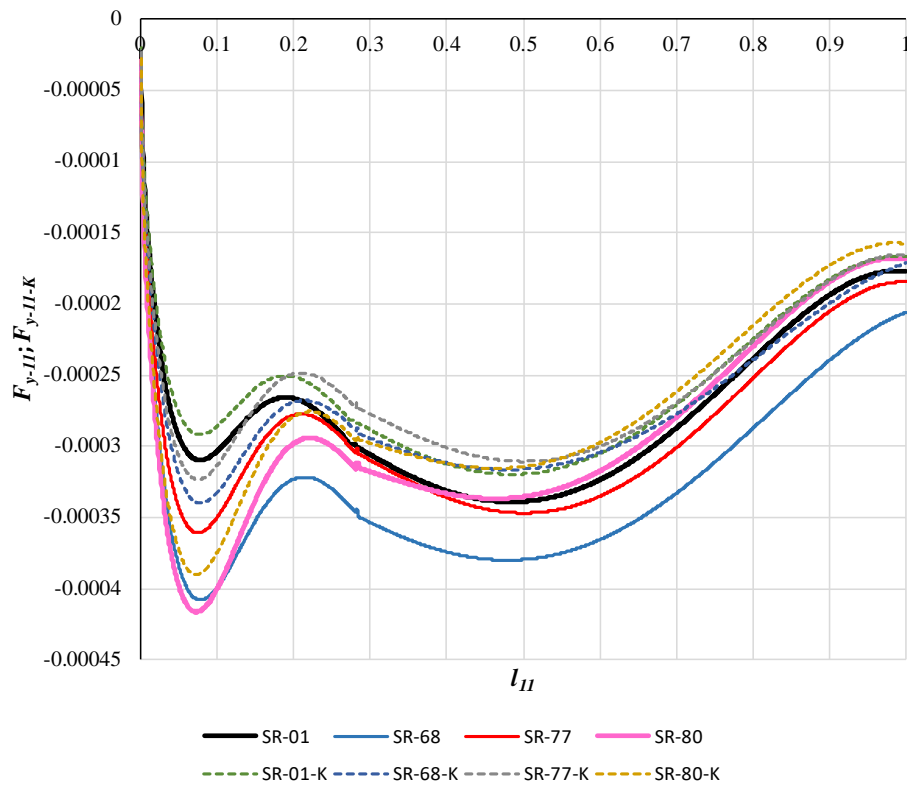


Figure 4-35. Comparison between calculated and corrected normal force distribution along the aerofoil set in low density radial cascade

#### 4.3.2.2 Radial cascade with density $t/L < 1$

The pressure distribution along the profile surface in a circular cascade depends on the position of the profile in the flow field.

Before measuring the pressures on the surfaces of the central blade in the cascade, the symmetry of the flow in the two inter-blade channels formed by the central blade was checked by confirming the identity of the pressure profiles of the central and control blades. At the same cascade pitch, the openness changes, i.e. the angle of rotation of the blades (Figure 4-36). Thereby, with the help of the control blades, conditions of shock-free inflow were achieved in all positions.

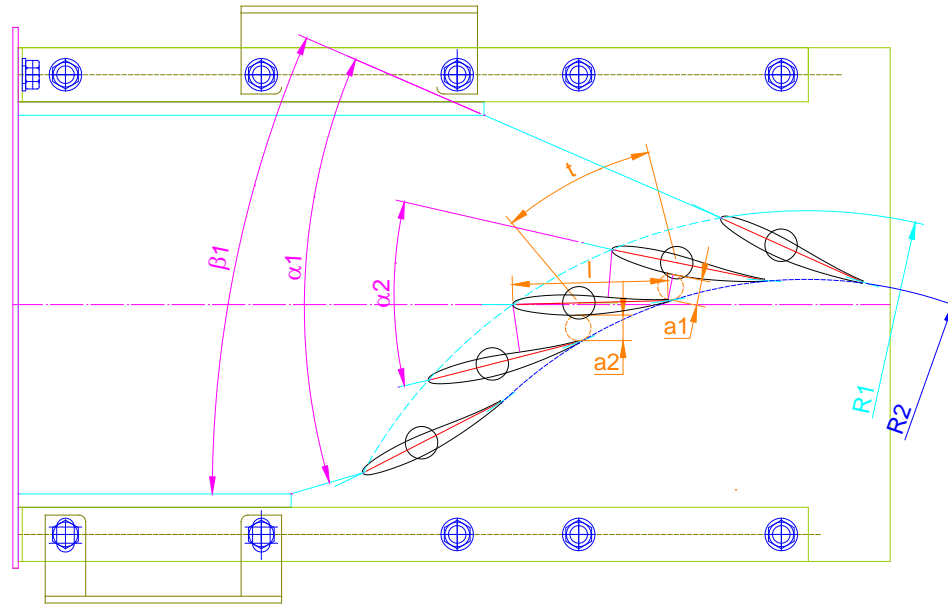


Figure 4-36. Position of aerofoils in higher density cascade and geometric parameters

Zero position  $0^\circ$ , three positions in the direction of opening the blades ( $5^\circ$ ,  $10^\circ$  and  $20^\circ$ ) and two positions in the direction of closing ( $-5^\circ$  and  $-10^\circ$ ) were examined, each with three different flow modes. The cascade geometric parameters for the high density radial cascade configurations are given in Table 5.

Table 5. Geometrical parameters for case position-shock free inflow

MODEL	$R_1$	$R_2$	$a_1$	$a_2$	$\alpha_1$	$\alpha_2$	$\beta_1$
	(mm)	(mm)	(mm)	(mm)	(deg)	(deg)	(deg)
TR-00	375,9	324,2	18,9	18,9	40,2	25,7	23,4
TR-05	372,5	329,8	13,1	13,1	36,8	25,7	24,7
TR-10	369	334,5	7	7	34,1	25,7	26
TR+05	379,2	318,8	22,5	22,5	42,9	25,7	22,1
TR+10	382,6	313,6	29	28	46,1	25,7	20,9

The measured pressures at the ten points distributed along the back and front surfaces of the central blade are given in relation to the maximum pressure at the corresponding mode (which in these cases is achieved at the front edge – shock-free entrance), i.e. as relative values so that the obtained pressure profiles be comparable. The position of the measuring points is given relative to the unit length of the profile. The relative pressure distribution of the profile, i.e. unit pressure profiles, reduced to unit total length of the profile for different openings is given in Figure 4-37.

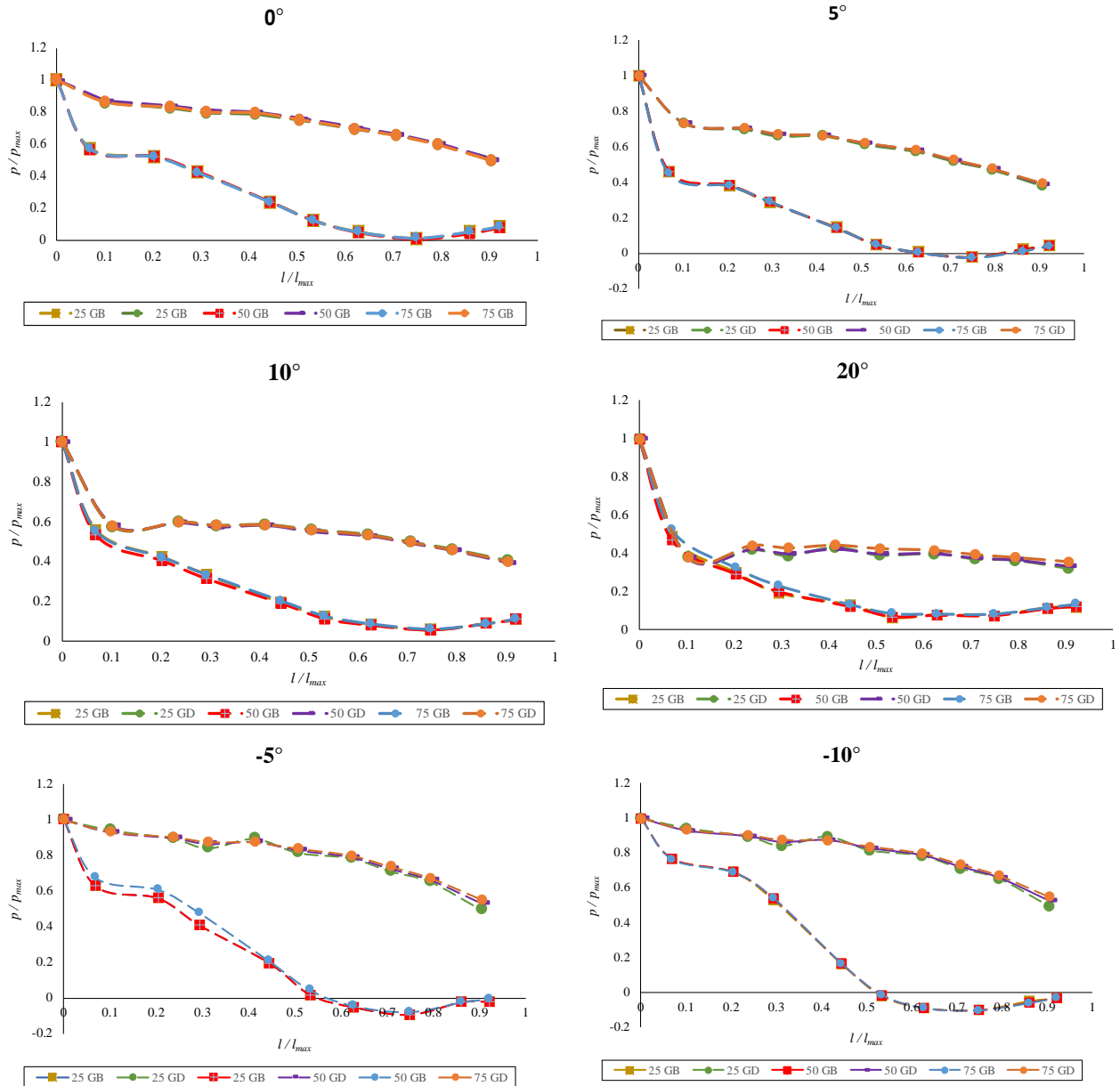


Figure 4-37. Unit pressure profiles of central blade at different openings of the higher density circular cascade

The flow uniformity in the inter-blade channels is confirmed to be achieved by comparing the pressure on both aerofoil surfaces. An example is given in Figure 4-38 for blade position  $-10^\circ$  in the cascade.

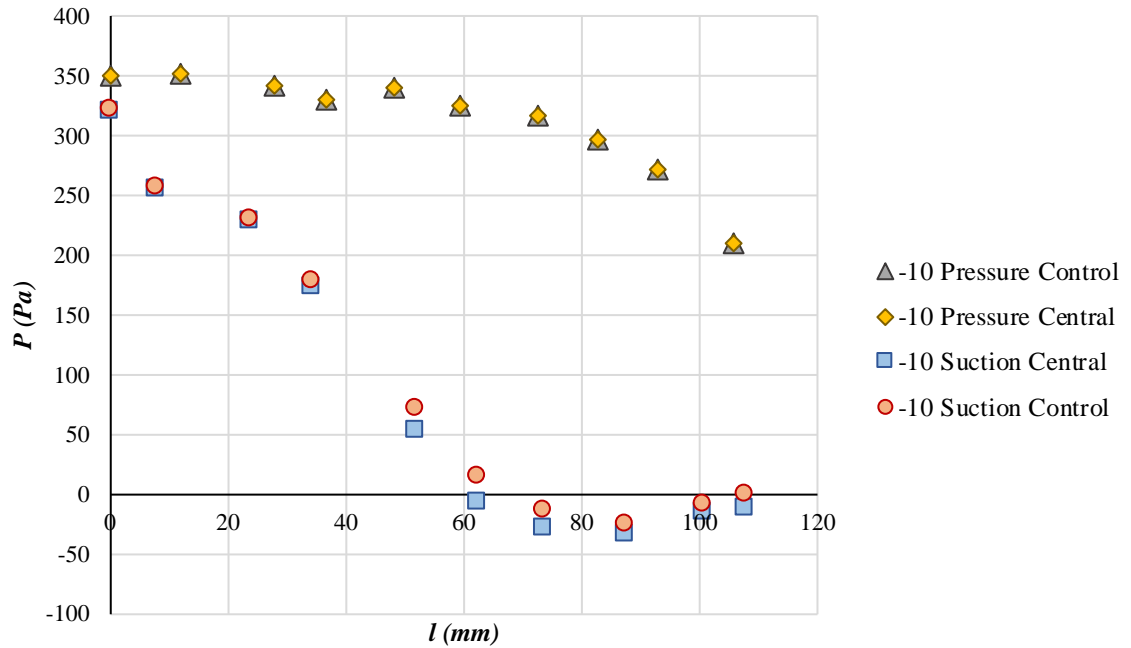


Figure 4-38. Pressure distribution comparison for central and control blade

From the comparison between the forms of pressure distribution for the central blade in the cascade at a given opening, it can be seen that under different flow modes similar shapes of pressure profiles are obtained. The differences are in the intensity of the values of the absolute pressures for different flow modes.

The normal force distribution along the aerofoil in radial cascade with higher density is given in Figure 4-39.

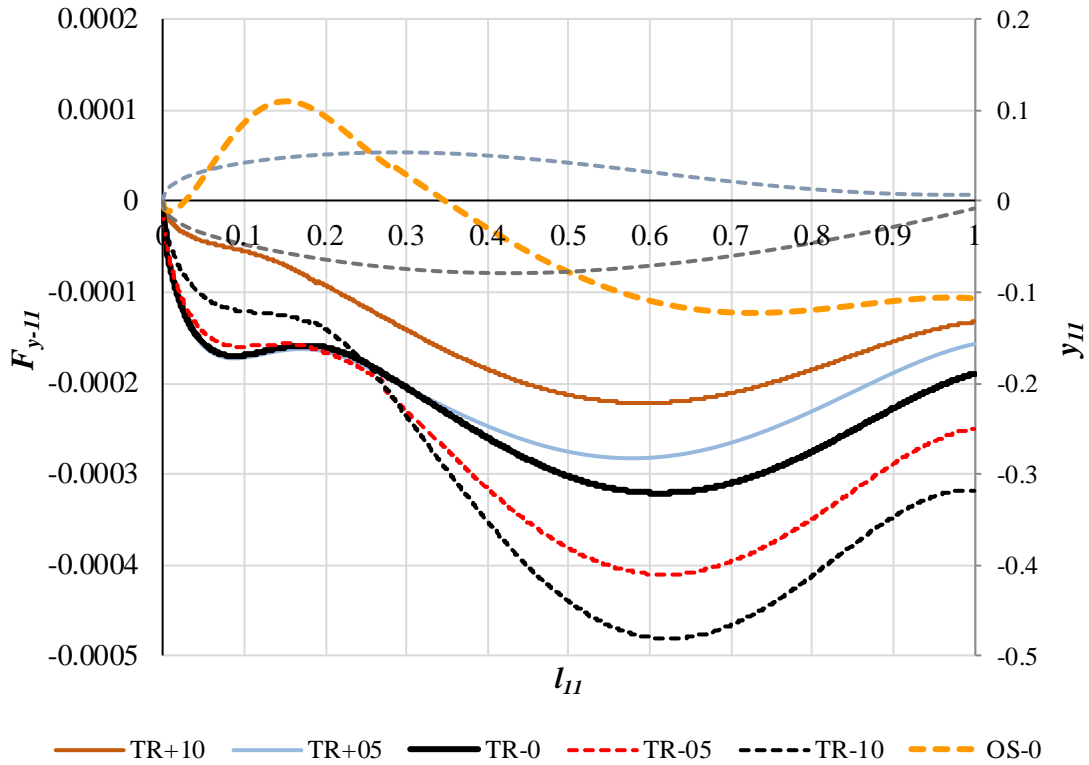


Figure 4-39. Normal force distribution along an aerofoil in higher density radial cascade

The results obtained show that the distance between two neighboring blades slightly affects the force (loads) distribution. Higher difference between the forces distribution for different cascade configurations is obtained on the part of the aerofoil which contributes to forming the interblade channel. The aerofoil overlapping length  $l_p$  change according to the radial cascade configuration is presented in Figure 4-40.

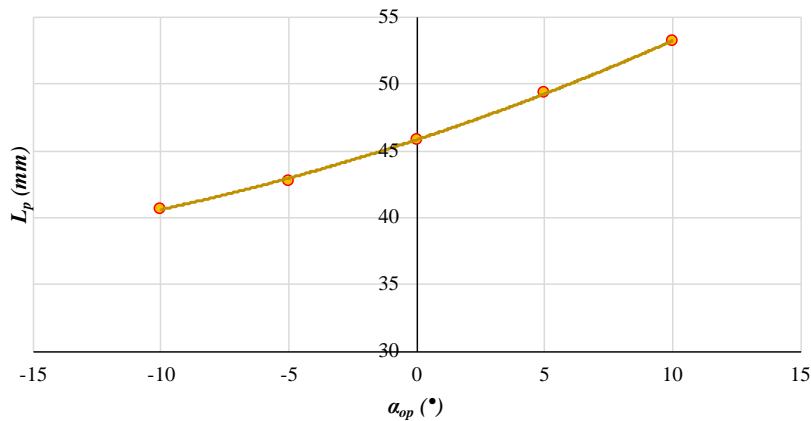


Figure 4-40. Aerofoil overlapping length variation with higher density cascade configuration

Higher overlapping length provides more uniform flow and smaller forces (loads) on the aerofoil.

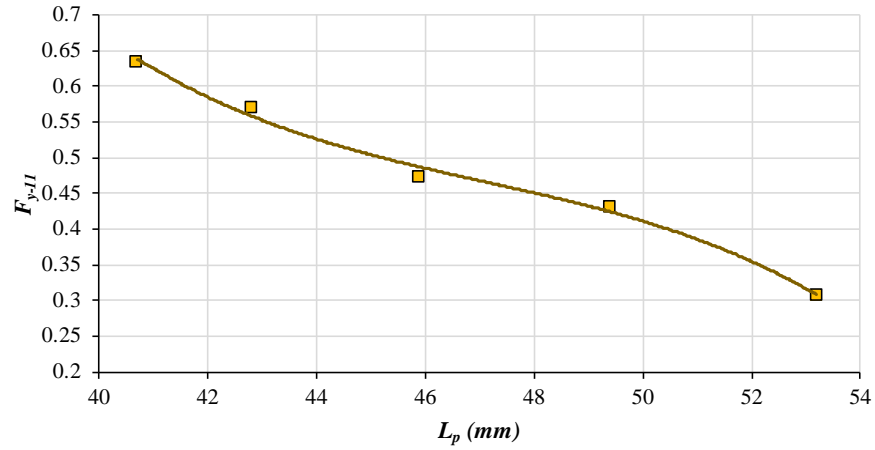


Figure 4-41. Aerofoil forces distribution dependence on overlapping length

By using the radial cascade coefficient, corrected forces distribution along the aerofoil in the high density cascade is obtained (Figure 4-42) and compared to the calculated forces distribution, shown in Figure 4-43.

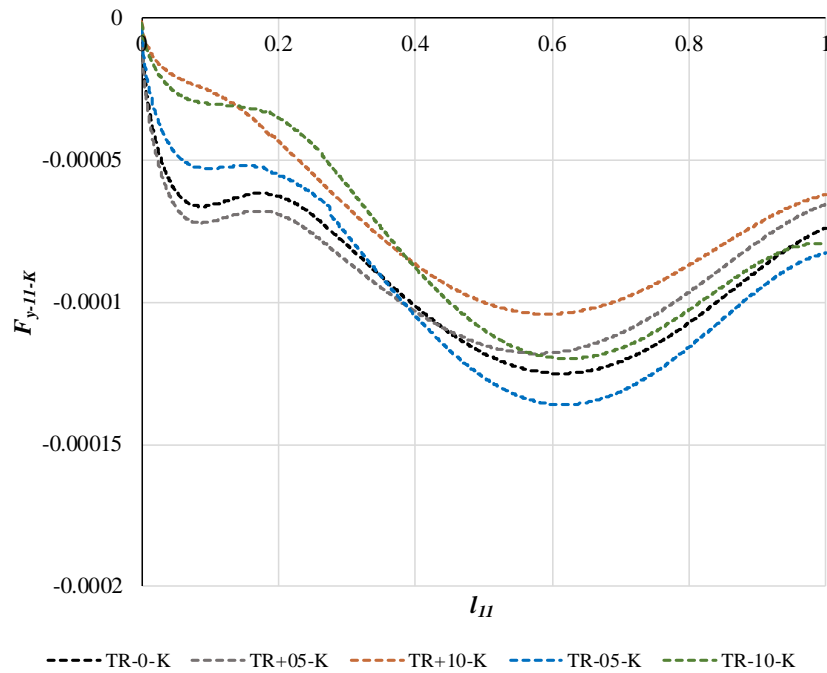


Figure 4-42. Corrected normal force distribution for different high density cascade configurations

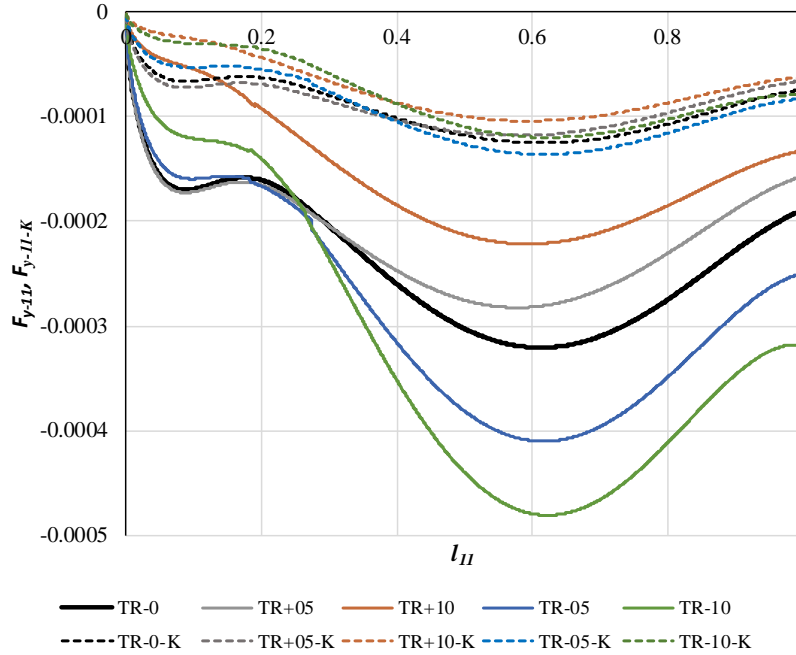


Figure 4-43. Comparison between calculated and corrected forces distribution along aerofoil in higher density cascade

The corrected aerofoil force distribution of each high density radial cascade configuration are more uniform, meaning that the introduced radial cascade coefficient provides describing the law of aerofoil forces (loads) distribution for the experimentally investigated cascade configuration.

#### 4.3.2.3 Relation between forces distribution in radial cascade with higher density ( $t/L < 1$ ) and lower density ( $t/L > 1$ )

The difference between the radial cascade with higher density and with lower density is the value of the cascade pitch  $t$  which defines the density of the cascade. The corrected forces distribution for both cascades, which was obtained by using the introduced radial cascade coefficient, is shown in Figure 4-44. The mean arithmetic value of the results for each type of cascade is taken as a representative of the corrected forces distribution of the cascade. The analysis is based on the absolute values of the characteristic forces distribution.

For the cascade with lower density ( $t/L > 1$ ), the dimensionless characteristic corrected forces distribution is derived to be:

$$F_{y-11-k-SR} = \frac{abs(F_{y-11-k-SR})^{1,135n}}{l_{11} \left(\frac{t}{l_k}\right)} \quad 4-15$$

while for the cascade with higher density ( $t/L < 1$ ), the dimensionless characteristic corrected forces distribution is derived:

$$F_{y-11-k-TR} = \frac{abs(F_{y-11-k-TR})^n}{l_{11} \left(\frac{t}{l_k}\right)} \quad 4-16$$

where  $t$  is the cascade pitch,  $l_{11}$  is the unit aerofoil chord length,  $l_k$  is the effective (overlapping) aerofoil length,  $n$  is the exponent which for this case considered is 0,02.

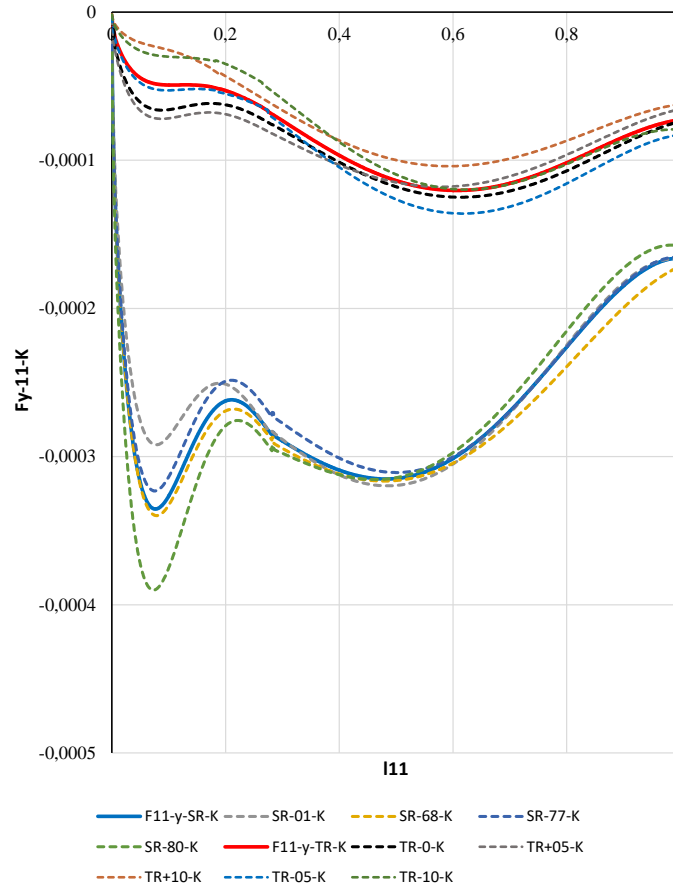


Figure 4-44. Comparison between corrected forces distribution for cascades with higher and lower density

The comparison between the dimensionless characteristic corrected forces distribution for radial cascade with higher and lower density is presented in Figure 4-45.

The ratio between the dimensionless characteristic corrected forces distribution for radial cascade with higher and lower density along the aerofoil unit chord length is:

$$F_{y-11-kk-TR-SR} = \frac{F_{y-11-kk-TR}}{F_{y-11-kk-SR}} \quad 4-17$$

and presented in Figure 4-46.

The correlation between the forces distribution on the aerofoil in a cascade with higher and lower density is obtained by introducing the radial cascade coefficient and the cascade pitch which are described by the cascade geometric parameters. The dependency is an exponential function both in the case of comparing dimensionless forces distribution of cascades with different density between themselves and in case of establishing a ratio between the dimensionless characteristic corrected forces distribution for the different density cascades along the aerofoil unit chord length.

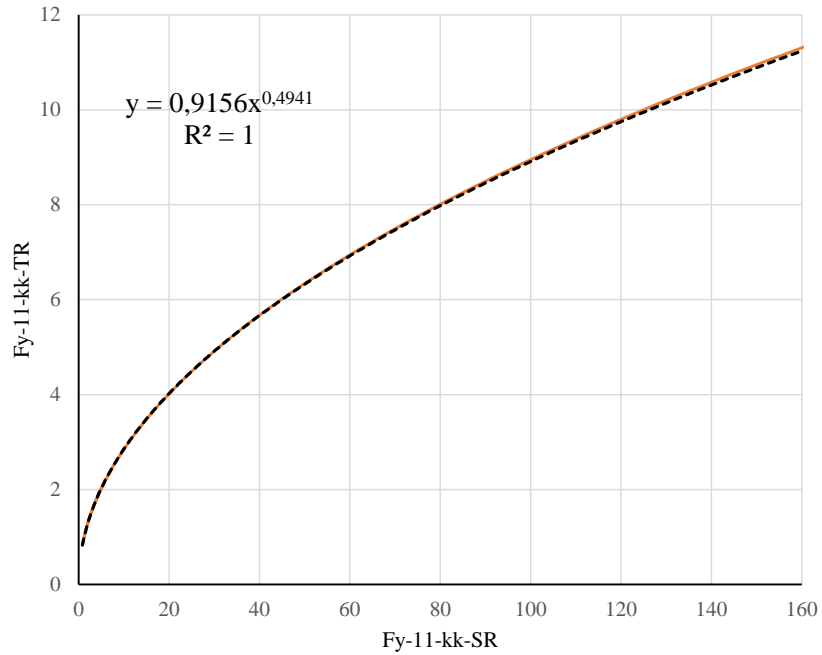


Figure 4-45. Comparison between dimensionless characteristic corrected forces distribution for radial cascade with higher and lower density

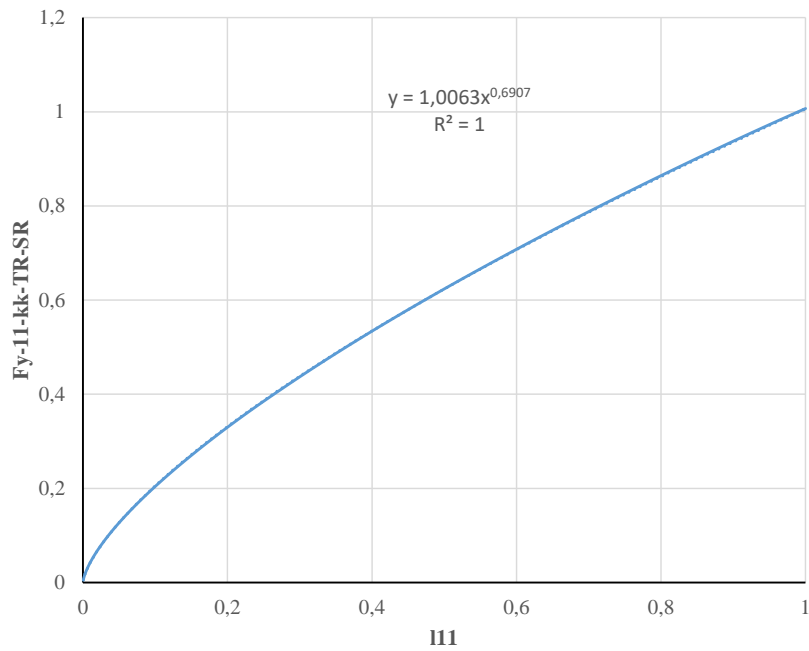


Figure 4-46. Ratio between dimensionless characteristic corrected forces distribution for radial cascade with higher and lower density

The derived correlations allow prediction of the aerofoil load force for different cascade pitch.

4.3.2.4 Relation between forces distribution on solitary aerofoil and aerofoil in a higher relative pitch cascade

Forces  $F_{y-11}$  are taken to be a (base 10) logarithm exponent:

- For a solitary aerofoil:

$$F_{y-11-exp-OS} = 10^{F_{y-11-OS}} \quad 4-18$$

- For a radial cascade with relative pitch  $t/l > 1$ :

$$F_{y-11-exp-SR-k} = 10^{F_{y-11-SR-k}} \quad 4-19$$

according to which a graph of forces distribution along the aerofoil is obtained (Figure 4-46).

Ponder (weighted) forces on basis of the aerofoil length are defined:

- For a solitary aerofoil:

$$F_{y-11-exp-OS}/x_{11} = \frac{F_{y-11-exp-OS}}{x_{11-i}} \quad 4-20$$

- For a radial cascade with relative pitch  $t/l > 1$ :

$$F_{y-11-exp-SR-k}/x_{11} = \frac{F_{y-11-exp-SR-k}}{x_{11-i}} \quad 4-21$$

And the graph for their distribution is given in Figure 4-48 **Error! Reference source not found.** left.

The comparison of ponder (weighted) forces of solitary aerofoil and radial cascade with higher relative pitch is given in Figure 4-48 right.

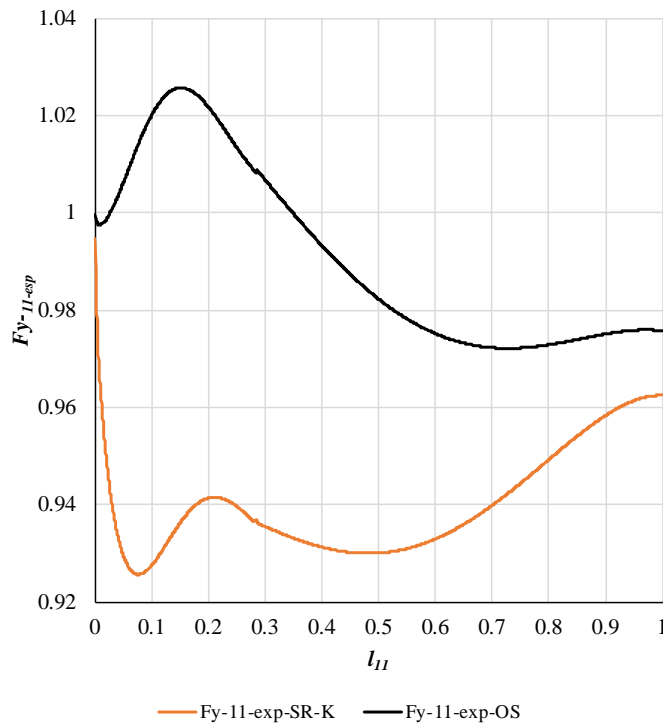


Figure 4-47. Forces distribution along solitary aerofoil and aerofoil in a cascade with higher relative pitch

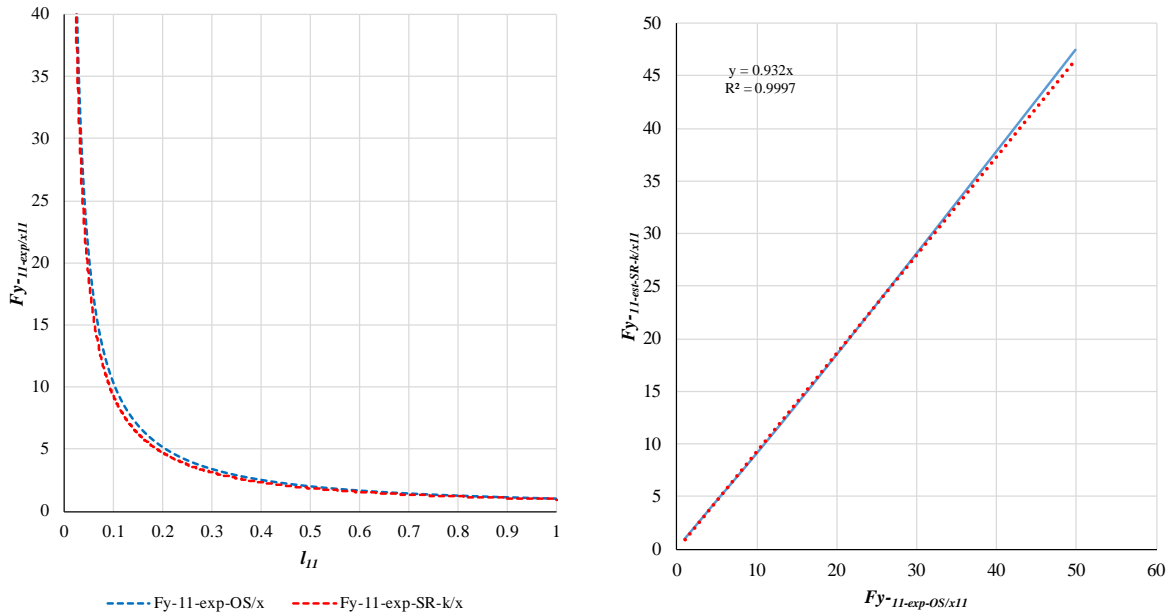


Figure 4-48. Ponder forces distribution on basis of aerofoil length (left) and comparison between a solitary aerofoil and cascade with higher relative pitch

The load force along the solitary aerofoil is in positive and negative direction in different parts of the aerofoil so intersection points with the apsis occur (zero value) which leads to more complicated mathematics. By applying the ponder forces along the aerofoil which are obtained by inserting the load force as a logarithmic function exponent and the introduced radial cascade coefficient, a correlation between the solitary aerofoil and the aerofoil in the cascade with higher relative pitch is established.

The results show linear dependence between the load force of a solitary aerofoil and aerofoil in a cascade, thus the prediction of the loads on an aerofoil in a radial cascade when the solitary aerofoil loads are known is shown to be possible.

## 5 Numerical research

On the one hand, experimental research of scaled models in wind tunnels or test installations is a more economical alternative to real-time experimental performance testing, and on the other hand, they play an important role in validating equations that mathematically describe flow processes, i.e. Navier-Stokes equations, which are so complex that no analytical solution can be obtained for most practical applications.

Advances in computer technology in the 1950s led to the emergence and development of the CFD (Computational Fluid Dynamics) technique, which analyses fluid flow processes, heat transfer, and chemical reactions using computer simulations. With CFD numerical techniques, partial differential equations have been replaced by systems of algebraic equations that are much easier to solve using computers. This provides a more economical test of fluid flow systems.

### 5.1 Numerical modelling of flow around a solitary profile in a wind tunnel

Numerical modelling and simulation of two-dimensional airflow around the aerofoil in the channel from the experimental installation was performed. The thermo-physical properties of air are taken to be subjected to the law of ideal gas, i.e. temperature and pressure-dependent. Initial limit conditions are mass flow and inlet temperature and atmospheric outlet pressure. The standard k- $\epsilon$  model of turbulence is used to describe the turbulent flow. A boundary layer is placed around the aerofoil surfaces, and the numerical grid is hexagonal with pave-method (Figure 5-1).

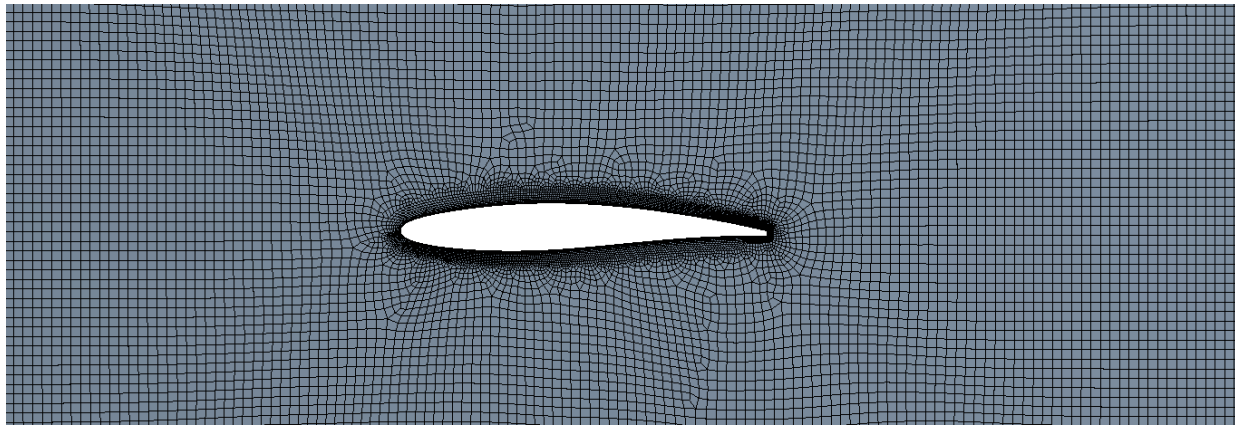


*Figure 5-1. Numerical model of flow around a solitary profile in an air tunnel*

The numerical model is validated by comparing the results with the experimental data for the solitary aerofoil positioned at zero attack angle. The verification of the results for the upper and lower aerofoil surface is presented in Figure 5-1 and Figure 5-2. While most of the measured values show difference compared to the numerical values in acceptable range (0,5%-14%), the second and third measuring point show higher deviation for the lower surface pressure distribution.

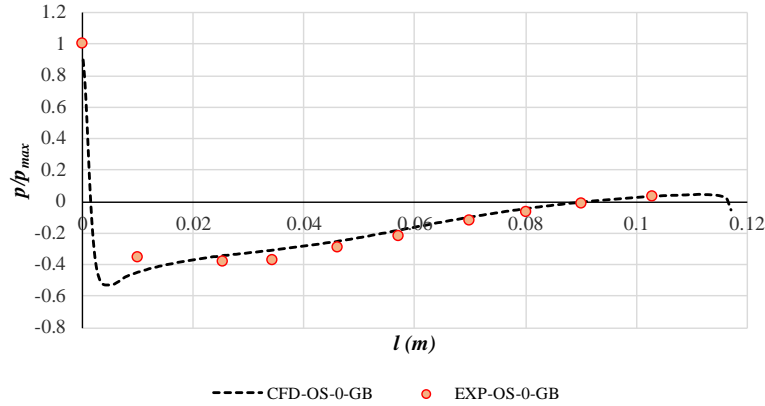


Figure 5-1. Comparison of experimental and numerical results for aerofoil upper surface at  $0^\circ$  attack angle

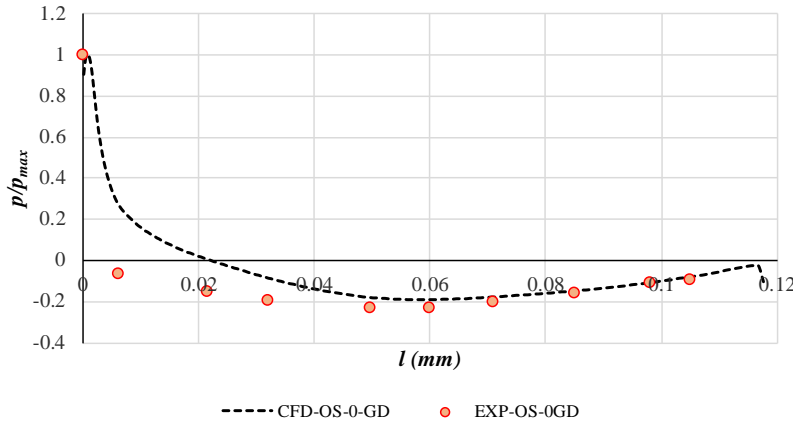


Figure 5-2. Comparison of experimental and numerical results for aerofoil lower surface at  $0^\circ$  attack angle

The experimental and numerical values of the lift force, the drag force and the moment at different aerofoil positions are compared (Figure 5-3 and Figure 5-4) and show 3%-28% discrepancy, except for attack angles of  $-20^\circ$  and  $-30^\circ$  where higher deviations were obtained. The larger differences between the experimental and numerical results can be due to different actual position of the aerofoil in the experimental system compared to the exact geometric position in the numerical model or different airflow conditions in the channel during the measurement.

At positive attack angles, there is overpressure on the lower surface of the profile and vacuum pressure on the upper surface, which causes a positive lift force. At negative attack angles, overpressure occurs on the upper surface of the profile and vacuum pressure on the lower surface, i.e. negative drag force. In the zero position the lift force is not zero because the profile is asymmetric (Figure 5-3 left).

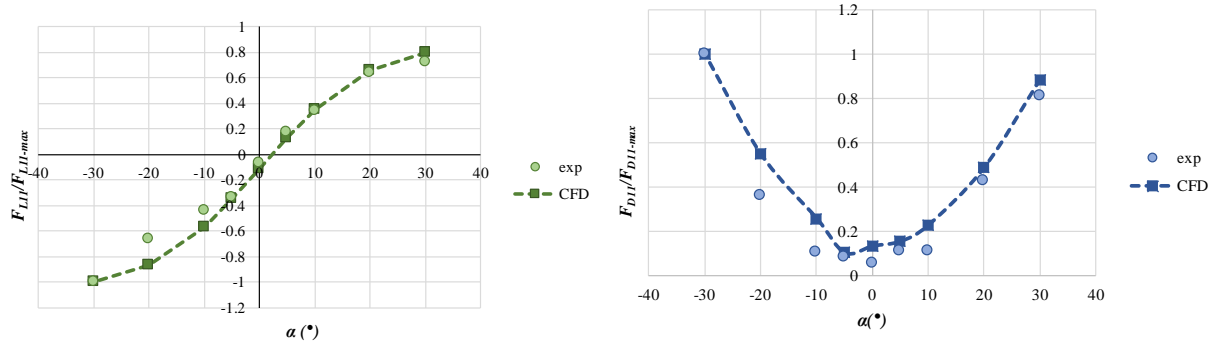


Figure 5-3. Change of lift and drag force depending on the attack angle of the solitary aerofoil

The drag force increases with increase of the aerofoil angle of attack from zero position into negative or positive direction (Figure 5-3 right). The torque acting on the aerofoil leading edge changes linearly depending on the angle of attack (Figure 5-4).

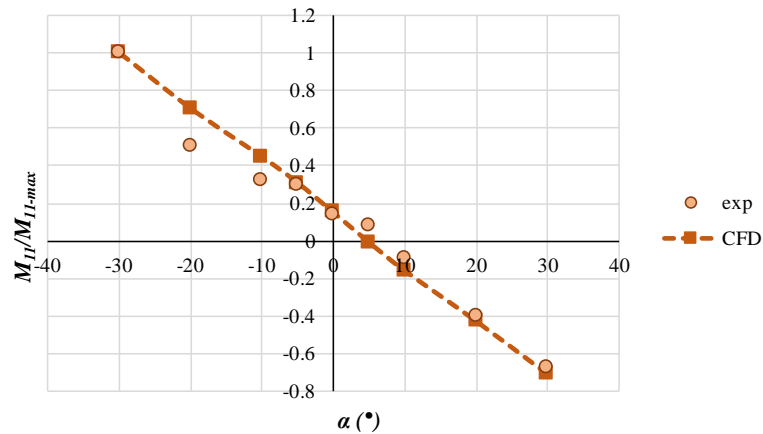


Figure 5-4. Change of the torque acting on the aerofoil depending on the angle of attack

## 5.2 Numerical modelling of the flow around the profile-blade in a radial cascade

To verify the obtained results, the flow around the profiles in the cascade segment in the laboratory is modelled and simulated using CFD. The channel dimensions and the profiles position in the higher density and lower density cascade are used, which corresponds to the position of the profile in the turbine to achieve shock-free flow. The numeric grid is hexagonal, with the pave method having around 90000 cells. A boundary layer is placed around the blades that are subject to analysis. The initial boundary conditions are: constant inlet velocity into the channel with a given air temperature and atmospheric pressure at the exit of the channel. Air is treated as a compressible fluid whose properties change depending on the pressure and temperature according to the equation of state of an ideal gas. The flow is two-dimensional, steady and turbulent. The  $k-\epsilon$  model is used as the turbulence model.

### 5.2.1 Radial cascade with density $t/L > 1$

The airflow in a radial cascade with lower density was numerically analysed for the model 00-68 (Figure 5-5) with geometric parameters as described in Table 4.

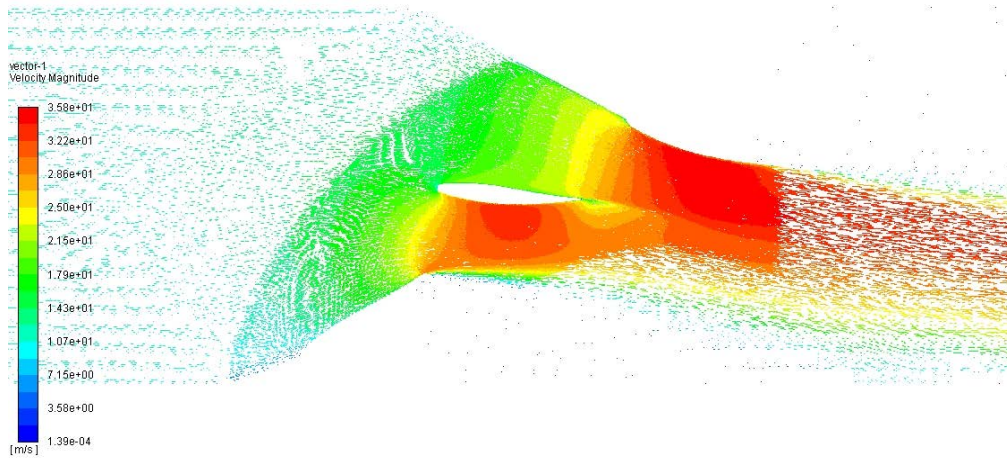


Figure 5-5. Airflow in a lower density radial cascade (model 00-68)-velocity vectors distribution

The numerical model is validated by comparing the numerical pressure distribution and the experimental results for the pressure measured in the measuring points on the upper and lower aerofoil surface. There is a great alignment between the numerically and experimentally obtained values of pressure with a discrepancy up to 7%, presented in Figure 5-6.

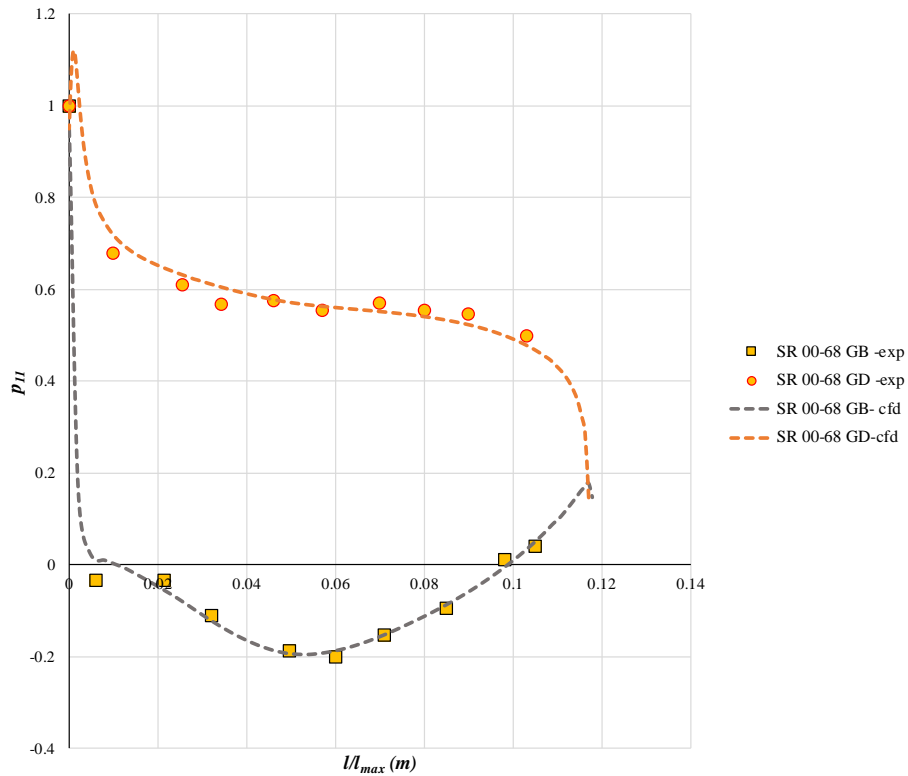


Figure 5-6. Lower density radial cascade numerical model validation (comparison with experimental results)

### 5.2.2 Radial cascade with density $t/L < 1$

The numerical mesh for the higher density radial cascade is shown in Figure 5-7.

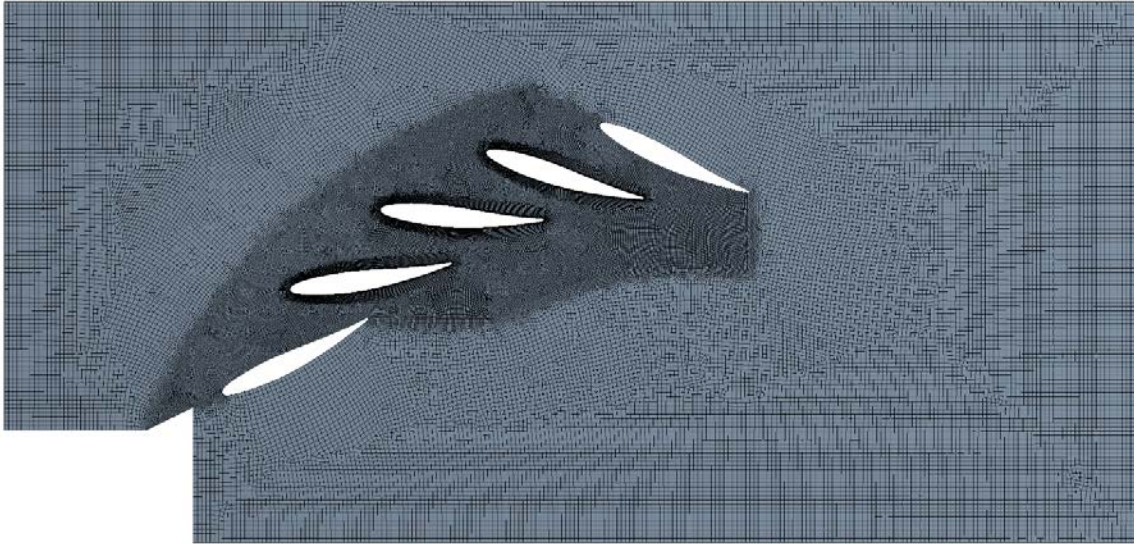


Figure 5-7. Numerical grid-flow domain in the measuring section of the wind tunnel with a radial cascade segment

The comparison between the numerical and experimentally obtained results for the pressure distribution along the profile - the central blade in the higher density radial cascade segment shows alignment (Figure 5-8) thus, the numerical model is validated with deviations less than 1%.

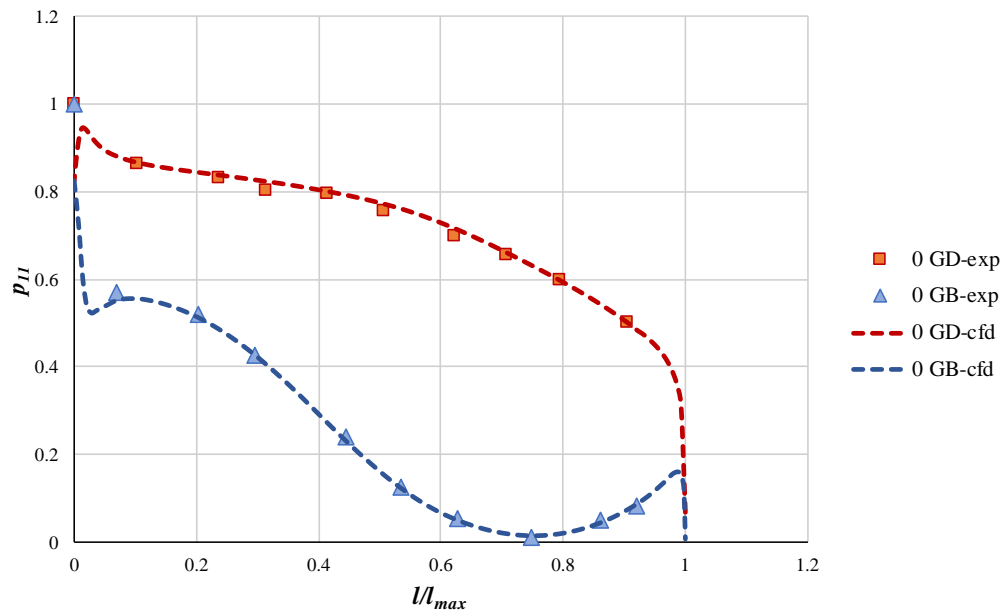


Figure 5-8. Comparison of experimental and numerical results for pressure distribution over profile surfaces

## 5.3 Numerical modelling of fluid flow in Francis turbine guide vane system at different runner rotating speeds

### 5.3.1 Development of a 2D numerical model

#### 5.3.1.1 Description of the turbine model in the laboratory

The Francis-99 turbine model at the Hydropower Laboratory of the University of Science and Technology in Trondheim, Norway (NTNU), was used as the basis for the development of the 2D numerical model for examining the effect of variable speed on the guide vanes' pressure distribution. The spiral casing and stay vanes have been retained in their original shape, while the guide vane shape has been replaced by the blade shape which has been experimentally examined in the framework of this dissertation presented in Chapter 4, maintaining the same dimensions of the available guide vanes space in the turbine model. The spiral casing has an inlet diameter of 338.3 mm. The stay ring consists of 14 blades, while there are 28 guide vanes with an inlet diameter of 764 mm and an outlet diameter of 630 mm. As it is a two-dimensional model, a radial rotating cascade of flat profiles whose shape is taken from the runner blades in the Francis-99 turbine is placed behind the guide vanes (Figure 5-9).

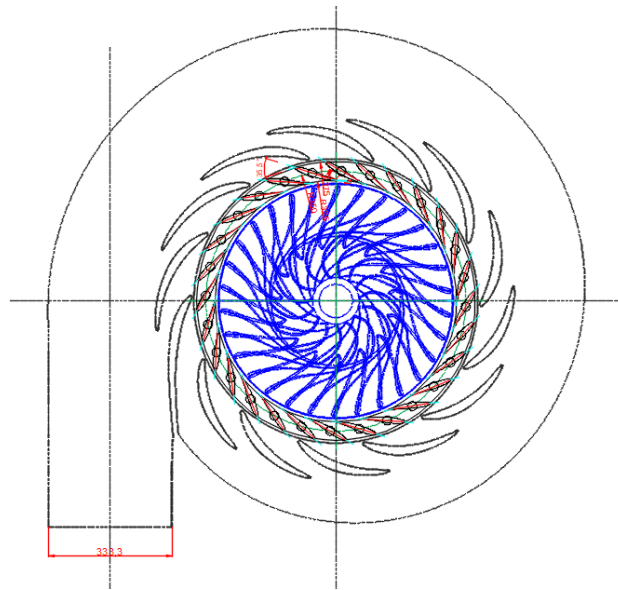


Figure 5-9. Basic parameters of the analysed 2D turbine model

#### 5.3.1.2 Boundary conditions and numerical grid

A two-dimensional steady flow of water through the turbine is simulated. Constant inlet velocity and outlet atmospheric pressure are used as initial boundary conditions. The blades that are subject to analysis are blades no. 7 and 8, and in additional analyses for mutual comparisons, blades no. 5, 9, 21, and 22 are used (Figure 5-10). The spiral case and the stay vanes represent one fluid zone, while the guide vanes and the rotating cascade are separate fluid zones. The connection of two adjacent fluid zones between which there is a fluid passage is achieved with a 'mesh interface'.

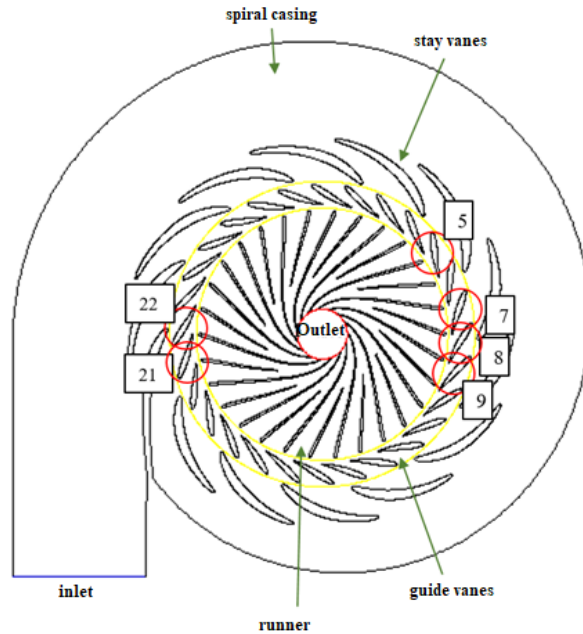


Figure 5-10. 2D numerical model of turbine-boundary conditions

To select an appropriate numerical grid, two grid types were tested: triangular and hexagonal (Figure 5-11). A boundary layer is placed around the stay vanes, the guide vanes and the runner blades.

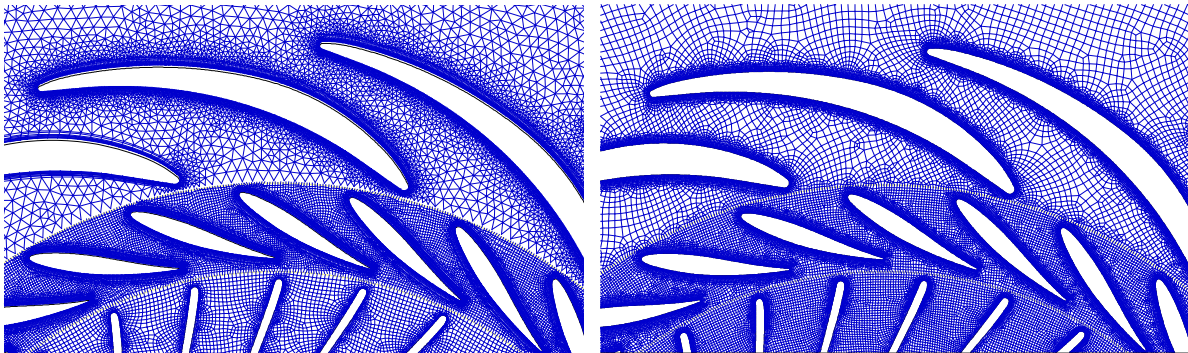


Figure 5-11. Triangular and hexagonal grid of a 2D turbine model

The selection of the hexagonal grid is made based on the size of the residuals. By applying a triangular grid, larger residual values are obtained compared to the hexagonal grid (Figure 5-12), due to which the simulations are further performed with the hexagonal grid.

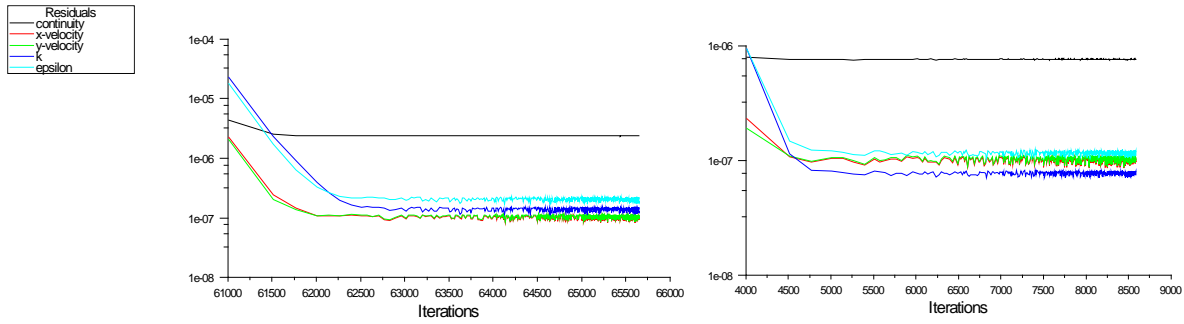


Figure 5-12. Residuals: triangular grid (left) and hexagonal grid (right)

### 5.3.1.3 Validation of the numerical 2D model and selection of the turbulence model

In order to check whether the same conditions were achieved in the experimental system and in the guide vanes of the turbine model, a simulation of 2D water flow through the turbine with empty space behind the cascade was performed, i.e. in the absence of a runner (Figure 5-13). The simulations are made using three different turbulent models:  $k-\epsilon$ ,  $k-\omega$  and  $k-\omega SST$ . The inlet velocity is constant and the outlet is towards the atmosphere. The results obtained by applying different turbulence models are compared with the measured values of pressures at the measuring points of the blade (Figure 5-14). The comparison is made based on the pressure differences between the pressure and suction blade surface. The greatest alignment exists with the  $k-\epsilon$  model thus it is applied in all further simulations because it best describes the flow through the turbine model. The highest discrepancy between the numerical and experimental results is less than 8%, except for the second measuring point which shows larger deviation.

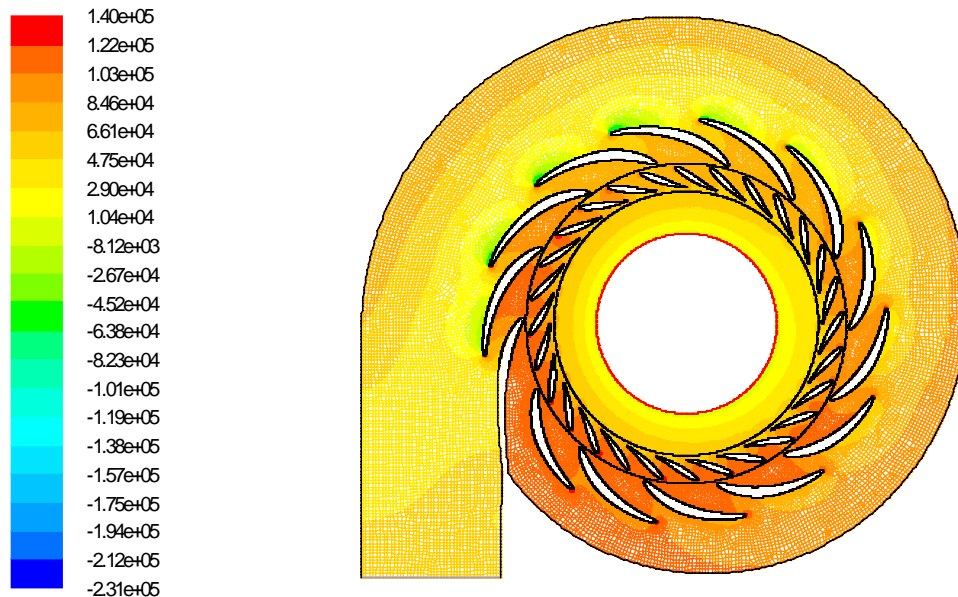


Figure 5-13. Pressure distribution in the flow space – 2D model of turbine without runner

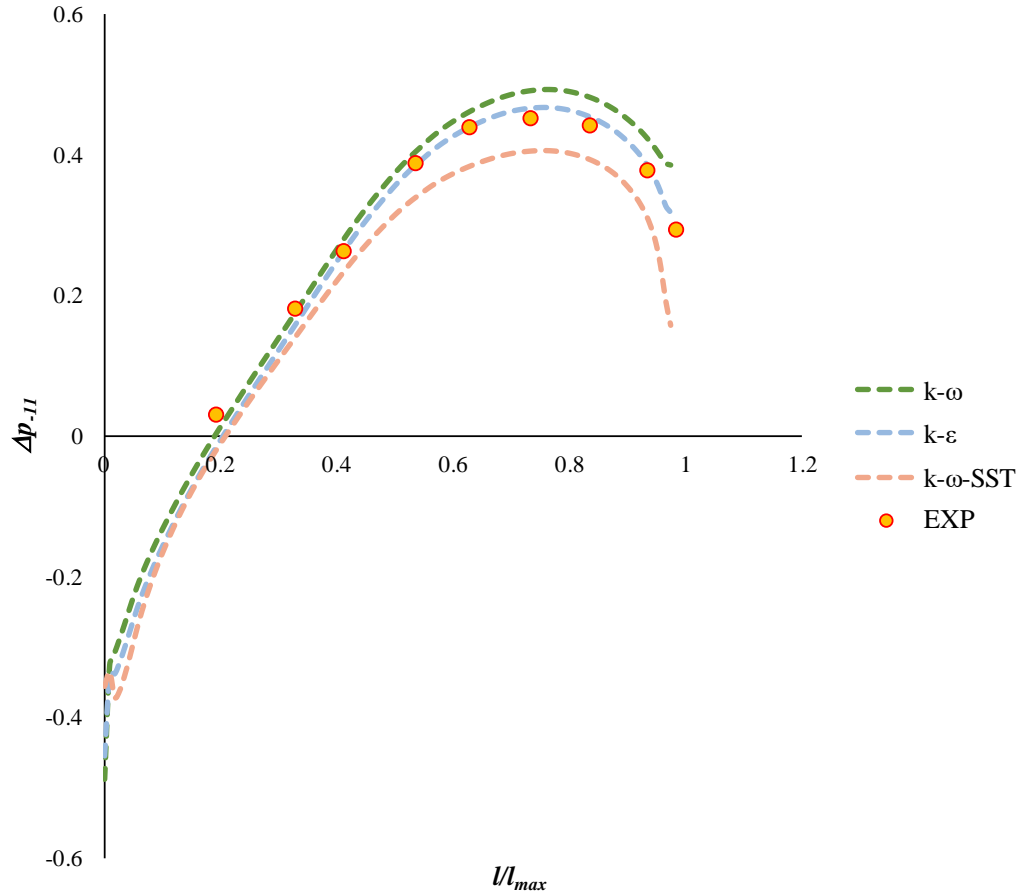


Figure 5-14. Comparison of numerical results by using three turbulent models with experimentally measured pressure values

#### 5.3.1.4 Defining the conditions in the 2D numerical model

According to experimental research conducted on the Francis turbine model in the NTNU Hydropower Laboratory, a maximum efficiency of 93.4% is achieved with a net head of 11.9m, a flow rate of  $0.2\text{m}^3/\text{s}$ , and a runner speed of 333rpm.

The guide vane position in the model of the turbine corresponds to the shock-free entry of water flow, i.e. the turbine operation in the optimal point. Since the two-dimensional model cannot represent the same 3D runner, an analysis was performed based on the numerical results for different inlet velocities (discharge) at a runner speed of 333.33rpm to select the inlet velocity at which maximum system efficiency will be achieved. For different values of the inlet velocities in the spiral casing in the 2D numerical model, the mass flow  $Q_m$  [kg/s], the torque of the runner (rotating cascade)  $M$  [N] and the inlet and outlet total pressures  $p_{11}$  [Pa] and  $p_{12}$  [Pa] are read in order to calculate the efficiency of the system under different inlet conditions:

$$\eta_{sis} = \frac{P_t}{P_h} \quad 5-1$$

where the output power of the system is

$$P_t = M\omega = M \frac{2\pi n}{60} [W] \quad 5-2$$

calculated for a constant angular velocity  $\omega = 34.9$  [rad/s], i.e. a constant number of revolutions  $n = 333.33$  [rpm].

The hydraulic power of the system is calculated according to:

$$P_h = Q\Delta p\eta_{sis} [W] \quad 5-3$$

where  $Q = \frac{Q_m}{\rho}$  [ $m^3/s$ ] is the water volume flow (at its constant density of  $\rho=998$   $kg/m^3$ ), a  $\Delta p = p_{t1} - p_{t2}$  [ $Pa$ ] is the total pressure difference in the system.

The efficiency of the system can be calculated according to the final expression:

$$\eta_{sis} = \frac{M\omega\rho}{Q_m\Delta p} [-]. \quad 5-4$$

From the obtained dependence of the system efficiency on the inlet velocity, shown in Figure 5-15, it is seen that the highest efficiency is achieved for a velocity of 13.6 m/s at the spiral casing inlet.

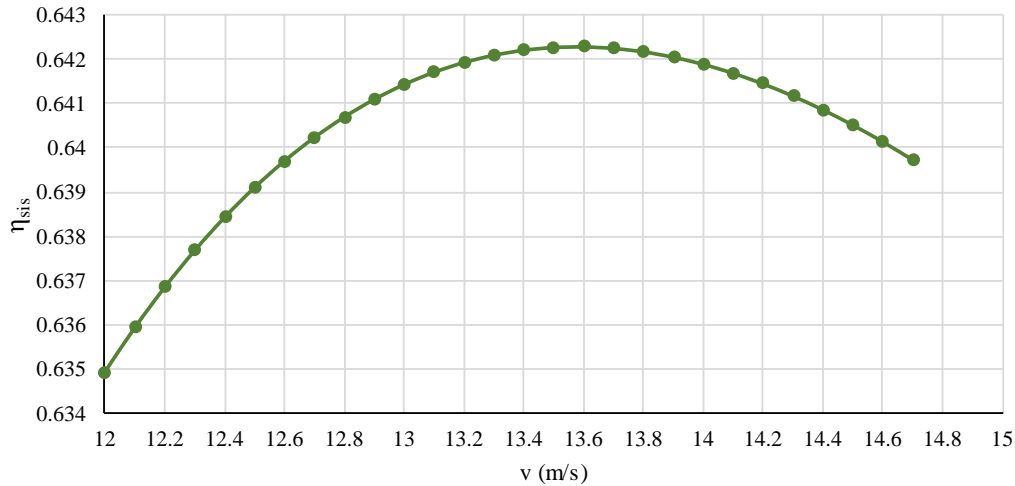


Figure 5-15. Changing of the system performance depending on inlet velocity

## 5.3.2 Influence of inlet conditions on guide vane pressure distribution

### 5.3.2.1 Influence of spiral casing

The loads on guide vanes 7 and 8 are compared for different inlet parameters achieved by using different spiral casings. The NTNU spiral casing and spiral casing calculated by a new methodology suggested in Chapter 7 are used in case without (WR) and with runner behind the guide vanes.

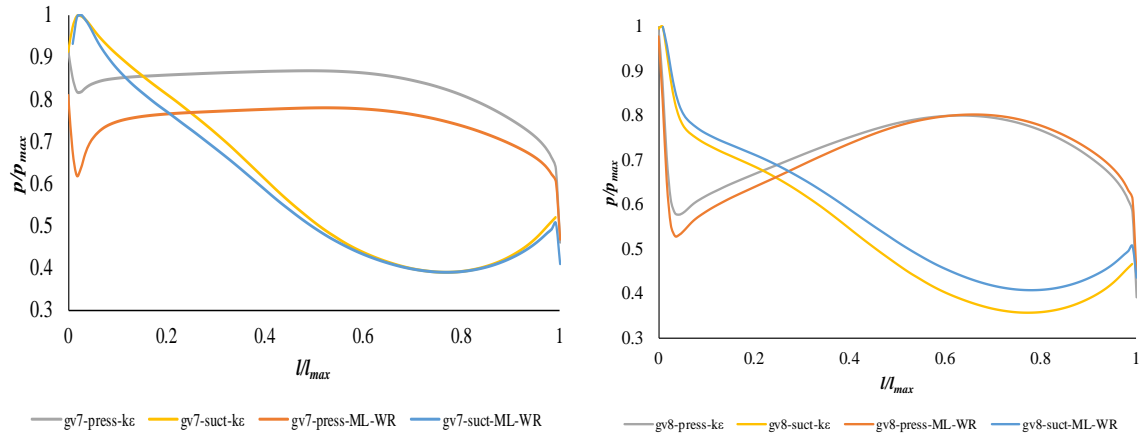


Figure 5-16. Guide vane pressure distribution – comparison when using different inlet conditions

From Figure 5-16 it can be noted that the new spiral casing design offers smaller guide vane loads since the pressure difference is lower when no runner is presented.

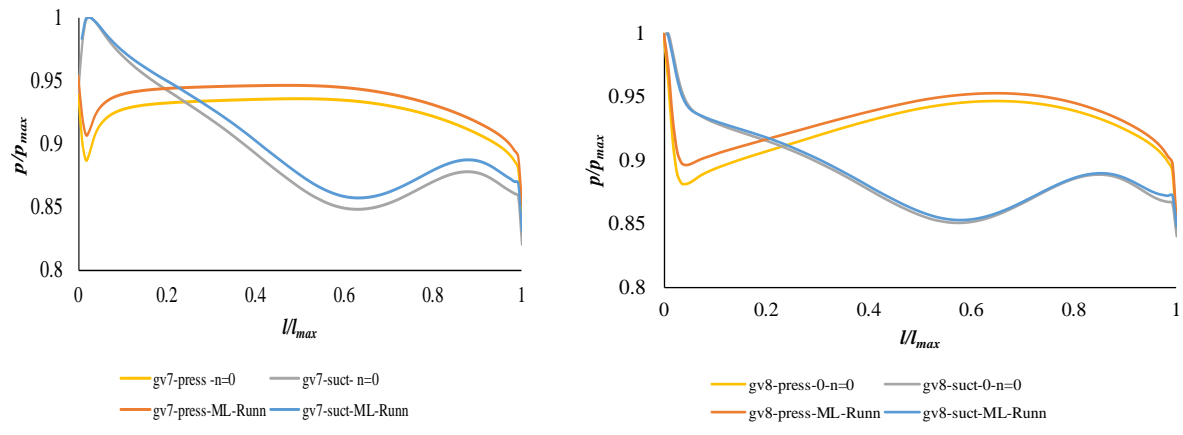


Figure 5-17. Guide vane pressure distribution – comparison when using different inlet conditions, with a runner

From Figure 5-17 it can be noted that almost same loads are exerted on the guide vane surface in the presence of a runner when using different spiral casings. However, further analysis should be done to make a firm conclusion even though it is shown that the spiral casing design is an influential parameter.

Moreover, a comparison of the velocity distribution at guide vanes inlet circumference when using different spiral casing and no runner is made (Figure 5-18).

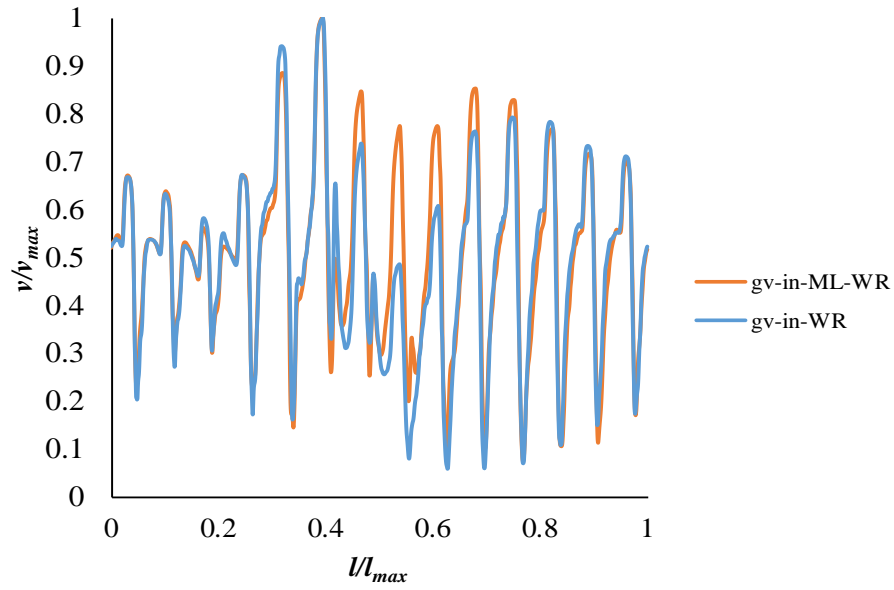


Figure 5-18. Guide vane inlet velocity distribution for different spiral casings used

The comparison shows that more uniform flow is achieved in one zone in front of the guide vanes by using the new spiral casing design.

### 5.3.2.2 Influence of stay vanes

Guide vane loads also depend on their position in relation to the stay vanes which can be seen from the next graph where two neighbouring guide vanes have different pressure distribution (Figure 5-19).

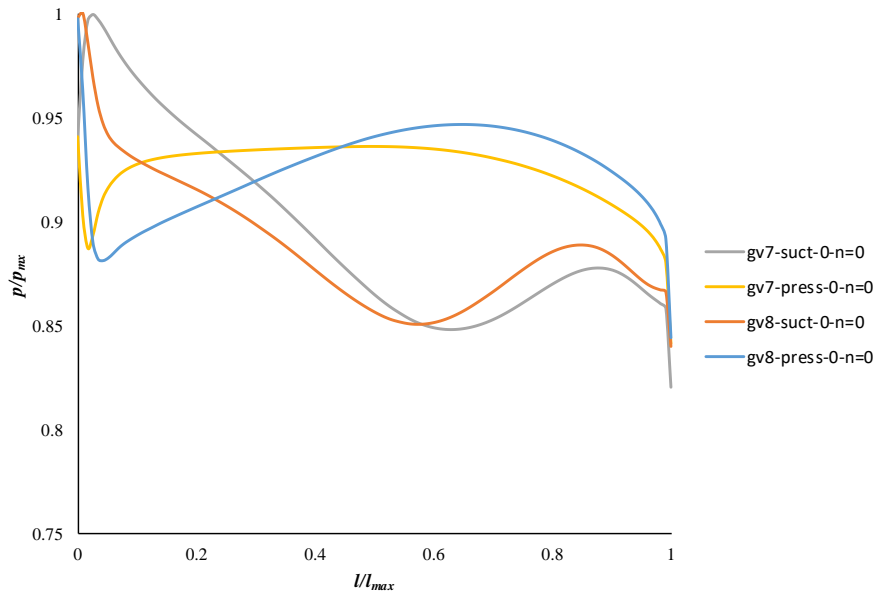


Figure 5-19. Pressure distribution of guide vanes with different position in relation to the stay vanes

### 5.3.3 Analysis of the runner blade position and variable speed influence on guide vane pressure distribution – quasi-steady conditions

After choosing the initial boundary conditions – constant inlet velocity of 13.6 m/s and atmospheric pressure at the outlet, and turbulence model –  $k-\varepsilon$ , simulations are performed for steady 2D water flow through the turbine in case of a static runner and a rotating runner at 5 different speeds. Numerical simulations are performed for several runner blade positions in relation to the guide vane to determine its influence on the pressure distribution.

Results are compared for the following runner speeds:  $\omega=0$ ,  $\omega =27.9$  rad/s,  $\omega =31.4$  rad/s,  $\omega =34.9$  rad/s,  $\omega =38.4$  rad/s, and  $\omega =41.9$  rad/s, i.e.  $\pm 20\%$  and  $\pm 10\%$  in relation to the nominal runner speed  $\omega =34.9$  rad/s.

#### 5.3.3.1 Analysis of the runner blade position relative to the guide vane

The runner blade passing from position  $\alpha=0^\circ$  when it is in line with the guide vane to position in line with the next guide vane. This passage is divided into 5 equal parts of  $2.572^\circ$  (Figure 5-20).

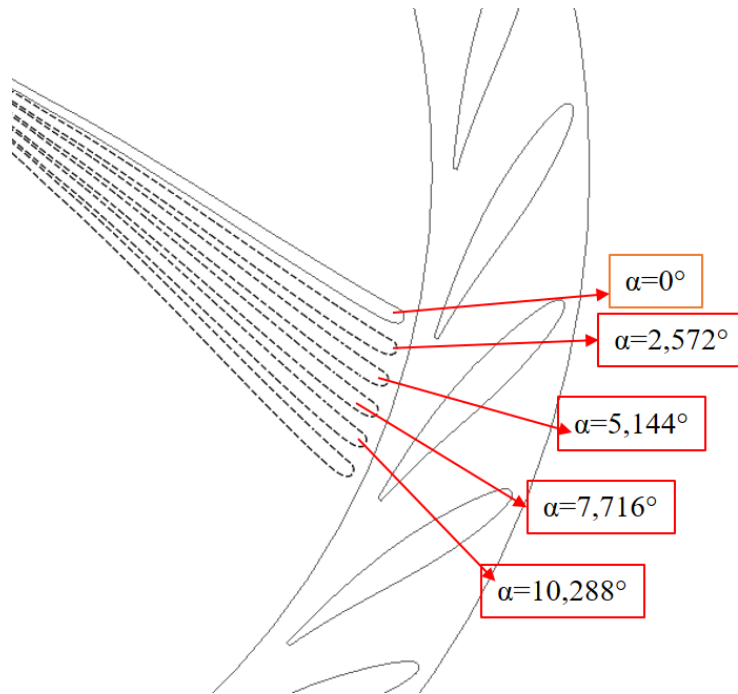


Figure 5-20. Runner blade position relative to the guide vane in quasi-steady state

For all positions, the pressure distribution on the guide vane pressure side is almost the same for different runner speeds. However, the suction side which is more affected from the runner rotation has different pressure distribution at different positions. For the first position ( $0^\circ$ ), the difference in the guide vane pressure distribution on the suction side starts from 0.6 of the guide vane length when the pressure starts to decrease with runner speed. For the second position ( $2.572^\circ$ ), there are two crossing points, at around 0.5 and 0.9 of the guide vane length where the pressure changes, i.e. it increases with runner speed increment (Figure 5-21).

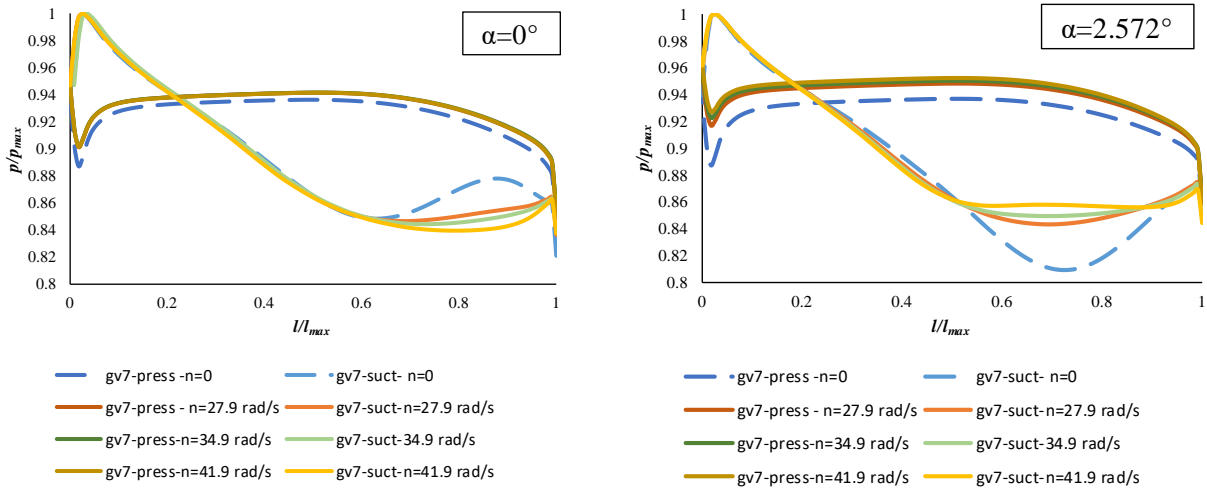


Figure 5-21. Runner speed influence on guide vane pressure distribution at positions  $0^\circ$  and  $2.572^\circ$

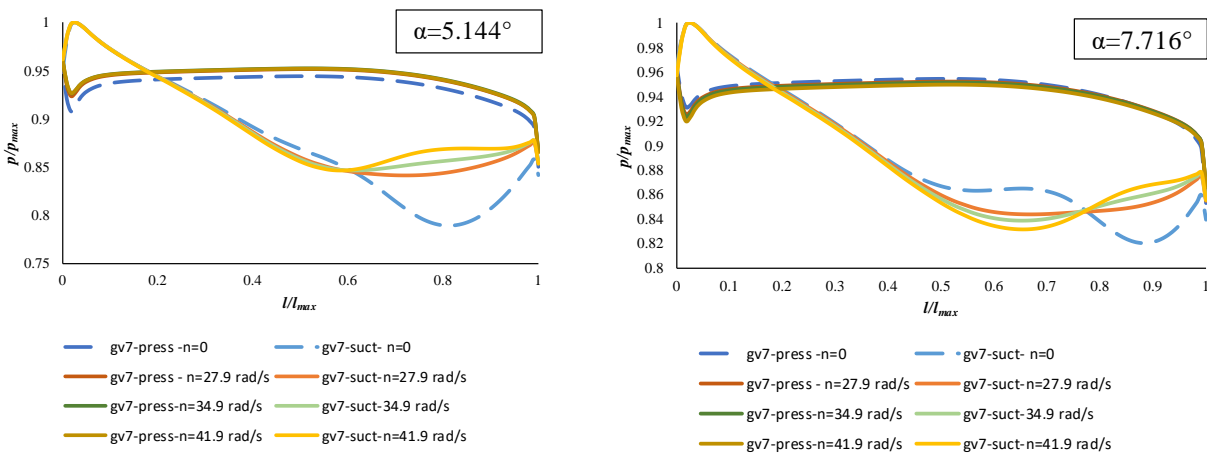


Figure 5-22. Runner speed influence on guide vane pressure distribution at positions  $5.144^\circ$  and  $7.716^\circ$

For position  $5.144^\circ$ , there is one crossing point at 0.6 of the guide vane length where the pressure starts changing with the runner speed as in the previous position. For position  $7.716^\circ$ , there are two crossing points, at 0,4 and 0,8 of the guide vane length in between which pressure decreases with runner speed, and afterwards it starts increasing with runner speed. For the last position  $10.288^\circ$ , pressure decrement with runner speed starts at 0.4 of the guide vane length (Figure 5-22, Figure 5-23).

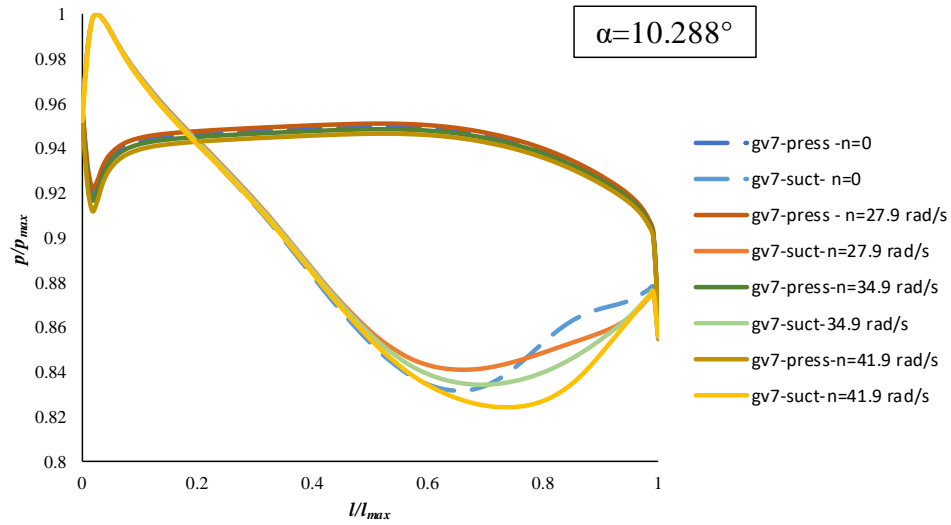


Figure 5-23. Runner speed influence on guide vane pressure distribution at position 10.288°

The analysis is done for different runner blade positions at constant runner speed (Figure 5-24).

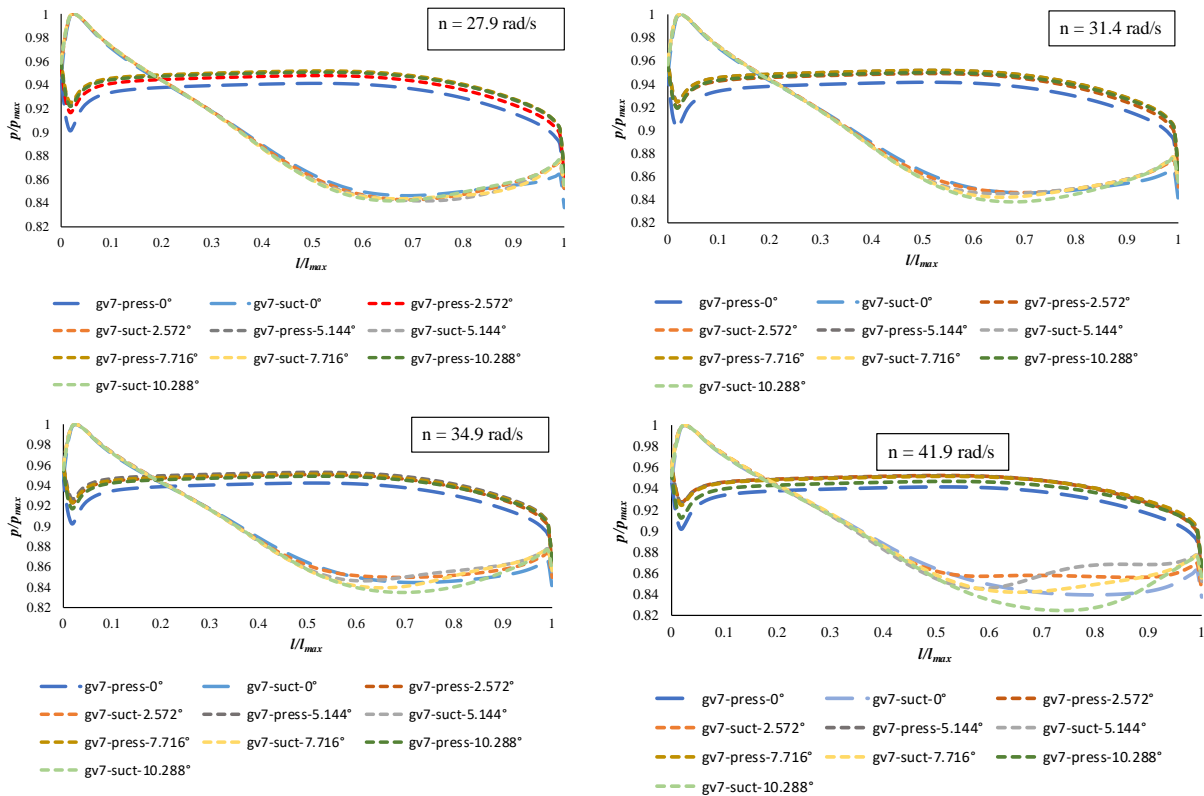


Figure 5-24. Guide vane pressure distribution at different positions for constant runner speed

It can be seen that the pressure distribution form is deforming more for higher runner speeds, especially on the guide vane suction side, on the half closer to the trailing edge.

## 5.4 Numerical modelling of unsteady flow through guide vanes at different runner speeds

The numerical simulations are performed for the different runner speeds with a total pressure at the inlet which corresponds to the same discharge, i.e. inlet velocity of 13.6 m/s and atmospheric pressure at the outlet. The time step for each runner speed is selected to correspond to 1° runner rotation.

The measuring points from the experimental investigation are used as monitoring points to obtain the values of pressure over time. In addition, the guide vane torque change is being monitored. This allows collecting data on the pressure and torque pulsations.

### 5.4.1 Inlet conditions – guide vane inlet and outlet velocity variation

The pulsations of velocity at guide vane inlet and outlet are first considered in the analysis. The root mean square (RMS) for guide vane inlet and outlet velocity at different runner speed is shown in Figure 5-25.

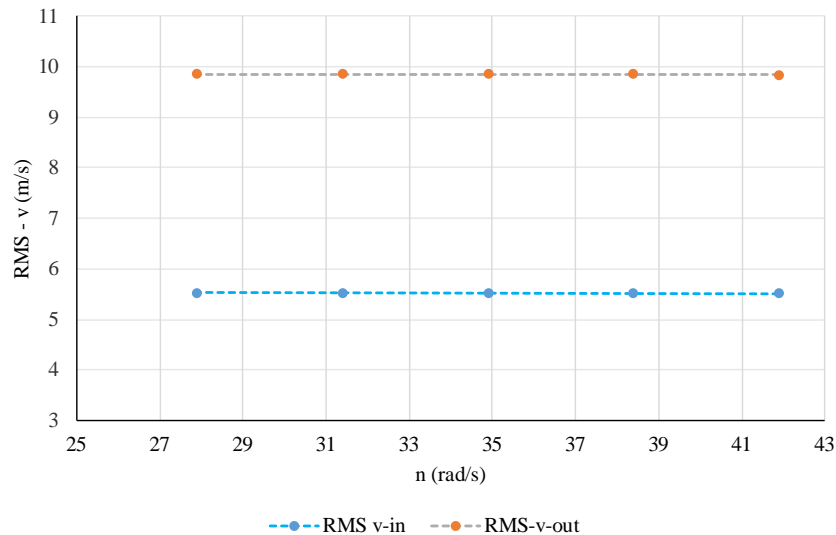


Figure 5-25. Guide vane inlet and outlet velocity – RMS value for different runner speed

The RMS value negligibly varies with the runner speed thus it can be stated that the water discharge remains constant.

The peak-to-peak (PtP) values relative to the RMS values of guide vane inlet and outlet velocity as shown in Table 6 change with the runner speed in small limits, i.e. 0.037-0.0465% for guide vane inlet velocity and 0.08-0.116% for guide vane outlet velocity.

Table 6. Peak-to-peak values of guide vane inlet and outlet velocity

$n$	PtP/RMS-v-in	PtP/RMS-v-out
$\omega$ (rad/s)	(%)	(%)
41.9	0.041128609	0.079918785
38.4	0.039678068	0.081028271
34.9	0.037357276	0.093128486

31.4	0.036904217	0.107526782
27.9	0.046520768	0.116066431

In conclusion, according to the numerical results, the velocity can be taken as a constant parameter.

The velocity amplitude changes with the runner speed – the amplitude decrement, frequency increment, and period decrement with increasing the runner speed is observed in Figure 5-26.

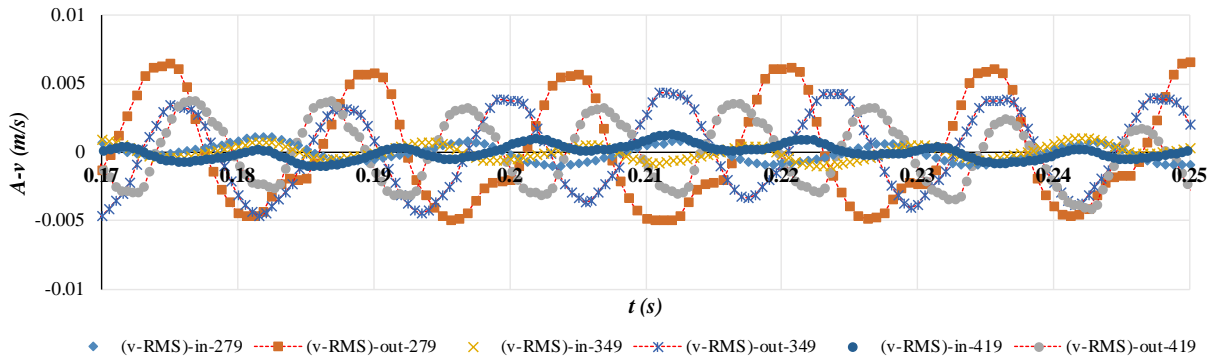


Figure 5-26. Guide vane inlet and outlet velocity variation during time

#### 5.4.2 Guide vane torque pulsations

The RMS value of the guide vane torque shows  $\pm 0.3$  Nm variation compared to the torque at the nominal runner speed thus it can be stated that it is constant (Figure 5-27 left). However, the PtP value of torque is changing in the interval 8.6-15% with the runner speed (Figure 5-27 right).

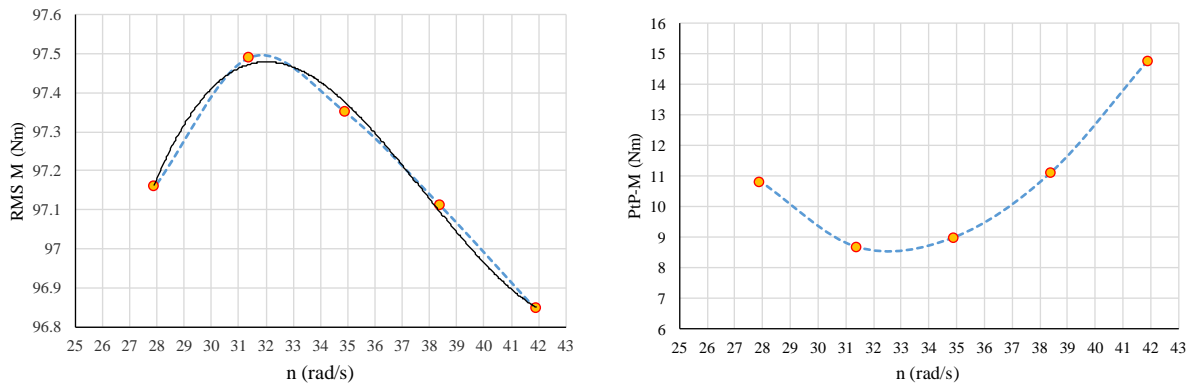


Figure 5-27. RMS and PtP values of torque at different runner speeds

It can be concluded that the guide vane torque pulsations should not be neglected due to the difference compared to the RMS value and their change with the runner speed. According to this, parametrisation of torque variations in time would help in predicting these pulsations for certain input parameters.

In order to parametrise the torque variation during time, a complete Fourier series with sines and cosines is used:

$$M(t) = A_1 \sin(\omega t) + B_1 \cos(\omega t) + A_2 \sin(2\omega t) + B_2 \cos(2\omega t) \quad 5-5$$

but reduced to:

$$M(t) = B_1 \cos(\omega t) + A_2 \sin(2\omega t) \quad 5-6$$

where coefficients  $B_1$  and  $A_2$  are calculated by integration [61]:

$$B_1 = \frac{1}{\pi} \int_0^{2\pi} M(t) \cos(\omega t) dt \quad 5-7$$

$$A_2 = \frac{1}{\pi} \int_0^{2\pi} M(t) \sin(2\omega t) dt \quad 5-8$$

For each runner speed, the coefficients are calculated using the numerical data (Figure 5-28).

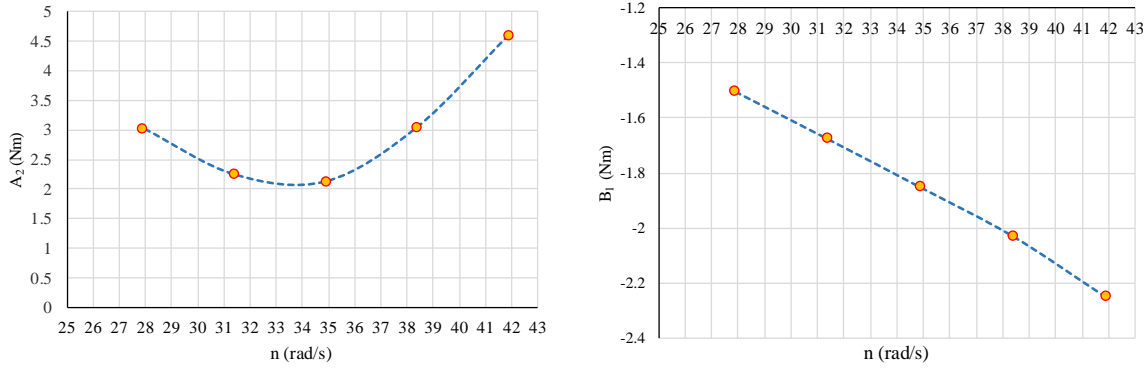


Figure 5-28.  $A_2$  and  $B_1$  coefficients' variation with runner speed

Strouhal number is defined by:

$$S_h = \frac{L}{u \cdot \frac{1}{T_t}} \quad 5-9$$

including:

- characteristic length  $L$  such as the guide vane length;
- the peripheral velocity calculated as:  $u = R_1 \cdot \omega$  [m/s] - where  $R_1$  is the runner inlet,  $\omega$  [rad/s] is the runner angular velocity.
- The theoretical period calculated as:  $T_t = \frac{2\pi}{z \cdot \omega}$  [s] where  $z$  is the number of runner blades.

The following relations are then established:

$$\frac{1}{\sqrt{A_2} n^{4,5}} = k_1 S_h \quad 5-10$$

$$\frac{B_1}{n^3} = k_2 S_h \quad 5-11$$

from where the coefficients  $A_2$  and  $B_1$  can be evaluated by using the linear equations (coefficients  $k_1$  and  $k_2$ , respectively) for the known Strouhal number, as given in Figure 5-29.

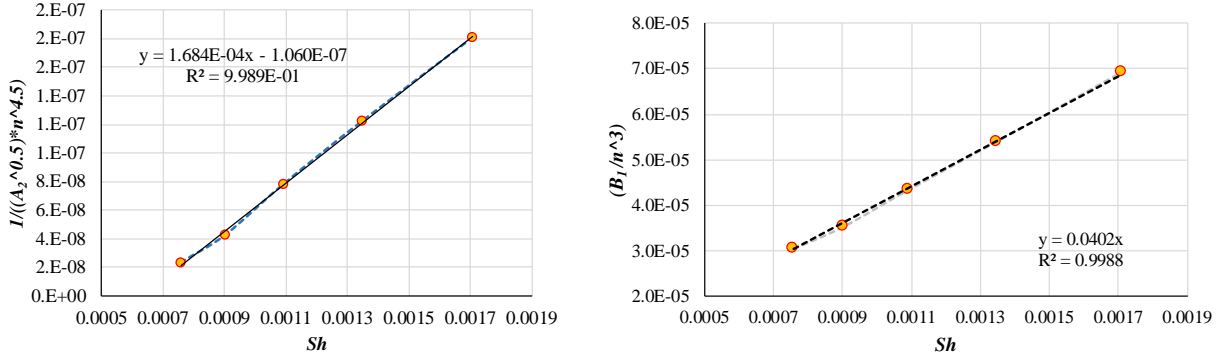


Figure 5-29. Calculating the coefficients  $A_2$  and  $B_1$  for a given Strouhal number

Linearization of the frequency of the numerical model, calculated as reciprocal value of the period, i.e.  $f_m = \frac{1}{T_m}$  [Hz], is established by the expression:

$$\frac{\left(\frac{v_{out}}{u}\right)^2}{\sqrt{S_h}} = f \left(\frac{f_m}{f_t}\right) \quad 5-12$$

where  $v_{out}$  [m/s] is the RMS value of guide vane outlet velocity and  $f_t$  [Hz] is the theoretical frequency.

The dependency is given in Figure 5-30.

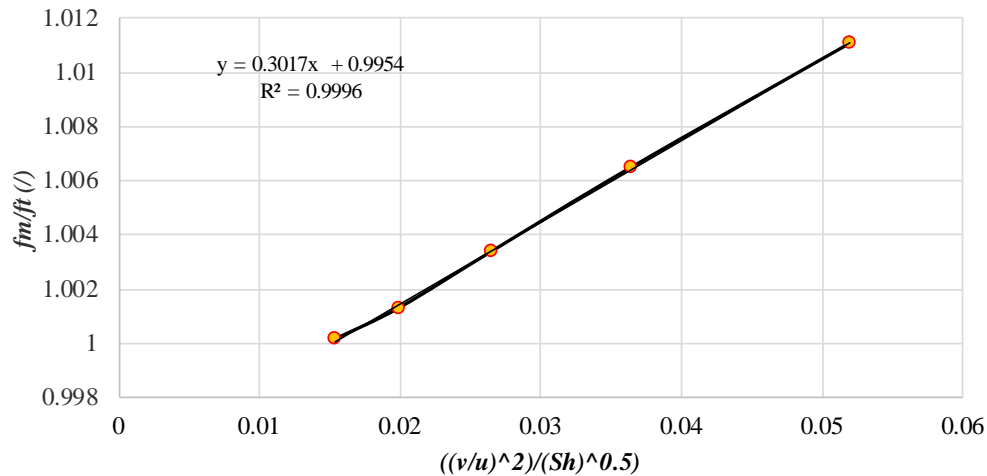


Figure 5-30. Relation between the theoretical and numerical model frequency

The calculation is confirmed by confirming alignment between torque variation in time obtained only from the numerical data and obtained both numerically and theoretically, as given in Figure 5-31 and Figure 5-32.

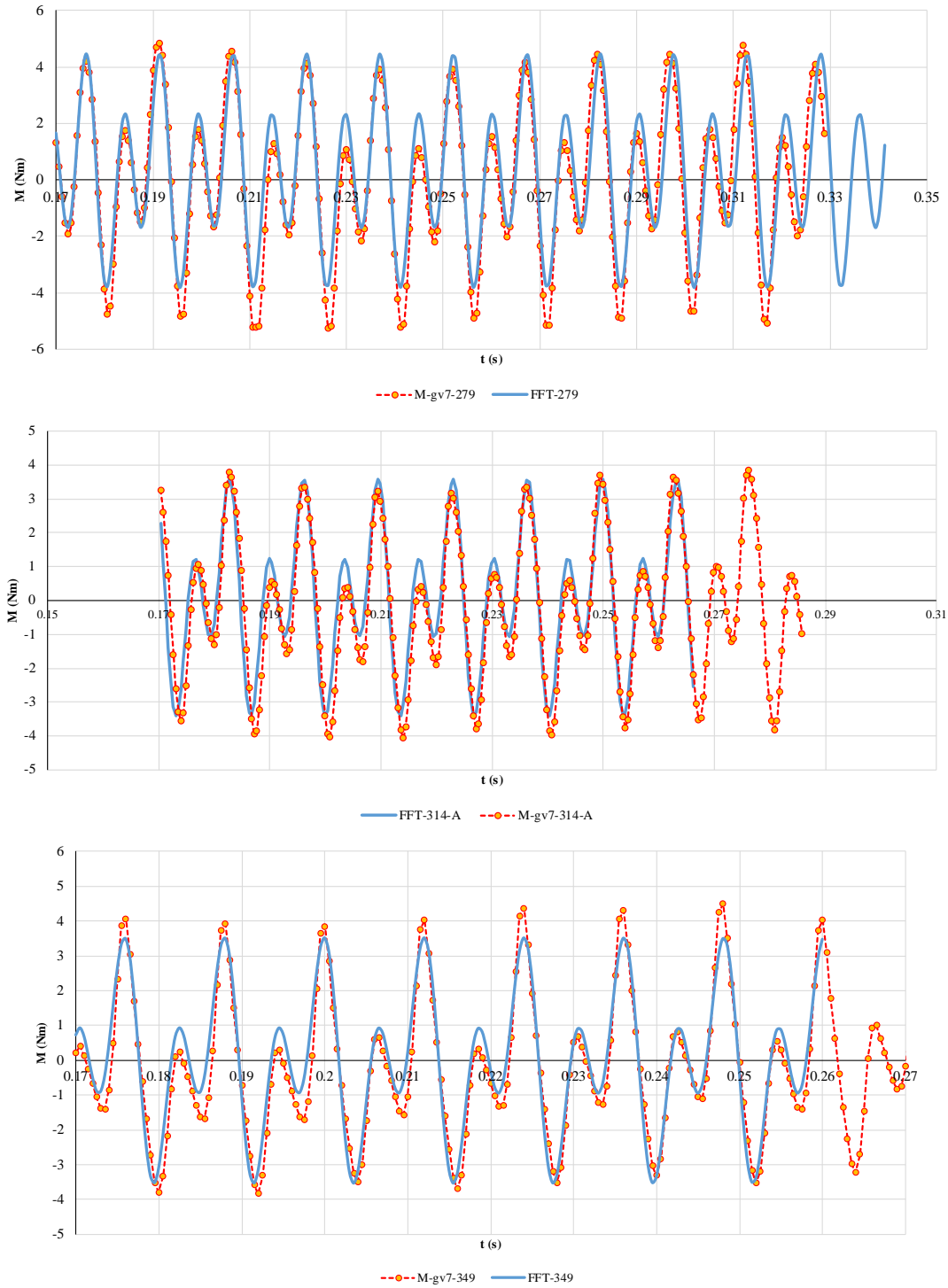


Figure 5-31. Guide vane torque pulsation – comparison of numerical data and calculation for  $\omega=27,9 \text{ rad/s}$ ,  $\omega=31,4 \text{ rad/s}$  and  $\omega=34,9 \text{ rad/s}$

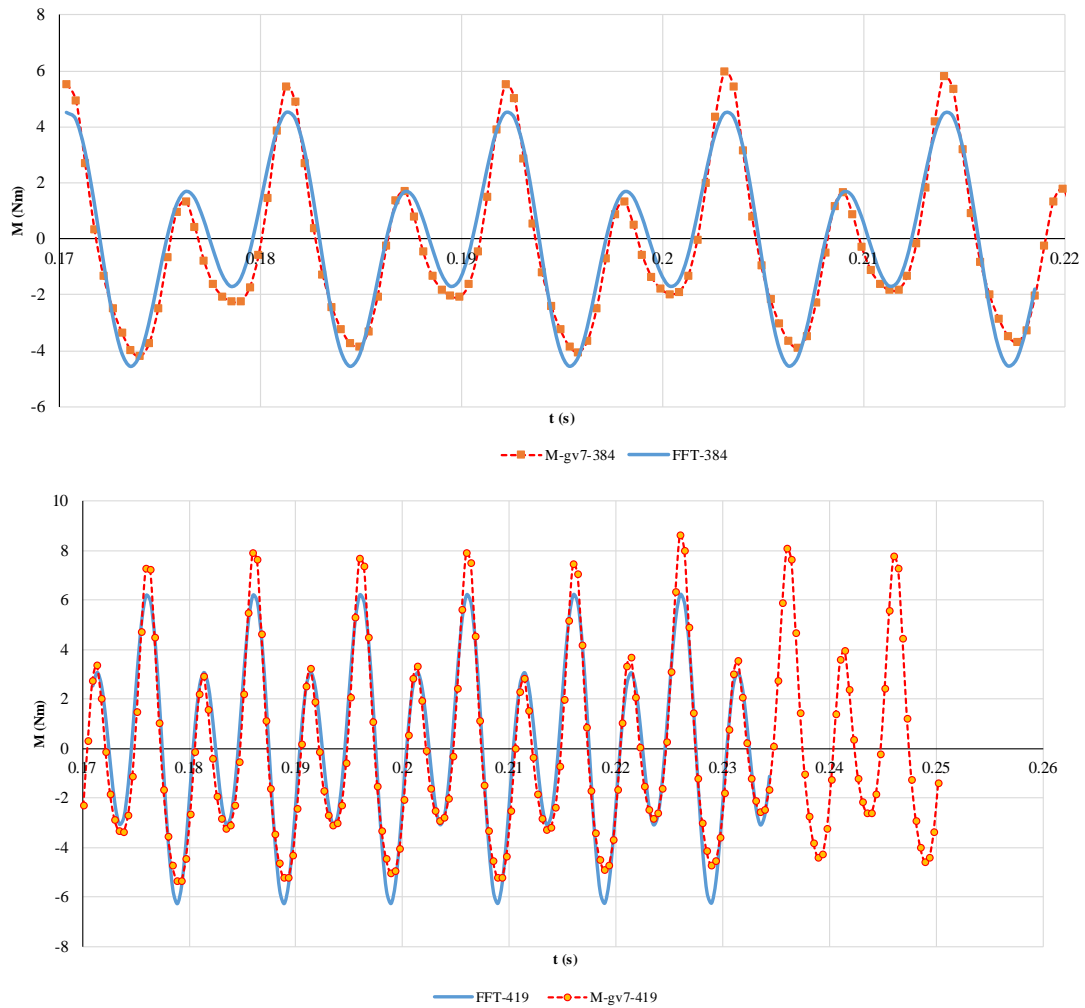


Figure 5-32. Guide vane torque pulsation – comparison of numerical data and calculation  $\omega=38,4$  rad/s and  $\omega=41,9$  rad/s

The guide vane pressure distribution changes over time and, for same torque values, same or different pressure profile can be obtained. The analysis is given for different runner speeds – nominal and  $\pm 20\%$ .

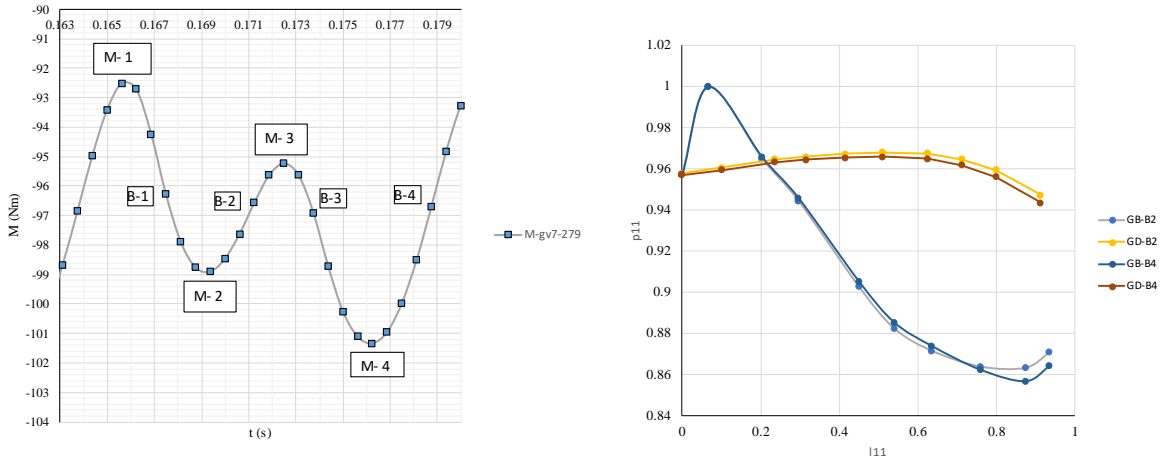


Figure 5-33. Torque of same values at 2 different time moments for runner speed  $\omega=27.9$  rad/s and corresponding pressure distribution comparison

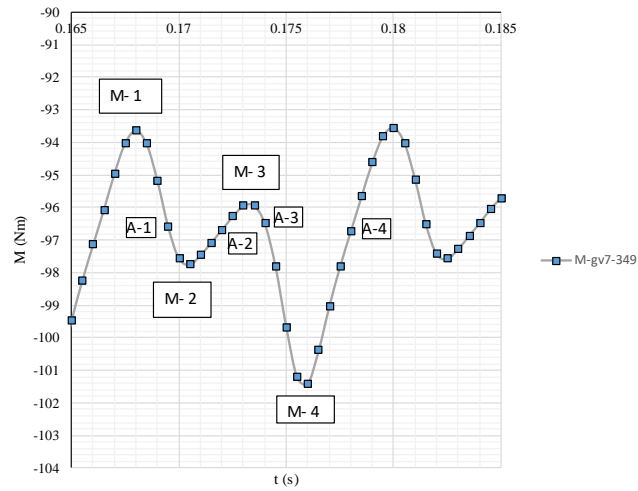


Figure 5-34. Torque of same values at 2 different time moments for runner speed  $\omega=34.9$  rad/s

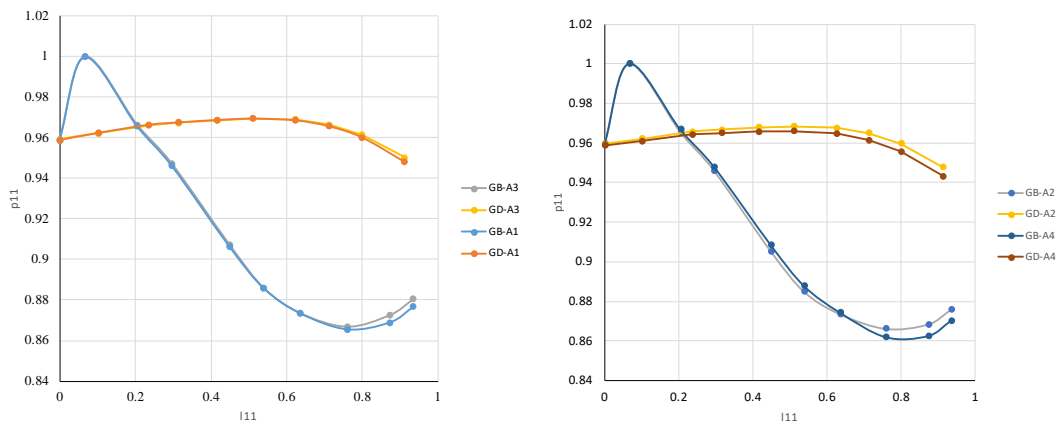


Figure 5-35. Comparison of pressure distribution for same guide vane torque at different time moment at runner speed  $\omega=34.9$  rad/s

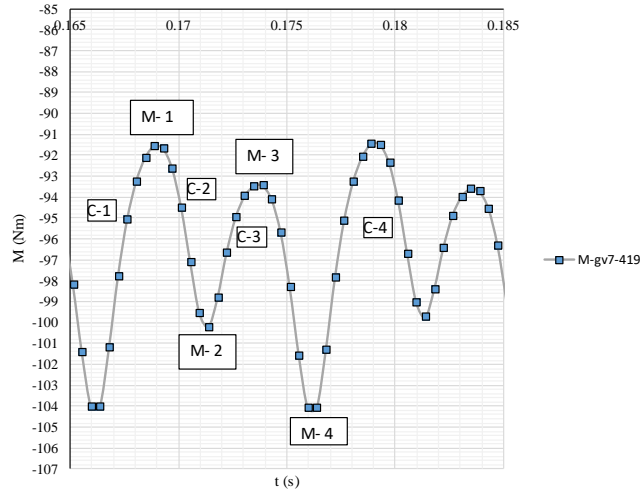


Figure 5-36. Torque of same values at 2 different time moments for runner speed  $\omega=41.9$  rad/s

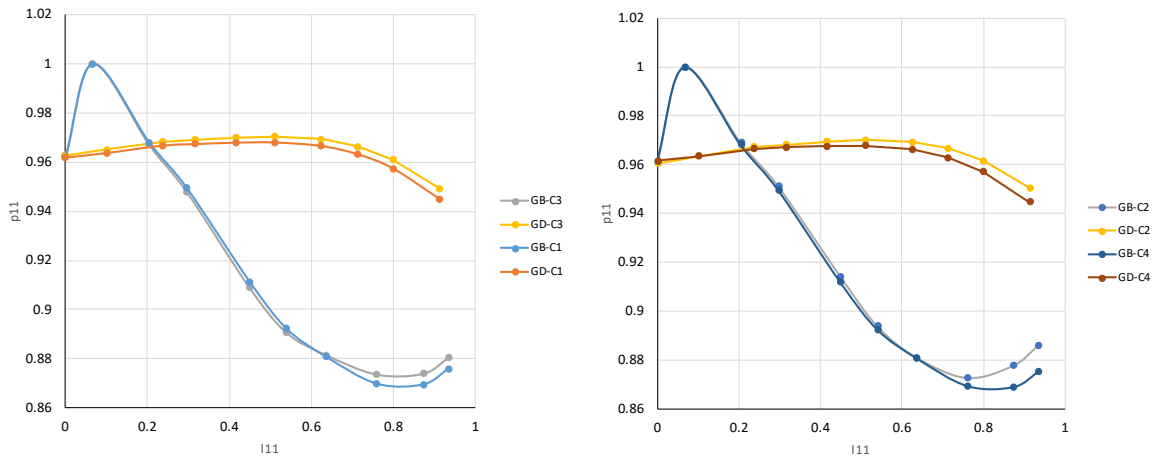


Figure 5-37. Comparison of pressure distribution for same guide vane torque at different time moment at runner speed  $\omega=41.9$  rad/s

Figure 5-33, Figure 5-34, Figure 5-35, Figure 5-36 and Figure 5-37 show that same values of guide vane torque can be achieved at different time moments, but the guide vane pressure distribution may not be the same. This can be attributed to a possible difference in the location of the acting point (line) of the resultant hydrodynamic force.

### 5.4.3 Guide vane pressure pulsations

Pressure change during time in the first (front) measuring point located on the leading edge (p1) and the last measuring points closest to the trailing edge on the pressure surface (GD p10) and suction surface (GB p10) for runner speed of 27,9 rad/s and 41,9 rad/s is presented in Figure 5-38 and Figure 5-39.

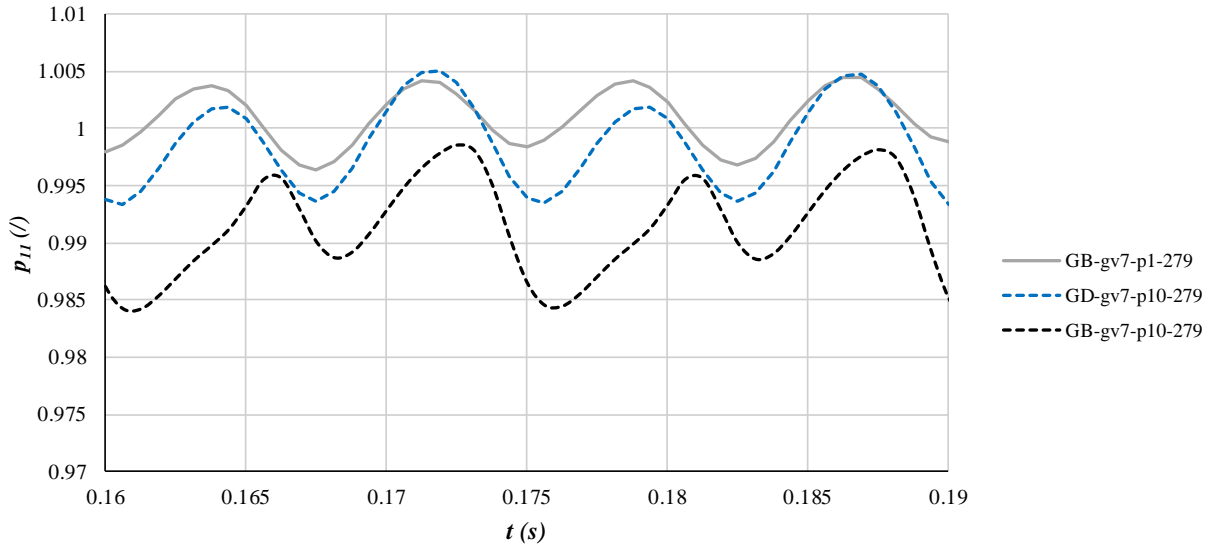


Figure 5-38. Pressure variation during time for runner speed of 27,9 rad/s

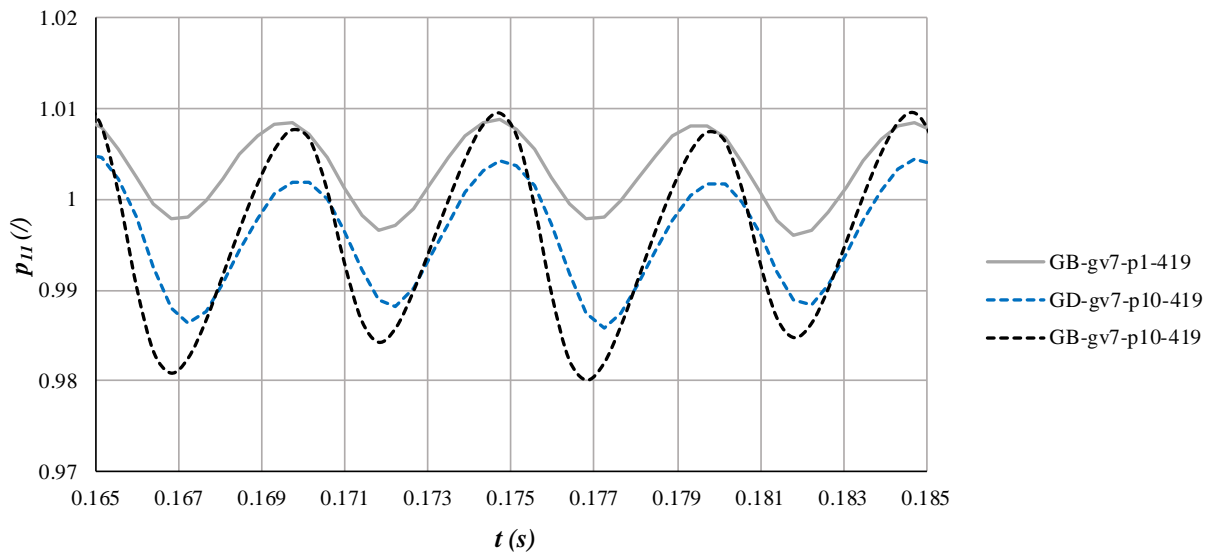


Figure 5-39. Pressure variation during time for runner speed of 41,9 rad/s

Pressure pulsations are lower for the leading edge measuring point for both considered cases of runner speed, because of the higher distance of the guide vane leading edge from the runner. Larger pulsations are obtained at higher runner speed.

Larger pressure pulsations are obtained on the guide vane suction side which is more affected by the runner rotation since the distance between them is higher.

Pressure pulsations in the last measuring point on the pressure and suction side, respectively, at  $\pm 20\%$  of the nominal speed are shown in Figure 5-40.

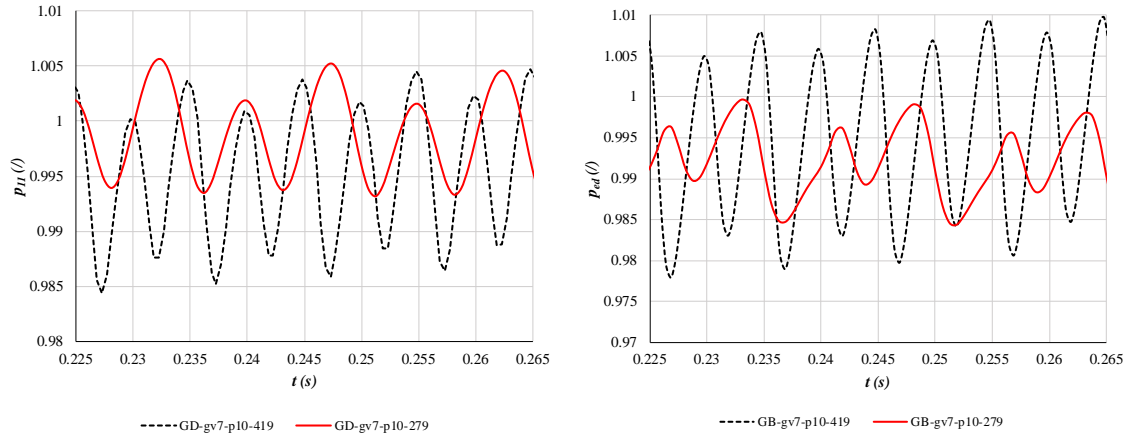


Figure 5-40. Pressure pulsations in measuring point 10 on pressure (left) and suction side (right)

The amplitude and the frequency are higher with higher speed.

For the front measuring point, guide vane pressure pulsations are shown in Figure 5-41 which also have higher amplitude and frequency at higher runner speed.

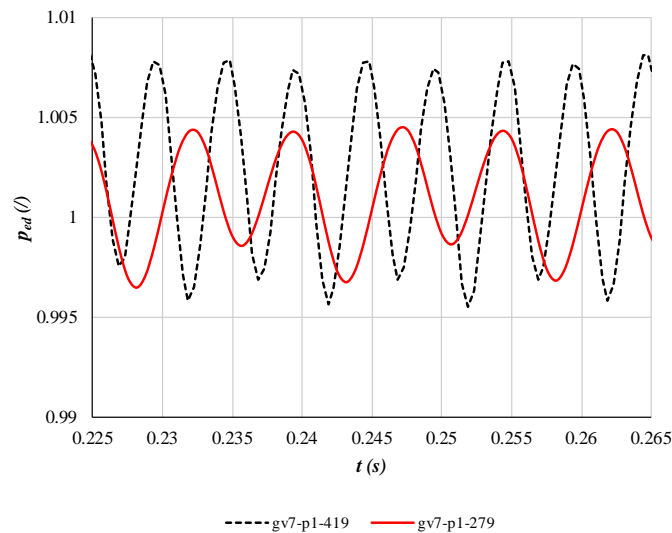


Figure 5-41. Pressure pulsations in the frontal measuring point (point 1)

Figure 5-42 shows I percentage the PtP values relative to RMS value of pressure in 10 measuring points on the guide vane pressure and suction side, respectively, at  $\pm 20\%$  of the nominal speed.

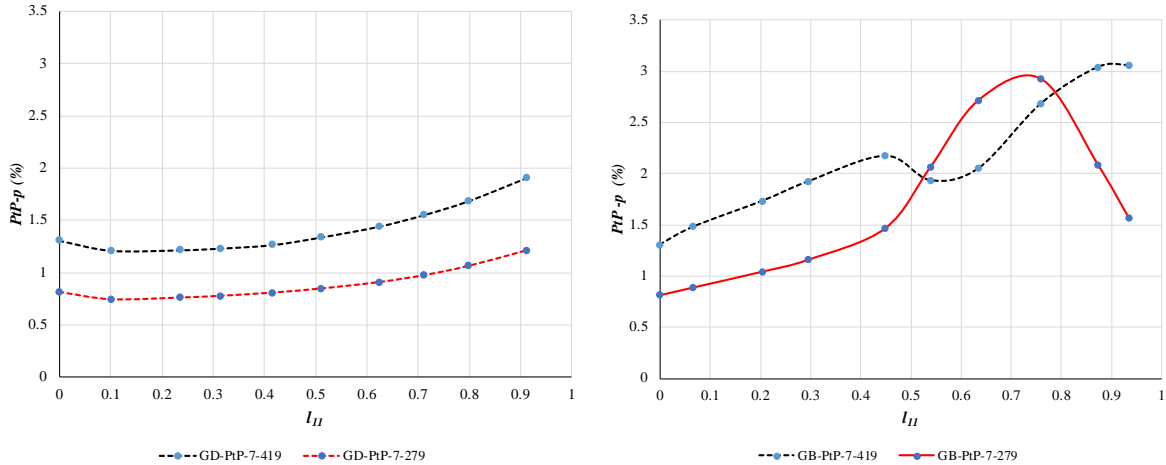


Figure 5-42. *PtP* values relative to RMS value of pressure in the measuring points along the guide vane pressure (left) and suction (right) side

Larger pressure changes on guide vane pressure side are noted at higher runner speed, dominant in the second half of the guide vane length. Pressure changes are increasing along the guide vane pressure side, while up until 45% of the guide vane length, pressure pulsations on the suction side are increasing along the guide vane length and are larger for higher runner speed.

For higher runner speed, there is a local decrease of pressure pulsations from 45% to 70% of guide vane suction side length, then continuous increase till the trailing edge. For lower runner speed, there is a local increase of pressure pulsations from 45% to 75% of the guide vane length, then the pulsations are getting smaller

#### 5.4.4 Guide vane strength conditions

The load forces  $F_{y11}$  along the guide vane length for the cases of fluid flow analysed in Chapter 4 and Chapter 5 are given in Figure 5-43. Comparison of loads is performed for the next cases:

- Solitary aerofoil
- Aerofoil set in a cascade with higher relative pitch
- Aerofoil set in a cascade with lower relative pitch
- Guide vane - without runner
- Guide vane - without runner, with newly designed spiral casing
- Guide vane – with non-rotating runner
- Guide vane with runner rotating at nominal runner speed
- Guide vane with rotating runner and newly designed spiral casing

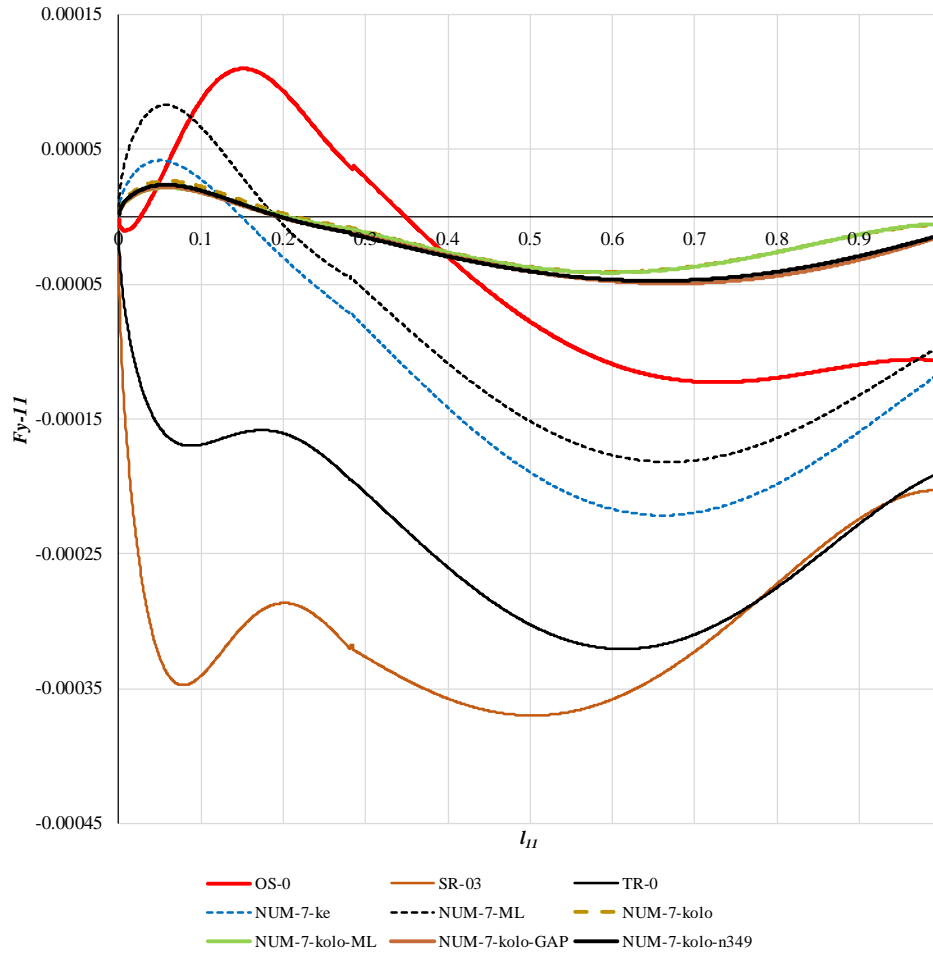


Figure 5-43. *Јакостна состојба на лопатка во различни услови на опструјување*

The summarizing graph shows loads decrease by reducing the cascade pitch. The loads additionally decrease by setting a non-rotating runner behind the guide vanes. Using the newly designed spiral casing contributes for further loads decrease.

## 6 Guide vane strength analysis

### 6.1 Interaction between a fluid and a solid

In the guide vane cascades in hydraulic turbines, the phenomenon of interaction between the fluid - water and the solid surface (FSI) of the blade occurs. This phenomenon can be mathematically described by the equation of motion of a solid body:

$$m_s \ddot{x} + d_s \dot{x} + k_s x = F(t) \quad 6-1$$

where  $m_s$  is the mass of the body,  $d_s$  is the damping,  $k_s$  is the stiffness of the body,  $F$  is the force acting on the solid body and  $x$  is the displacement, and with the fluid flow equation:

$$\rho \left( \frac{\partial v}{\partial t} + v \cdot \Delta v \right) = -\nabla p + \nabla \cdot T + f \quad 6-2$$

where  $\rho$  is the density of the fluid,  $v$  is the velocity vector,  $p$  is the pressure,  $T$  is the tensor and  $f$  is the mass (volume) force acting on the fluid [6]. The equation for mass conservation is:

$$\frac{\partial \rho}{\partial t} + \nabla \cdot (\rho v) = 0 \quad 6-3$$

For an incompressible fluid, the Navier-Stokes equations can be written as follows:

$$\rho \left( \frac{\partial v}{\partial t} + v \cdot \Delta v \right) = -\nabla p + \mu \nabla^2 v + f \quad 6-4$$

where  $\partial v / \partial t$  indicates unsteadiness,  $-\nabla p$  is a pressure gradient, and  $\mu$  is a dynamic viscosity. The mass conservation equation can be reduced to:

$$\nabla \cdot v = 0 \quad 6-5$$

Understanding the occurrence of interaction between the water and the guide vane requires knowledge of the static loads of the blade under different operating conditions, i.e. at different openings of the guide vane system [30], [62], [63].

### 6.2 Influence of the axis of rotation on the guide vane torque and static loads

Hydraulic turbines often operate outside the optimum point to meet current energy demand. Thus, the static loads on the guide vanes vary with changing operating conditions. The structural performance of Francis turbine guide vanes depends on the intensity of the hydrodynamic forces and the location of the axis of rotation.

These two parameters affect the magnitude and direction of the hydraulic torque on the blade. The optimal position of the axis of rotation of the blade can be determined based on the criteria of achieving the least possible stresses and deformations.

#### 6.2.1 Three-dimensional numerical model of flow through guide vanes

To determine the influence of the axis of rotation on the hydraulic moment at different operating conditions of the turbine and to select its appropriate position, a numerical analysis of

the Francis-99 turbine model was performed, maintaining the geometry of the spiral casing, stay vanes, runner, and diffuser, but replacing the conductive blades with the blade shape for which the experimental and numerical studies in this dissertation were performed. The three-dimensional numerical model is shown in Figure 6-1.

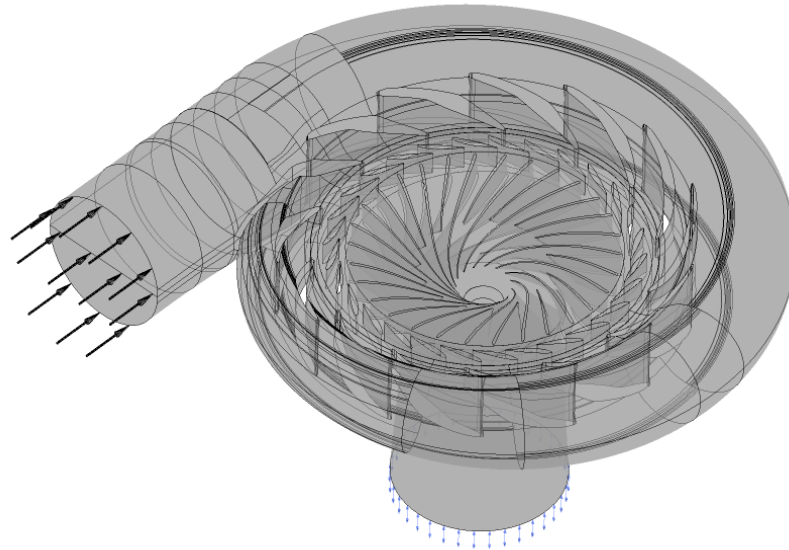


*Figure 6-1. 3D numerical model of a turbine*

Total inlet pressure and outlet pressure are used as boundary conditions. Spatial stationary flow is considered, using the Frozen Rotor approach to take runner rotation into account. The simulations are performed at the same runner speed  $n = 333.33 \text{ min}^{-1}$ . The results obtained from 6 different openings of the guide vanes are analysed, starting from the closed position (Figure 6-2, left) to its maximum opening (Figure 6-2, right). The subject of analysis is blade No. 1 through which the vertical axis shown in Figure 6-2 passes.

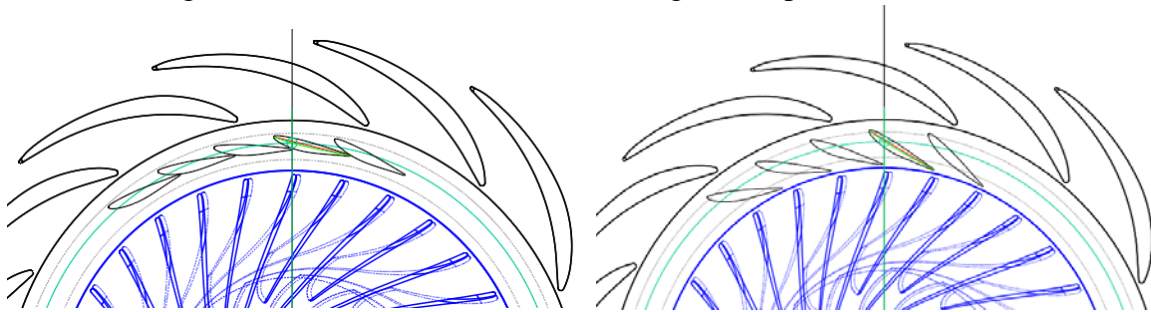


*Figure 6-2. Closed position (left) and maximum opening of the guide vanes (right)*

### **6.3 Influence of the guide vane axis of rotation on the torque**

Nine (9) positions of the axis of rotation of the guide vane were analysed, all chosen to lie on the camber line of the hydrofoil (Figure 6-3), starting from the initial point P0 to 25% of the length of the chord.

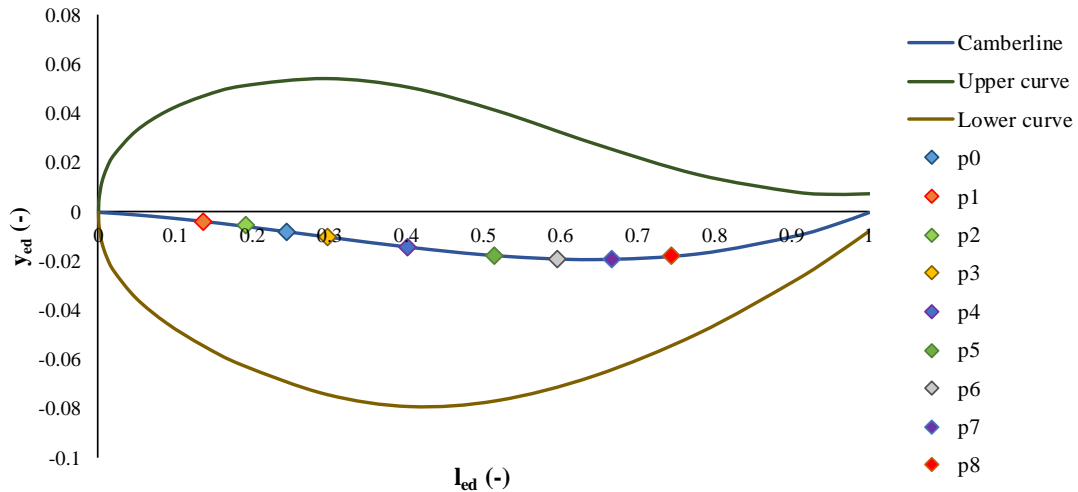


Figure 6-3. Analysed positions of the guide vane rotation axis

For each guide vane opening (represented as a percentage of the maximum openness  $a_{max}$ ) the change of the intensity and the direction of the moment of the blade is obtained depending on the position of its axis of rotation (Figure 6-4).

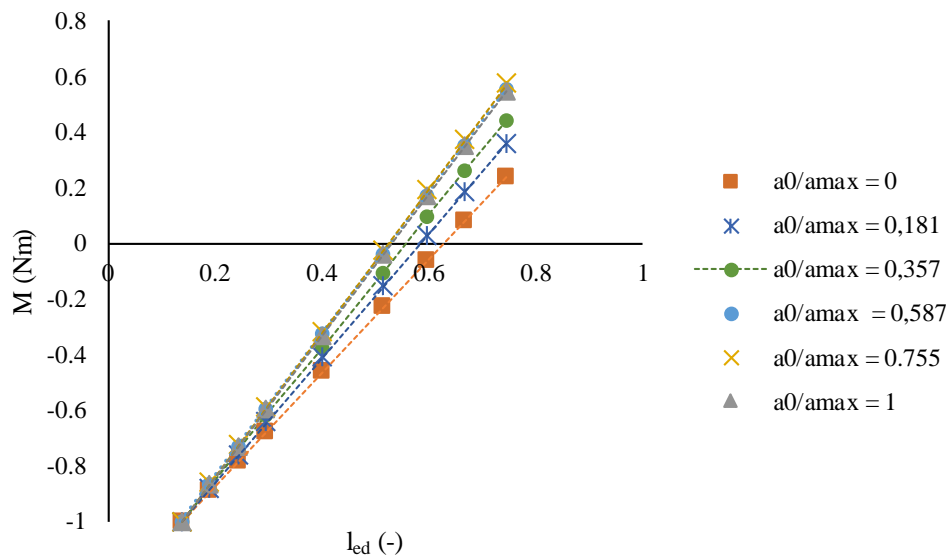


Figure 6-4. Variation of the blade torque by changing the position of the axis of rotation, for different openings of the guide vanes

The position of the axis of rotation is represented relative to the maximum length (of the chord) of the blade. The torque is also expressed in relation to the greatest torque that appears for the considered openness. The dependence is linear, since, for a specific openness of the guide vanes, the size and direction of the force remain the same, and, by changing the position of the axis, the distance to the acting line of the force changes. It can be seen that the maximum opening moments (negative sign) for any location on the axis of rotation are obtained in the closed position of the guide vanes, and they decrease with increasing  $a_0$  aperture. Closing

moments (positive sign) for the same axis of rotation are increased by opening the guide vanes. The intersection of each line with the apsis give the rotation point for which the torque is zero, i.e. through which the resultant forces passes for a certain opening. According to this, the resultant force acts between 52% and 63% of the guide vane length.

The change of the moment with opening of the guide vanes shows a different trend depending on the position of the axis of rotation (Figure 6-5). For axes of rotation that are up to a maximum of 40% of the chord length (points P1, P2, P0, P3, and P4), there is only an opening moment, i.e. self-closing of the guide vanes would not be ensured.

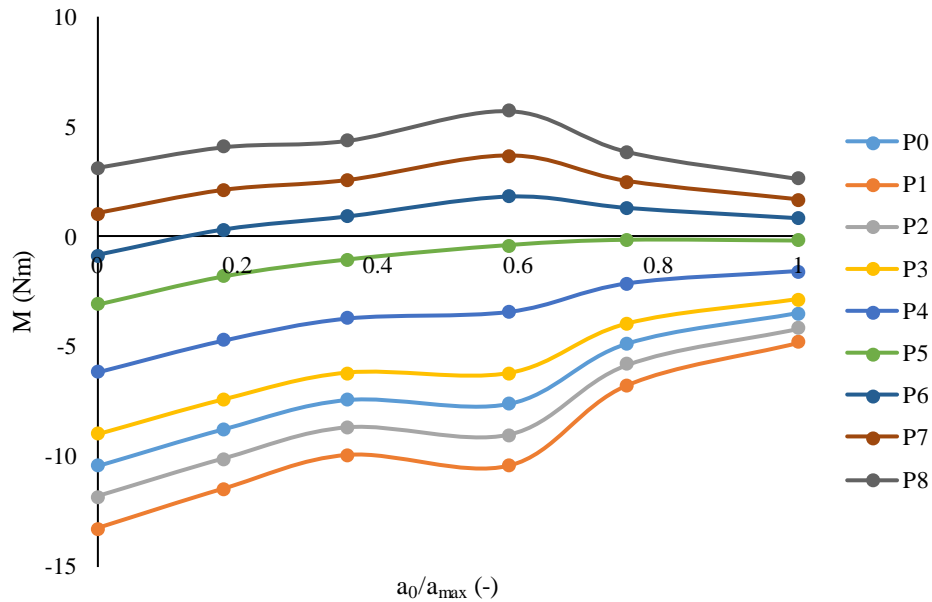


Figure 6-5. Variation of the blade torque by opening the guide vanes, at different axes of rotation

At the same time, the extreme moment that occurs in the closed position for these points, as well as the extreme moment that occurs in this case at the opening that corresponds to the optimal operating mode of the turbine ( $a_0/a_{\max} = 0.6$ ), are higher compared to the extremes that are obtained for the other axes of rotation.

For axes located in the zone after 65% of the chord length (points R7 and R8), self-closing is achieved, but the extreme moments are greater. Applying point P5 as the axis of rotation gives smaller extreme moments (except in the closed position), not self-closing, but approximately zero moment at larger openings. The desired trend of changing the moment by opening the guide vanes would be closest to the point P6 located on the guide vane camber-line, at 60% of the length of the chord. In this case, the moment in closed guide vanes is lower in intensity, and, with a small openness, a moment of zero is achieved.

With further opening of the guide vanes, the torque increases in the closing direction and reaches the maximum value at the optimal operating point. Until the maximum opening of the blades, the moment gradually decreases with the same sign (closing) and approaches the value of zero.

### 6.3.1 Selection of guide vane rotation axis position

Previous analyses of the impact of the rotation axis position show that the optimal axis is located between points P5 and P6, closer to point R6 due to the conditions it provides - smaller extreme moments and a tendency to self-closing. On the other hand, it can be seen that these conditions are achieved when by selecting the point of rotation a zero moment is achieved at a lower opening of the guide vanes. Therefore, two approaches are presented for selecting the appropriate position of the axis of rotation.

#### 6.3.1.1 Selection of the rotation axis position based on the equalisation of the extreme moments acting on the blade

Having the values of the moments at different openings of the guide vanes for the axes of rotation P5 and P6 between which the optimal position is expected, there is an intersection between the lines of the extremes, i.e. one line obtained from the moments acting on the blade in the closed position (first extreme) and the second line obtained from the moments of openness 0,6amax (second extreme observed for the optimal operating point), for the two selected axes of rotation (Figure 6-6).

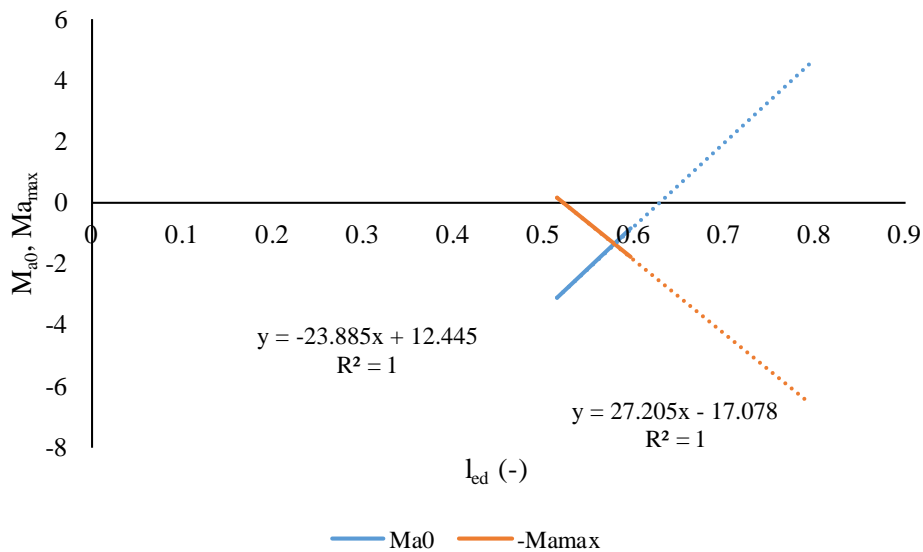


Figure 6-6. A point of rotation for which extreme moments of the same order of magnitude would be obtained

To achieve approximately the same extreme values of the moments (in the closed position and in the optimal openness), the axis of rotation should be positioned on the camber-line, at 57.8% of the length of the chord (x-coordinate). Extreme moments of  $\pm 1.36$  Nm are obtained. This point of rotation achieves smaller moments at all openings of the guide vanes (compared to those obtained at all other points of rotation considered), except in the closed position. This idea of equal extreme moments magnitude is suggested by Nechleba [48] as presented in Figure 3-17 and also implemented by Muntean et al. [23].

### 6.3.1.2 Selection of the rotation axis position based on the achievement of a zero moment at a small opening of the guide vanes

A model for calculating the blade rotation point coordinates was developed which would provide zero moment at low opening of the guide vanes, which, according to the previous analysis of numerically obtained results, will cause a tendency to self-closing with increasing openness, as well as generally smaller moments at different working conditions.

The intensity of the total (resultant) force  $F_R$  acting on the blade at a small opening of the guide vanes (assuming the case  $0.2a_{\max}$ ) is calculated through its components along the x-axis  $F_x$  and on the y-axis  $F_y$ :

$$F_R = \sqrt{F_x^2 + F_y^2} \quad [N] \quad 6-6$$

The direction of the resultant force is determined by the angle  $\theta$  with the vertical:

$$\theta = \arctg \frac{F_x}{F_y} \quad [^\circ] \quad 6-7$$

The torque acting on the blade around the axis passing through the coordinate origin (parallel to the blade height)  $M_0$  is used to calculate the normal distance between the acting line of the resulting force and the vertical axis through the coordinate origin:

$$l_0 = \frac{M_0}{F_R} \quad [m] \quad 6-8$$

A linear equation can be defined that mathematically describes the acting line of the resultant force acting on the considered guide vane in the given coordinate system for the numerical model:

$$y = ctg\theta \cdot x + \frac{l_0}{\sin\theta} \quad 6-9$$

The camber-line of the hydrofoil–guide vane is represented by a second-order polynomial with coefficients  $k_{f1}$ ,  $k_{f2}$   $k_{f3}$ :

$$y = k_{f1}x^2 + k_{f2}x + k_{f3} \quad 6-10$$

for the given coordinate system and for the position of the considered blade in space.

The intersection of the two curves defines a point of rotation for which a moment zero would be achieved, i.e. the point through which the acting line of force passes ( $l_0 = 0$ , then  $M = 0$ ), shown in Figure 6-7.

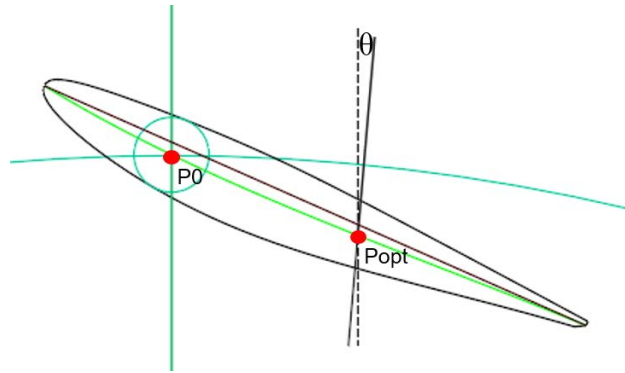


Figure 6-7. Point of rotation for which a moment  $M = 0$  would be achieved at a small opening

### 6.3.1.3 Comparison of results using two approaches for rotation axis position selection

Applying the first approach gives a point  $P_{opt2}$ , and applying the second approach a point  $P_{opt}$ , in the zone between points  $P_5$  and  $P_6$  (Figure 6-8). The first approach gives a more favourable state of changing moments by opening the guide vanes as it achieves a lower (extreme) moment at the optimal operating point and smaller moments at different openings, although at the expense of increasing the moment acting on the guide vane in a closed position. The two extreme moments are approximately equal in magnitude. The second approach achieves the required trend of changing the moment of the blade with the openness, but the intensity of the values is higher, which indicates that by setting a criterion for obtaining a zero moment at a greater openness than the given ( $0.2a_{max}$ ) the situation could be obtained as in the first approach.

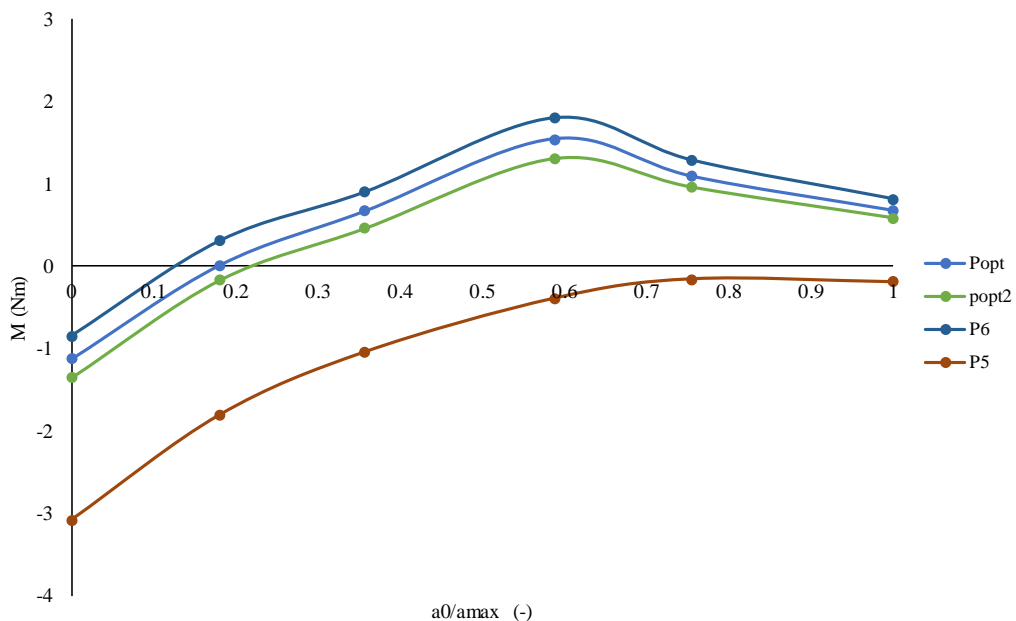


Figure 6-8. Variation of the moment with the opening of the guide vanes in the newly acquired blade rotation axis positions by applying two approaches

Using the second approach for guide vane pivot axis rotation, 15% lower torque at the opening corresponding to BEP is achieved, while first approach gives 25% torque decrement, compared to the point P6. Although the first approach gives more accurate results in selecting the optimal position of the rotation axis, the second approach would be more practical to apply - after redefining the openness that requires zero moment - due to the direct calculation and the possibility of implementation in CFD and FEA software.

### 6.3.2 Impact of rotation axis on the guide vane static loads

The provided methods of calculating rotation axis position are aimed at obtaining the lowest possible stresses and deformations of the guide vane. Prediction of blade strength behaviour can be performed by simulating the interaction between fluid and solid surface, using numerically calculated hydrodynamic forces to solve equations of solid body mechanics [64] [65].

Using software based on the finite element method, the impact of changing the position of the rotation axis on the stress distribution and deformation of the guide vane is analysed. The already obtained optimal position of the axis of rotation through the first approach is used and compared to points P5 and P6, as well as the original point P0. For that purpose, a numerical model of a guide vane with a shaft and bearings has been developed, which is tested using the finite element method.

#### 6.3.2.1 Numerical model of guide vane for strength analysis

To develop the numerical model, the previously considered guide vane is used, and a shaft is added to obtain a more accurate strength analysis. A model shaft is used according to the model in the NTNU Hydropower Laboratory.

The number of cells in the numerical grid is selected after conducting a mesh independence test of the numerical solution (Figure 6-9).

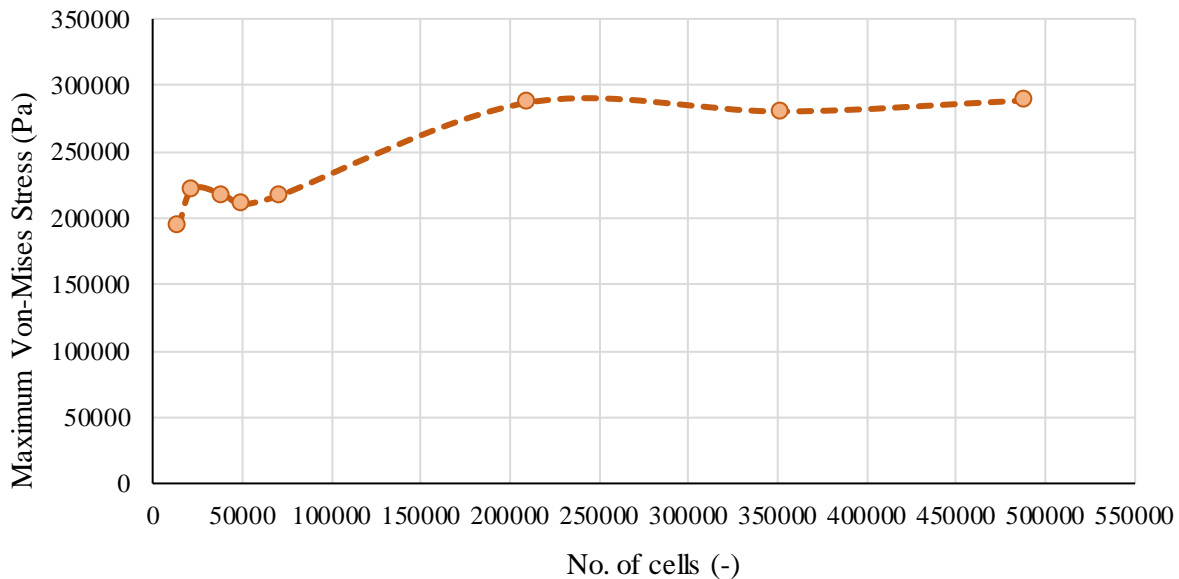


Figure 6-9. Test for the independence of the numerical solution from the grid

All simulations are performed with the same type of grid, with about 200,000 cells. The boundary conditions used are: fixed support (support D) and frictionless support (supports F and E), shown in Figure 6-10.

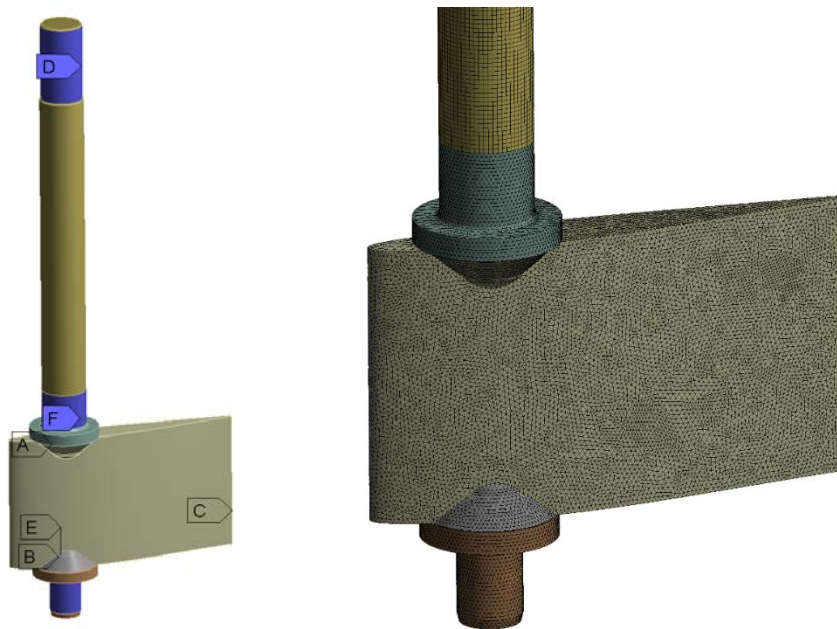


Figure 6-10. Boundary conditions (left) and numerical grid (right)

The variable load, i.e. the pressure distribution obtained from the CFD simulations of the water flow through the guide vanes is transferred to the solid surface of the blade to perform the strength analysis.

#### 6.3.2.2 Comparison of strength analyses results

The state of stresses and deformations is obtained for a shaft blade whose axis is positioned through points P0, P6, and Popt, respectively. The strength analyses refer to the guide vanes openness which corresponds to the optimal operating point where the second extreme moment is observed. The stress distribution of the blade (Figure 6-11) shows a decrease in the value of the maximum stress by changing the shaft axis from the initial position P0 to position P6, which in previous analyses indicated a lower moment in the optimal opening on the guide vanes. The maximum stress is further reduced by changing the shaft position from point P6 to point Popt determined by the criterion for obtaining extreme moments of the same magnitude. In all three cases, the critical zones are the contact surfaces of the blade with the shaft.

Figure 6-12 shows the total deformation of the blade for the three positions on the shaft axis. The value of maximum deformation is higher for the initial pivot axis P0 compared to the axis P6 and Popt. Moving the pivot axis from P6 to Popt gives 28% lower value of the maximum deformation.

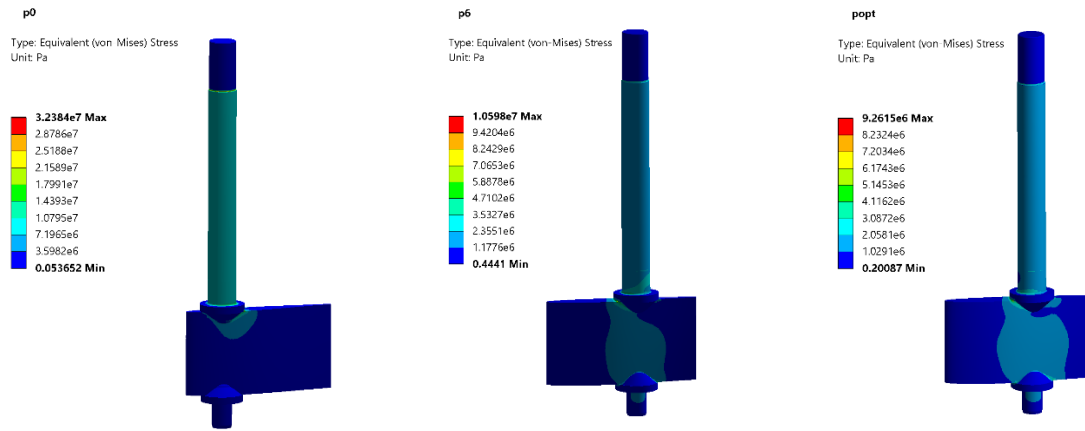


Figure 6-11. Distribution of stresses in the guide vane for different positions of the shaft

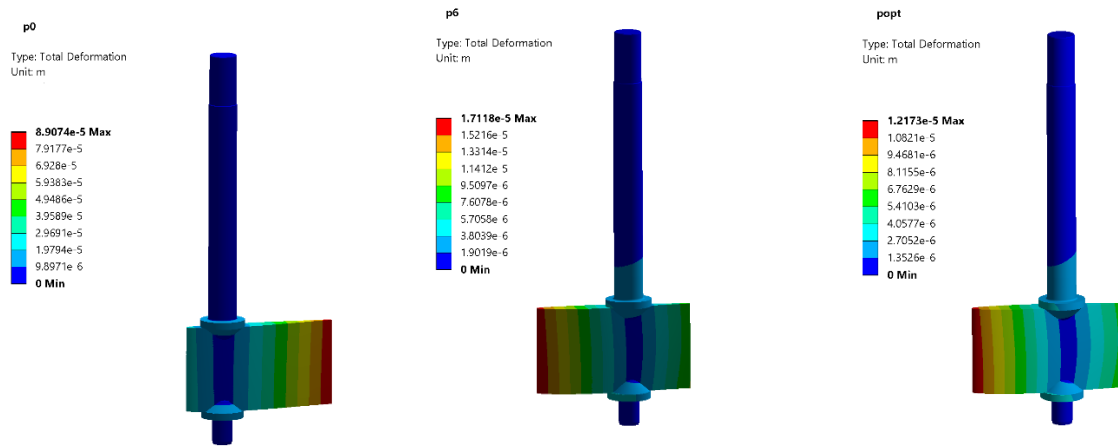


Figure 6-12. Deformations of guide vanes for different positions of the shaft axis

## 6.4 Influence of variable speed on static loads of the blade

Using the three-dimensional model, simulations were performed at different runner speeds,  $\pm 20\%$  of the nominal speed. It can be noticed that pressure profiles are obtained that differ in shape and intensity, which is especially pronounced on the guide vane suction side which is more exposed to the impact of the presence of the runner. According to the results, the pressure on the back surface increases with the number of revolutions which gives higher pressure difference between the guide vane surfaces. Consequently the guide vane torque increases with runner speed rise (Table 7). In this case, the torque at the nominal speed is 1.25% smaller than at  $+20\%$  of the nominal speed, and 1,45% higher than at  $-20\%$  of the nominal speed.

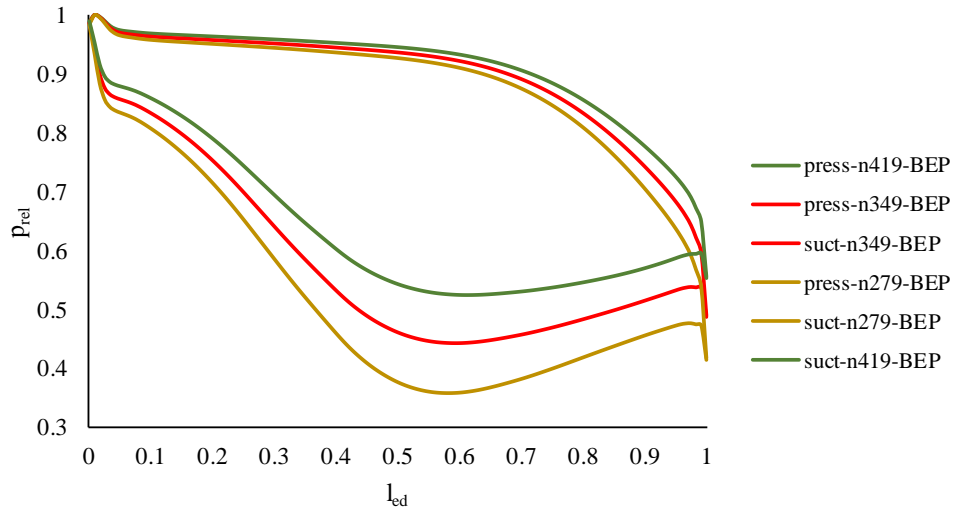


Figure 6-13. Pressure profiles at different rotational speeds  
 Table 7. Guide vane torque for different runner speed

Runner speed n (rad/s)	Guide vane torque M (Nm)
27.9	-7.516
34.9	-7.609
41.9	-7.72

After transferring the pressure distribution to the guide vane, at different rotational speeds, an analysis was performed with the FEA method at the same axis of rotation. It can be concluded that in this case the value of the maximum stress and the maximum total deformation increase with the number of revolutions rise. The maximum stress at the nominal speed is 1.43% smaller than at +20% of the nominal speed, and 1,21% higher than at -20% of the nominal speed. The maximum total deformation at the nominal speed is 1.27% smaller than at +20% of the nominal speed, and 1,51% higher than at -20% of the nominal speed.

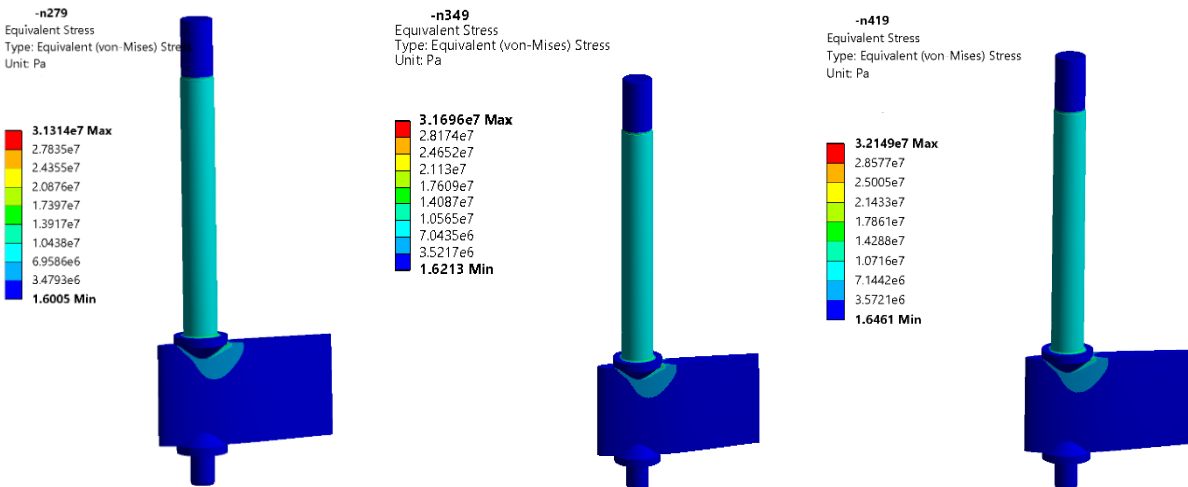


Figure 6-14. Guide vane stress distribution for different rotational speeds

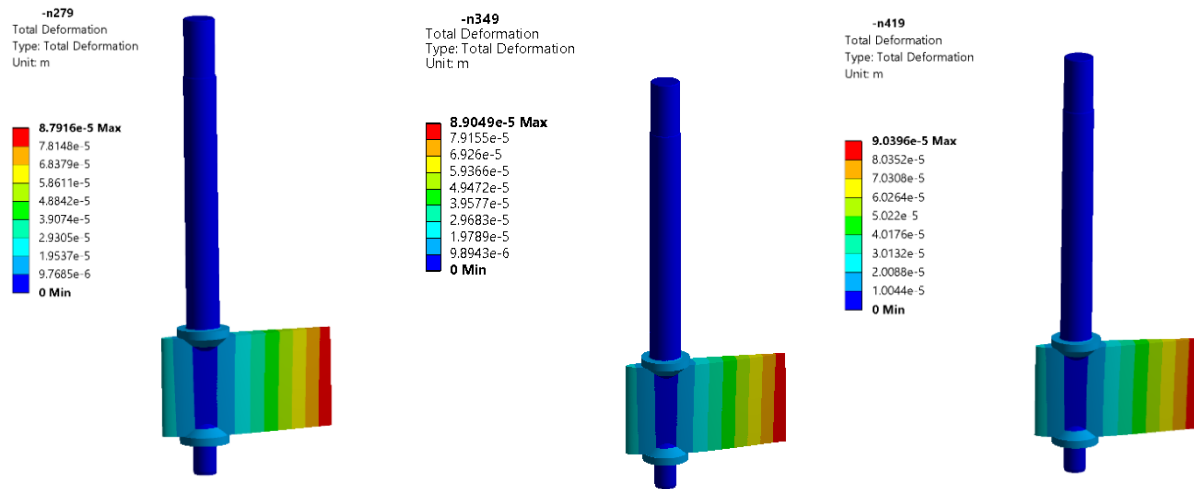


Figure 6-15. Deformations of the guide vane at different rotational speeds

## 6.5 Automated software implementation

To determine the position of the axis of rotation, the calculation described above for achieving zero moment at low aperture is implemented in MATLAB and ANSYS Workbench. The shape of the guide vane is defined in MATLAB by equations of the upper and lower contours.

By applying transformations (translations and rotations), the position of the blade in the coordinate system is obtained. MATLAB code has been adapted to be called by a Python script and to communicate with ANSYS Workbench. MATLAB script is created as a function with extension \*.m that can receive input parameters and give output parameters - output parameter = function (input parameter).

A function is used to write the coordinates of the blade in a txt file, which is needed to generate the geometry in SpaceClaim. Thanks to the ability to script in ANSYS Workbench, it is possible to automate the process of generating geometry and numerical calculation. The connection between the two software is realised through the External Connection module through xml script. The connection between the input and output parameters is created with the parameter set in the ANSYS Workbench [66].

By positioning the blade for a small opening relative to the initial axis of rotation, the required coefficients that define the camber-line of the hydrofoil can be calculated. By automating the process of generating the guide vane geometry, numerical mesh and simulations, and extracting moment and force as output parameters, the coordinates of the point of rotation can be defined.

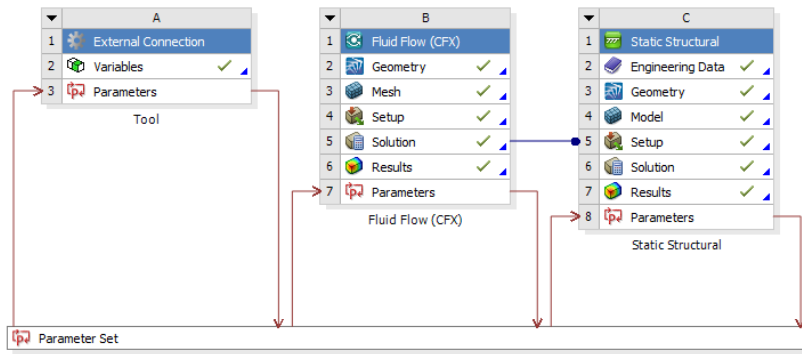


Figure 6-16. Tool for determining the axis of rotation based on the second approach

## **7 Spiral casing hydraulic design**

### **7.1 Introduction**

#### **7.1.1 Spiral casing in hydraulic turbines**

The water intake and the penstock in a hydraulic turbine deliver the flow entering the spiral casing. Spiral casing is a reaction turbine component that ensures water inflow and even distribution of water in front of the stay vanes. It guides the water at optimal angle from the stay vanes through the guide vanes into the runner for effective utilisation of the available kinetic energy. The spiral casing directs the water in the stay vanes giving it a tangential velocity component thus providing certain momentum of the water striking the runner blades.

Despite decreasing the water flow rate along the stay vane perimeter, the spiral casing maintains uniform velocity and pressure distribution of the water at the stay vane inlet. This is obtained by the gradual diameter decrement of the spiral. Because of the even water distribution in front of the runner ensured by the spiral casing, the turbine is efficiently used for the given flow rate.

Moreover, the uniform pressure distribution along the stay ring periphery contributes for the minimisation of loads since radial forces acting on the runner are almost zero [44]. In order to achieve a proper functioning of the spiral casing, its cross-sections must fulfil certain requirements. The sectional area of the spiral chamber decreases in the flow direction.

#### **7.1.2 Brief literature review of previous scientific research in the area of spiral casing design**

The understanding of the flow in the spiral casing is very important and it can be gained through a numerical analysis performed by means of CFD software. Dahal D. R. et al. numerically analysed free-vortex types of spiral casings with circular, trapezoidal, and square cross-section. The aim was to find the best casing configuration for a micro Francis turbine which gives minimal pressure loss and provides required inflow conditions for stay vanes. An iterative process is used to design the spiral casing so that previously defined inlet velocity of stay vanes is obtained. Comparisons were made based on the distribution of pressure and radial and tangential velocity. It was concluded that reducing the casing dimension in the radial direction without change in the section area does not significantly affect the radial velocity. The observation was made that trapezoidal configuration is most appropriate for such applications [67]. Shrestha and Choi [68] numerically optimised the spiral casing shape using response surface methodology (RSM) and multi-objective genetic algorithm. Improvement of the stay vane inlet conditions is shown by the optimal design. Nakkina et al. [69], [70] numerically investigated fluid flow characteristics of accelerated, free-vortex, and decelerated types of spiral casings with different aspect ratios to obtain optimal design regarding spiral velocity coefficient, total pressure loss, and average radial velocity. Desai et al. [71] compared the hydraulic performance of spiral casings with circular and elliptical cross-sections, respectively, designed for high-head Francis turbines. The CFD-based analysis showed better radial velocity distribution, less flow separation, higher efficiency, smaller head drop and smaller velocity, and

total pressure loss of the elliptical configuration. Kurokawa and Nagahara [72] investigated the behaviour of accelerated, free-vortex, and decelerated spiral casing type with circular sections and found out that the decelerated type shows best performance. In addition, they concluded that optimal configuration can be achieved by reducing the tangential velocity. Other authors, such as Maji and Biswas [73], studied only free-vortex type of spirals with circular cross-sections to numerically obtain the pressure and velocity distribution and secondary flow behaviour.

In order to find an optimal spiral casing configuration or to make a hydraulic redesign of an existing spiral, different geometries can be tested or numerical optimisation techniques can be applied. In both cases, parametrisation of the spiral casing complex geometry can be introduced by defining the Francis turbine spiral casing with a certain number of parameters. A new methodology of Francis turbine spiral casing hydraulic design is proposed based on the free-vortex law and Archimedes central spiral line. The spiral casing performance is determined by a CFD analysis.

## 7.2 Spiral casing hydraulic design methodology

### 7.2.1 Calculation methodology

The first requirement of a spiral casing to uniformly distribute the water flow along the guide vane circumference implies that the discharge through a meridional section of the spiral casing determined by the angle  $\varphi$  is:

$$Q_{\varphi} = Q \frac{\varphi}{360^{\circ}} \quad 7-1$$

where  $Q$  [m<sup>3</sup>/s] is the total discharge through the spiral casing and  $\varphi$  [°] is the wrapping angle measured from the end of the spiral tooth [74].

#### 7.2.1.1 Inlet section

The design procedure starts from the inlet section defined by the coverage angle  $\varphi_{cov}$ , the inlet water flow rate  $Q_{in}$  and the inlet peripheral velocity  $v_{uin}$  (Figure 7-1 left).

The coverage angle is defined as the angle enveloped between the inlet section of the spiral case and the end of the spiral tooth. The angle of the spiral tooth is taken as  $\varphi_{s.t.}=15^{\circ}$ , so the coverage angle is:

$$\varphi_{cov} = 360^{\circ} - \varphi_{s.t.} = 345^{\circ} \quad 7-2$$

The discharge at the spiral inlet section is calculated as:

$$Q_{in} = 3Q \frac{\varphi_{cov}}{360^{\circ}} \quad 7-3$$

The inlet peripheral velocity can be determined based on two approaches. The first one is according to the turbine net head  $H_n$  by the expression [75]:

$$v_{u,in} = 1,93 \cdot H_n^{0.33} \quad 7-4$$

used for steel spiral casings with prototype dimensions (Figure 7-1 right).

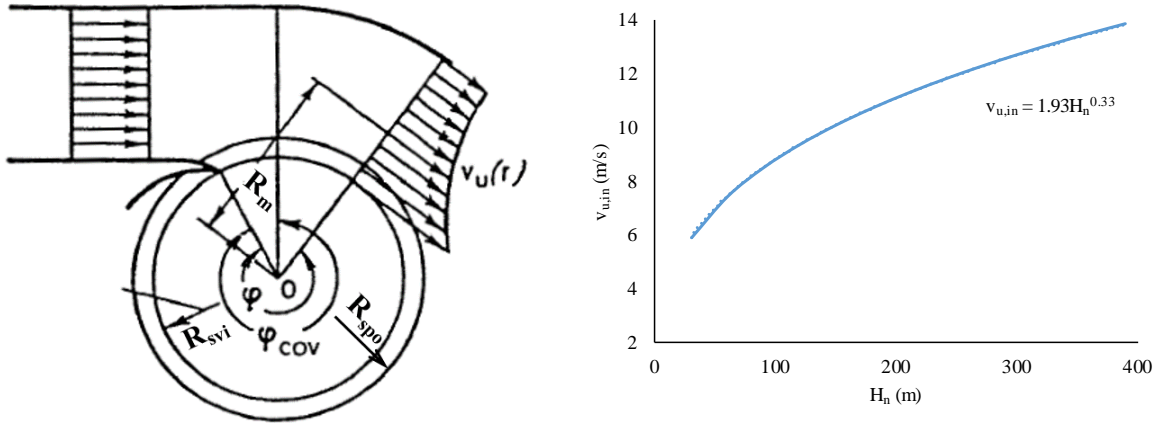


Figure 7-1. a) Basic parameters of spiral casing; b) Dependence of spiral casing inlet velocity on turbine net head

The latter is by presetting the direction of the stay vanes inlet velocity  $v_{sv,in}$  defined by the stay vanes inlet angle  $\alpha_{sv,in}$  to be coincided with the outlet angle of the spiral streamline  $\alpha_{spo}$ :

$$\tan\alpha_{spo} = \frac{v_{r,spo}}{v_{u,spo}} \quad 7-5$$

By setting a value for  $\alpha_{spo}$  between  $26^\circ$  and  $34^\circ$ , the peripheral velocity at the spiral case inlet section is taken as:

$$v_{u,in} = v_{u,spo} = \frac{v_{r,spo}}{\tan\alpha_{spo}} \quad 7-6$$

where  $v_{r,spo}$  is the radial velocity at spiral outlet calculated as:

$$v_{r,spo} = \frac{Q}{D_{spo}\pi B_{sv}} \quad 7-7$$

for a given stay ring inlet diameter  $D_{svi}$  and stay vane height  $B_{sv}$  (Figure 7-2).

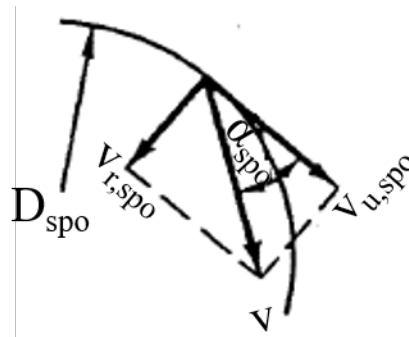


Figure 7-2. Calculating the spiral casing inlet section velocity

The spiral casing consists of circular and elliptical sections. The circle or ellipse is vertically cut with height denoted as  $t$  that changes along the spiral outlet periphery.

The area of the inlet section is then:

$$A_{ef,in} = \frac{Q_{in}}{v_{u,in}} \quad 7-8$$

for which a radius of a full circle can be found:

$$r_{in0} = \sqrt{\frac{A_{ef,in}}{\pi}} \quad 7-9$$

For a given value of spiral height at inlet section  $t_{in} > B_{sv}$ , the angle  $\alpha_{in0}$  can be calculated as:

$$\frac{\alpha_{in,0}}{2} = \arcsin \frac{t_{in}}{2r_{in0}} \quad 7-10$$

The area of the cut circle is determined:

$$A_{ef0} = r_{in0}^2 \left[ \pi \left( 1 - \frac{\alpha_{in,0}}{360} \right) + \sin \frac{\alpha_{in,0}}{2} \cos \frac{\alpha_{in,0}}{2} \right] \quad 7-11$$

The last two equations are used to find the radius of the inlet cut circle  $r_{in} > r_{in0}$  whose effective area is equal to the calculated area of the inlet section  $A_{ef,in}$ , taking  $r_{in0}$  as an initial value.

## 7.2.2 Basics of the hydraulic design

The spiral casing hydraulic design is developed based on the Archimedean spiral equation and the law of constant moment of velocity.

The general equation of the Archimedean spiral is applied to the spiral casing central line which connects the centres of the circles and/or ellipses. Calculating the distance from the centre of the inlet section cut circle to the stay vane inlet as follows:

$$m_{in} = \sqrt{r_{in}^2 - \left(\frac{t_{in}}{2}\right)^2} \quad 7-12$$

we can determine the location of inlet section circle centre in relation to the turbine axis:

$$R_{m,in} = R_{svi} + m_{in} \quad 7-13$$

Taking into account that the inlet centre lies on the central line defined by Archimedean spiral, its coefficient can be expressed as:

$$a = \left( \frac{R_{m,in}}{R_{svi}} - 1 \right) \frac{360}{\varphi_{cov}} \quad 7-14$$

where  $R_{svi} = \frac{D_{svi}}{2}$ .

For the rest of the sections defined by angle  $\varphi$ , the radii of the spiral central line are as follows:

$$R_{m\varphi} = R_{svi} + aR_{svi} \frac{\varphi}{360} \quad 7-15$$

while the distance from the centre of the respective section to the stay vane inlet is:

$$m_\varphi = R_{m\varphi} - R_{svi} \quad 7-16$$

The free vortex type of spiral casing is chosen, which follows the law of constant moment of velocity applied at the central line:

$$v_{u\varphi} R_{m\varphi} = c = const \quad 7-17$$

where  $v_{u\varphi}$  is the peripheral velocity at a given section of the spiral determined by angle  $\varphi$  and evaluated in a point at a distance  $r_\varphi$  from the spiral case axis (i.e. turbine axis).

Applying the law at the spiral case inlet section, the constant  $c$  is determined:

$$c = v_{uin} R_{m,in} \quad 7-18$$

and used to find the velocity at each section:

$$v_{u\varphi} = \frac{c}{R_{m\varphi}} \quad 7-19$$

#### 7.2.2.1 Calculation of sections

The area of a certain section at angle  $\varphi$ , required to provide the discharge  $Q_\varphi$  is:

$$A_{ef\varphi} = \frac{Q_\varphi}{v_{u\varphi}} \quad 7-20$$

Assuming each section is a cut circle, the minimal value of its radius and angle would be:

$$r_{\varphi,min} = \sqrt{m_\varphi^2 + \left(\frac{B_{sv}}{2}\right)^2} \quad 7-21$$

and

$$\frac{\alpha_{\varphi,min}}{2} = \arcsin \frac{B_{sv}}{2m_\varphi} \quad 7-22$$

respectively.

The minimal required area of the respective section is then calculated as:

$$A_{\varphi,min} = r_{\varphi,min}^2 \left[ \pi \left( 1 - \frac{\alpha_{\varphi,min}}{360} \right) + \sin \frac{\alpha_{\varphi,min}}{2} \cos \frac{\alpha_{\varphi,min}}{2} \right] \quad 7-23$$

If  $A_{ef\varphi} > A_{\varphi,min}$ , the section shape is circular (Figure 7-3 left). An initial value of the circle radius is calculated:

$$r_{\varphi 0} = \sqrt{\frac{A_{ef\varphi}}{\pi}} \quad 7-24$$

The starting value of the angle  $\alpha_\varphi$  can then be calculated:

$$\frac{\alpha_{\varphi 0}}{2} = \arccos \frac{m_\varphi}{r_{\varphi 0}} \quad 7-25$$

The area of the cut circle with initial parameters is:

$$A_{ef0} = r_{\varphi 0}^2 \left[ \pi \left( 1 - \frac{\alpha_{\varphi 0}}{360} \right) + \sin \frac{\alpha_{\varphi 0}}{2} \cos \frac{\alpha_{\varphi 0}}{2} \right] \quad 7-26$$

The last two equations are used to find the value of the angle  $\alpha_\varphi$  for the previously determined area  $A_{ef\varphi}$  of the section considered. The section height is:

$$t_\varphi = 2m_\varphi \tan \frac{\alpha_\varphi}{2} \quad 7-27$$

while the radii of the circular sections can be calculated as:

$$r_\varphi = \sqrt{m_\varphi^2 + \left( \frac{t_\varphi}{2} \right)^2} \quad 7-28$$

If  $A_{ef\varphi} < A_{\varphi, \min}$ , the section shape is elliptical (Figure 7-3 right). For a height  $t_{\varphi'}$  smaller than the height of the last circle, the angle of the ellipse at the section considered  $\theta_\varphi$  and the distance  $r_{\varphi'}$  are calculated as follows:

$$\theta_\varphi = \arctan \frac{m_\varphi}{t_{\varphi'}/2} \quad 7-29$$

$$r_{\varphi'} = \sqrt{m_\varphi^2 + \left( \frac{t_{\varphi'}}{2} \right)^2} \quad 7-30$$

Applying the equations for an ellipse, the major axis  $a_{el}$  is expressed with:

$$a_{el} = \sqrt{\frac{-k_1 + \sqrt{k_2^2 - 4k_1k_3}}{2k_1}} \quad 7-31$$

where  $k_1 = (r_{\varphi'} \pi \sin \theta)^2$ ,  $k_2 = -A_{ef\varphi}^2$  and  $k_3 = (r_{\varphi'} \pi \cos \theta)^2$ .

The half ellipse which is cut has a minor axis  $b_{el}$ :

$$b_{el} = \frac{A_{ef\varphi}}{a_{el}\pi} \quad 7-32$$

while the other half has a corrected value of  $b_{cor}$  so that the required effective area of the section can be achieved.

The area of the part of the ellipse defined by the angle  $\theta_\varphi$  is calculated as:

$$F = \frac{a_{el}b_{el}}{2} \left[ \theta - \arctan \frac{(b_{el} - a_{el})\sin 2\theta}{b_{el} + a_{el} + (b_{el} - a_{el})\cos 2\theta} \right] \quad 7-33$$

The area of the other part of the ellipse has an area:

$$A_{cor} = A_{ef} \left( 2F + m_{\varphi} \frac{t_{\varphi}'}{2} \right) \quad 7-34$$

Then, the value of the minor axis for the new ellipse would be:

$$b_{cor} = \frac{2A_{cor}}{a_{el}\pi} \quad 7-35$$

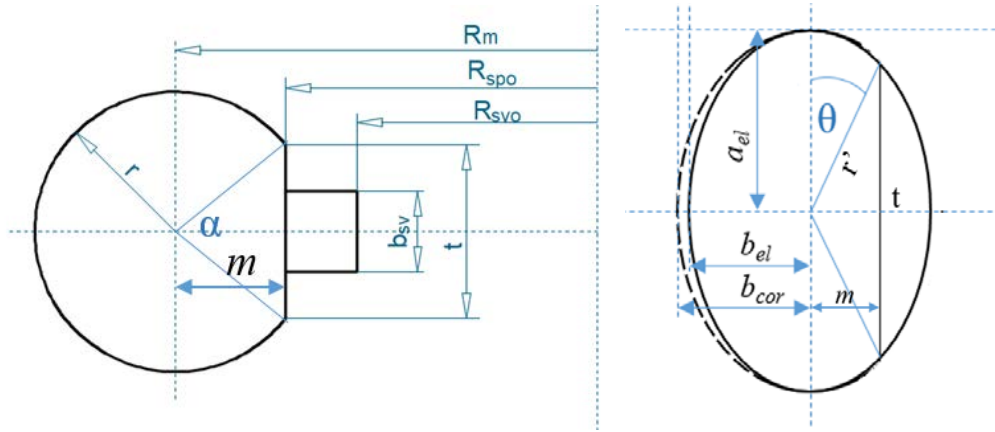


Figure 7-3. a) Geometry parameters of a circular cross-section, b) Geometry parameters of an elliptical cross-section

### 7.3 Validation of the spiral casing hydraulic design

Validation of the calculation methodology and achievement of the required performance is made by numerically testing a low specific speed Francis turbine. A suggested redesign of the spiral casing of the Francis-99 turbine model in the Waterpower Laboratory is done. The parameters in Table 8 are used.

Table 8. Spiral casing parameters

Discharge Q (m <sup>3</sup> /s)	0,2 m <sup>3</sup> /s
Net head H <sub>n</sub> (m)	11,4 m
Stay vane inlet diameter D <sub>svi</sub> (m)	0,98 m
Coefficient of spiral casing outlet increment C <sub>spo</sub> (-)	1,05
Stay vane height B <sub>sv</sub> (m)	0,06 m
Spiral casing outlet streamline angle α <sub>spo</sub> (°)	30°

Since this is a turbine model, the expression for calculating the peripheral velocity according to the net head is not used. Furthermore, new stay vanes are introduced, so the peripheral velocity at the spiral casing outlet is chosen to be coincident with the stay vane inlet

velocity direction defined by the stay vane inlet angle, i.e. the spiral casing outlet streamline

$$\text{angle } \alpha_{spo}, v_{u,in} = v_{u,spo} = \frac{v_{r,spo}}{\tan \alpha_{spo}}$$

Geometry configuration of spiral casing is given in Figure 7-4 where the contours of the spiral casing diameter, the central spiral line by the radius  $R_{m\phi}$  changing with the angle  $\phi$  and the outer contour with radius  $R_{a\phi} = R_{m\phi} + r_{\phi}$  changing with the angle  $\phi$ .

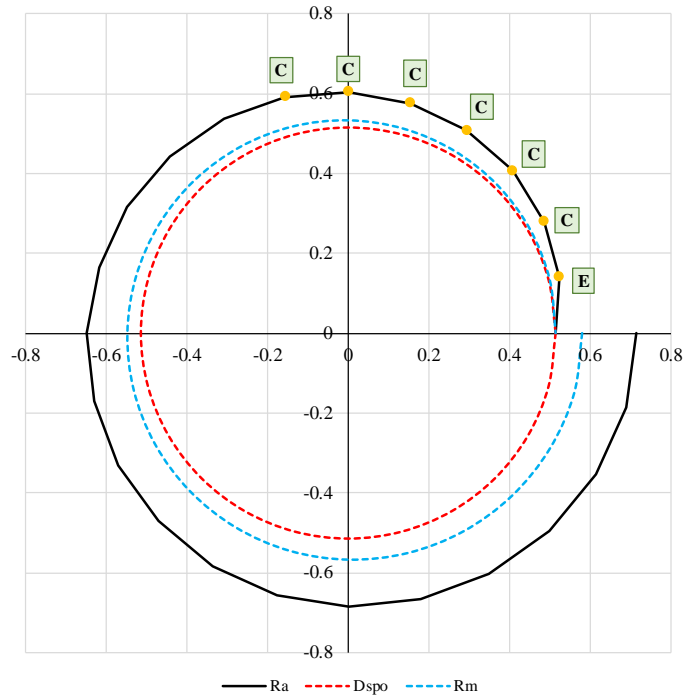


Figure 7-4. Geometry of new design of spiral casing

Design control is performed by confirming the continuous change of the outer radius, the radius of the circular sections and the height of the sectioning depending on the angle  $\phi$ , given in Figure 7-5.

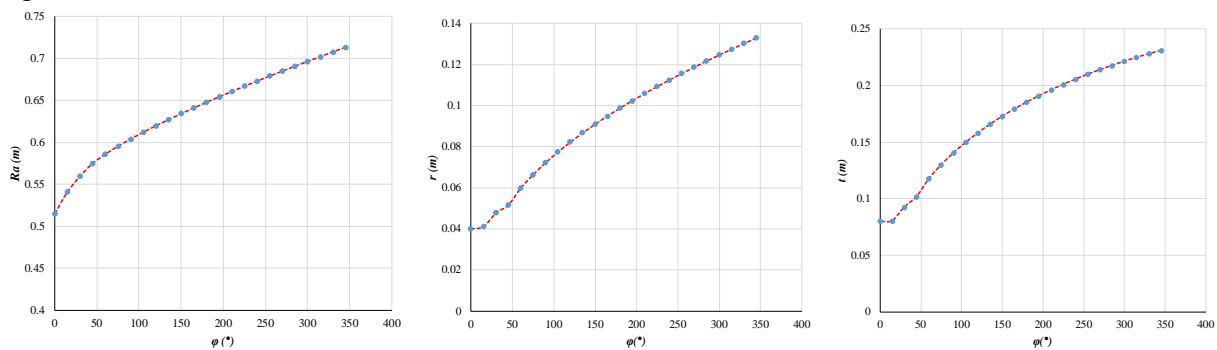


Figure 7-5. Change of  $R_a$ ,  $r$  and  $t$  along the angle  $\phi$

Steady three-dimensional water flow through the spiral casing and stay ring with The number of stay vanes is  $Z_{SV} = 14$  stay vanes is modelled and simulated applying mass flow rate as

inlet boundary condition. The three-dimensional model is built in the CFD software where a numerical fluid flow model is developed (Figure 7-6).

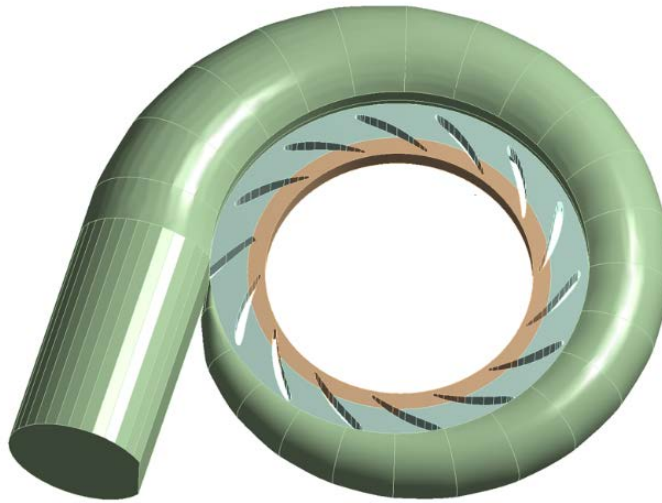


Figure 7-6. 3D geometry model of spiral casing

Velocity distribution in the spiral casing and at certain cross-sections is presented in Figure 7-7.

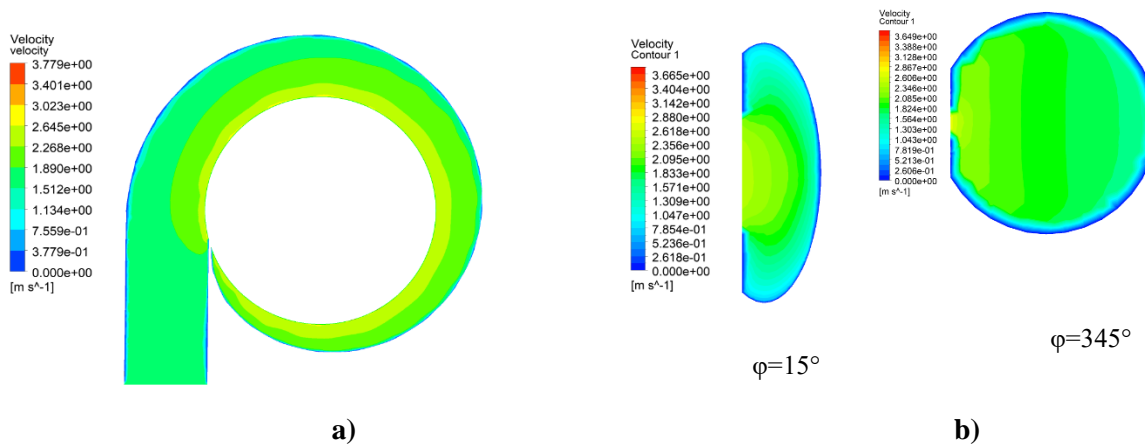


Figure 7-7. Velocity distribution in spiral casing (a) and at different cross-sections (b)

The uniformity of the distributed flow through the spiral casing sections is confirmed by the linear change of the discharge  $Q$  with the wrapping angle  $\varphi$ . A comparison of the theoretical values of the discharge for every section  $Q_\varphi$  with the numerically obtained values is made (Figure 7-8).

From the inlet section to the section at  $\varphi=120^\circ$ , the deviations from the theoretical discharge is maximum  $\pm 2.2\%$ , while from sections in the interval from  $\varphi=105^\circ$  to  $\varphi=75^\circ$  is  $4.2\%$ . The relative error is approximately  $8\%$  in sections at  $\varphi=60^\circ$  and  $\varphi=45^\circ$ . Higher deviations are

obtained in the last sections – around 17%, which is attributed to the spiral tooth construction which is not equally dividing the flow.

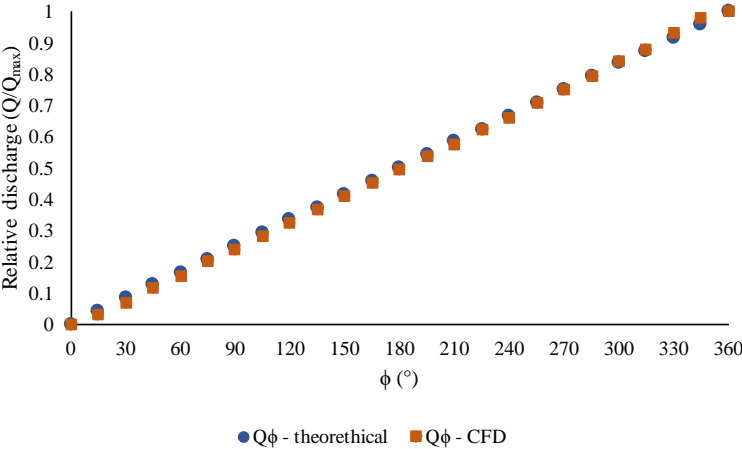


Figure 7-8. Comparison between theoretical and numerically obtained values of discharge through spiral casing cross-section

## 8 Conclusions and recommendations for further work

In order to accommodate the intermittent behavior of the future renewable system, hydropower plants have to be operated in a flexible manner which will cause as much as less fatigue of the turbine components.

The evaluation of a Francis turbine guide vane mechanical loads and their correlation to the cascade geometry parameters, blade pressure distribution, rotational axis position and variable speed of the turbine can indirectly introduce a higher flexibility to a hydro power plant. In this doctoral dissertation, experimental and numerical research was conducted to gather knowledge on the mechanical performance of the guide vanes, find a way to predict the guide vanes loads and detect the impact of the variable speed.

An analysis of the current achievements in the field of hydraulic turbines has been previously performed with emphasis on theoretical, experimental, and numerical research related to turbine loads. The correlation between the guide vane shape and its pressure distribution and the impact of variable speed on the strength performance of the guide vane are studied, in order to obtain an objective view of the outcomes (conclusions, claims, knowledge) from the previous research.

The second step was to present the theoretical background of the guide vane loads arising from the hydrodynamic forces, i.e. the fluid flow. A calculation model was developed based on the theoretical laws in order to determine the forces acting on the blade. The measurement results for pressure distribution on the aerofoil are used as a basis of the model. By inserting the experimental data, the model calculates the normal and axial force as components of the resultant force acting on the aerofoil.

The characteristics of an aerofoil have been investigated on an experimental system consisting of a wind tunnel, using appropriate measuring equipment to measure certain physical quantities. Emphasis is placed on the pressure distribution along the blade surface, which dictates the magnitude and direction of the forces acting on the blade and, consequently, on the stresses and deformations. The experimental investigation is performed for a solitary aerofoil positioned at different angles of attack in the flow field and for an aerofoil set in a radial cascade.

The subject of the experimental test is a central blade in a segment of a circular cascade with five blades, positioned so that the inflow is shock-free. Adjacent control blades were used to achieve the uniformity of the flow in the two inter-blade channels in which the central blade participates in. The end boundary blades that form the inlet part of the radial channel were used to obtain shock-free inflow on the central blade. Cascade measurements are preceded by:

- determining the average velocity and air flow rate in the duct by measuring the total pressure in the measuring sections of the duct, obtaining an even air velocity profile at the duct exit, i.e. an even flow at the entrance of the radial cascade. Position of one Pitot tube for measuring the average velocity in the channel is defined in order to gain data for the flow mode during the aerofoil measurements.
- determining the aerodynamic characteristics of a solitary profile by conducting pressure distribution measurements at different attack angles. The calculation model developed is

used to determine the moment and the normal and axial force which are transformed into the lift and drag force for different positions.

The measured pressures at the ten points distributed along the back and front surfaces of the central blade are given in relation to the maximum pressure at the corresponding mode (which in these cases is achieved at the front edge – shock-free entrance), i.e. as relative values so that the obtained pressure profiles be comparable. The position of the measuring points is given relative to the unit length of the profile.

From the comparison between the forms of pressure distribution for the central blade in the cascade at a given opening, it was seen that under different flow modes similar shapes of pressure profiles are obtained. The differences are in the intensity of the values of the absolute pressures for different flow modes

High and low density cascades were experimentally examined to see the effect of the cascade pitch on the blade loads. The normal force which was determined to be much more dominant than the axial force, was taken as a representative of the aerofoil loads.

Both types of cascades are described by geometric parameters such as inlet and outlet radius whose ratio defines the cascade relative width, cascade opening (also defined in relation to the aerofoil length, i.e. relative opening) and inflow angles. It is noted that both the relative width increment and the relative opening increment lead to loads reduction since the width and opening are directly proportional.

The presence of dependency between the mechanical quantities and the geometry parameters induced introduction of a radial cascade coefficient to describe the flow (loads) conditions in a cascade by its relative width and relative opening. Using this coefficient for every experimentally investigated cascade configuration of same type gives corrected forces distributions which are similar to each other i.e. can be described by same law.

For the high density cascade, additional influencing geometric parameter has been detected such as the overlapping length defined as the length of the aerofoil contributing to forming of the inter-blade channel. Higher overlapping length leads to loads decrement.

The correlation between the forces distribution on the aerofoil in a cascade with higher and lower density is obtained by introducing the radial cascade coefficient and the cascade pitch. The dependency is an exponential function both in the case of comparing dimensionless forces distribution of cascades and in case of establishing a ratio between the dimensionless characteristic corrected forces distribution for the different cascades along the aerofoil unit chord length. The derived correlations allow prediction of the aerofoil load force for different cascade pitch.

The numerical model for flow around a solitary aerofoil is validated by verifying the simulation results by comparing them with the experimentally obtained results. While most of the measured values show difference compared to the numerical values in acceptable range (0,5%-14%), the second and third measuring point show higher deviation for the lower surface pressure distribution. The experimental and numerical values of the lift force, the drag force and the moment at different aerofoil positions show 3%-28% discrepancy, except for attack angles of  $-20^\circ$  and  $-30^\circ$  where higher deviations were obtained. The larger differences between the experimental and numerical results can be due to different actual position of the aerofoil in the

experimental system compared to the real geometric position in the numerical model or different airflow conditions in the channel during the measurement.

The numerical models for flow through the circular lower and higher density cascade were validated by verifying the simulation results by comparing them with the experimentally obtained results. There is a good alignment between the numerically and experimentally obtained values of pressure with a discrepancy up to 7% and 7,7% for the case of higher and lower pitch cascade, respectively.

The numerical analysis continues with the two-dimensional model of the turbine which includes the examined blade, after it has been previously concluded that the conditions achieved in cascade in the experimental installation correspond to the conditions provided by the numerical model. The results obtained from a simulation of 2D water flow through the turbine with empty space behind the cascade by applying different turbulence models are compared with the measured values of pressures at the measuring points of the blade. The greatest alignment exists with the k- $\epsilon$  model thus it is applied in all further simulations because it best describes the flow through the turbine model. The highest discrepancy between the numerical and experimental results is less than 8%, except for the second measuring point which shows larger deviation.

The model was further used for the analysis of the stationary and non-stationary flow of water through the guide vanes at different runner speeds. Inlet velocity of 13,6 m/s at which maximum system efficiency will be achieved was selected after conducting an analysis.

The influence of the inlet conditions on guide vane pressure distribution was determined by comparing the loads when using different spiral casings and by comparing guide vanes with different position in relation to the stay vanes. It was concluded that the guide vane loads highly depend on the inlet conditions. The additional spiral casing was originally developed according to calculation methodology based on the Archimedean spiral centre line and the law of constant velocity moment applied on it. It was concluded that the newly developed spiral casing shows more uniform flow distribution compared to the initially considered design.

Furthermore, analysis of the influence of the runner blade position relative to the guide vane on its loads for runner speeds  $\pm 10\%$  and  $\pm 20\%$  of the nominal one in quasi-steady conditions was performed.

The impact of runner speed on the blade pressure distribution has been determined through this model. The non-stationary flow model enables the determination of pressure pulsations, i.e. consideration of dynamic loads at the different runner speeds. In unsteady flow conditions, it was firstly concluded that the guide vane inlet and outlet velocity can be taken as a constant parameter since their peak-to-peak values relative to their RMS values change in small limits (0,037-0,0465% for inlet velocity and 0,08-0,116% for outlet velocity) with the runner speed. However, the PtP value of the guide vane torque was found to be 8,6-15% which is not negligible.

In order to parametrize torque variation during time which would help predicting torque pulsations, a reduces Fourier series with sines and cosines was used. Relations were established regarding the coefficients of the series and the frequency in terms of the runner speed, Strouhal number and theoretical frequency.

The results and findings from these studies are in favour of finding a correlation with the runner speed, i.e. determining the impact of the runner speed on the pressure profile and torque - the strength condition of the blade.

Considering the guide vane pressure pulsations, they are smallest for the front point as the leading edge is further from the runner. Larger pressure changes during time at the leading edge is obtained for the higher rotating speed. Higher pressure variations are obtained on the suction side rather than the pressure side as it is more affected by the rotating runner.

Moreover, it is noted that same values of guide vane torque can be achieved at different time moments, but the guide vane pressure distribution may not be the same. This can be attributed to a possible difference in the location of the acting point (line) of the resultant hydrodynamic force.

Additionally, a three-dimensional model with the same geometry of the turbine was built in order to use it to determine the stress distribution on the blade using FSI analysis. With the help of this model, the change of the rotation axis on the guide vane loads is analysed. Nine positions of the pivot axis were considered. Different guide vane openings were numerically analysed. It was concluded that the resultant force acts between 52% and 63% of the guide vane length.

Two approaches were offered to calculate the favourable position of the rotation axis, which show a reduction of moments and, consequently, the loads under different operating conditions of the guide vanes. Using the second approach for guide vane pivot axis rotation, 15% lower torque at the opening corresponding to BEP is achieved, while first approach gives 25% torque decrement, compared to a point that was later taken as reference. Although the first approach gives more accurate results in selecting the optimal position of the rotation axis, the second approach was implemented in CFD and FEA analysis software - after redefining the openness that requires zero moment.

The most significant results in this doctoral thesis are:

- An experimental test rig has been set up for the investigation of the fluid-flow and stress conditions on a hydrofoil (blade) circular cascade;
- The experimentally obtained results of the hydrodynamic and stress characteristics of this hydrofoil in a cascade contribute to the extent of the available relevant data, having in mind the very limited research on the topic published so far;
- Using the zonal approach in the experiments, more information on the origin of the forces on the analysed hydrofoil have been gathered;
- The comparison of the experimental results from the wind tunnel and the Francis turbine guide vane water flow confirms that the same flow conditions can be achieved;
- A model is developed for determination of the forces and torques that are generated on a single hydrofoil (blade) or in a cascade (guide vane) though discretised pressure distribution;
- A calculation procedure has been defined with set criteria for determination of guide vane rotational axis position (location) with a zero-torque condition at set opening of the guide vanes;
- An original hydraulic design of the spiral casing has been developed implementing methodology based on an Archimedes' center spiral line;

- An investigation of the influence of the runner and its geometric positions in regard to the guide vanes, as well as its rotational speed on the pressure distribution has been performed;
- The mechanism of the influence of the runner rotational speed on the dynamic loads (pressure pulsations and torques) on the guide vane has been defined;
- Correlation between the pressure profile, rotational axis, and the torque on the guide vane at a specific runner rotational speed during unsteady-state analysis.

The conducted experimental research gives a broader view of the flow processes in the guide vanes, the result of which are the hydrodynamic loads - forces acting on the blades. The parametrization of the loads of a solitary aerofoil and aerofoil in a cascade performed can be used to predict the loads on an aerofoil with given geometry which is to be set in a circular cascade with certain geometric parameters. The guide vane torque parametrization can be used to predict the torque change with time for a given runner rotational speed and basic geometric parameters such as guide vane outlet radius and guide vane length.

## References

- [1] the International Renewable Energy Agency (IRENA), “Solutions to integrate high shares of variable renewable energy,” 2019.
- [2] “Renewable Energy Medium – Term Market Report 2012-2017,” Paris, 2012.
- [3] G. Baoling and B. Seddik, “Variable speed micro-hydro power plant: Modelling, losses analysis, and experiment validation,” 2018.
- [4] M. Flores, G. Uргуiza, and J. Rodriguez, “A fatigue analysis of a hydraulic Francis turbine runner,” *World J. Mech.*, vol. 2, no. 1, 2012, doi: 10.4236/wjm.2012.21004.
- [5] D. Valentin, A. Presas, M. Bossio, M. Egusguiza, E. Egusguiza, and C. Valero, “Feasibility of detecting natural frequencies of hydraulic turbines while in operation, using strain gauges,” *Sensors*, vol. 18, no. 1, 2018, doi: 10.3390/s18010174.
- [6] J. I. Perez, J. R. Wilhelmi, and L. Maroto, “Adjustable speed operation of a hydropower plant associated to an irrigation reservoir,” *Energy Convers. Manag.*, vol. 49, pp. 2973–2978, 2008.
- [7] C. Yang, X. Yang, and Y. Chen, “Integration of variable speed hydropower generation and VSC HVDC,” 2015, [Online]. Available: <https://search.abb.com/library/Download.aspx?DocumentID=9AKK10103A6095&LanguageCode=en&DocumentPartId=&Action=Launch>.
- [8] M. Valavi and A. Nysveen, “Variable-Speed Operation of Hydropower Plants: A look at the past, present and future,” *IEEE Ind. Appl. Mag.*, vol. 24, no. 5, pp. 18–27, 2018.
- [9] G. I. Krivchenko, *Hydraulic Machines - Turbines and Pumps*. Moscow: Mir publishers, 1986.
- [10] S. Katzoff, R. S. Finn, and J. S. Laurence, “Interference method for obtaining the potential flow past an arbitrary cascade of airfoils.”
- [11] J. H. Allen, “General theory of airfoil sections having arbitrary shape or pressure distribution.”
- [12] R. A. Spurr and J. H. Allen, “THEORY OF UNSTAGGERED AIRFOIL CASCADES IN COMPRESSIBLE FLOW.”
- [13] M. Bohle, “An Inverse Design Method for Cascades for Low-Reynolds Number Flow,” *ISRN Appl. Math.*, vol. 2012, p. 18, 2012, doi: doi:10.5402/2012/148607.
- [14] K. Daneshkhah and W. Ghaly, “An inverse blade design method for subsonic and transonic viscous flow in compressors and turbines,” *Inverse Probl. Sci. Eng.*, vol. 14, no. 3, pp. 211–231, 2006, doi: DOI: 10.1080/17415970500354235.
- [15] J. C. Páscoa, A. C. Mendes, and L. M. C. Gato, “A fast iterative inverse method for turbomachinery blade design,” *Mech. Res. Commun.*, vol. 36, pp. 630–637, 2009, doi: doi:10.1016/j.mechrescom.2009.01.008.
- [16] Y. Duan, Q. Zheng, and B. Jiang, “Use of computational fluid dynamics to implement an aerodynamic inverse design method based on exact Riemann solution and moving wall boundary,” *Eng. Appl. Comput. Fluid Mech.*, vol. 14, no. 1, pp. 284–298, 2020, doi: DOI: 10.1080/19942060.2020.1711812.
- [17] J. C. Dunavant and J. R. Erwin, “Investigation of a related series of turbine-blade profiles in cascade,” Washington, 1956.
- [18] G. Assassa and M. Ghany, “EXPERIMENTAL AND NUMERICAL INVESTIGATION OF THE FLOW THROUGH CASCADES,” in *SECOND A.S.A.T. CONFERENCE*, 1987,

- pp. 120–132.
- [19] G. Assassa and M. Ghany, “EXPERIMENTAL INVESTIGATION OF THE WAKE BEHIND A CASCADE OF AIRFOILS AND ISOLATED AIRFOIL,” in *SECOND A.S.A.T. CONFERENCE*, 1987, pp. 133–147.
  - [20] A. Lipej, “Numerical Prediction Of Torque On Guide Vanes In A Reversible Pump-Turbine: Turbine and pump mode operation,” *J. Multidiscip. Eng. Sci. Technol.*, vol. 2, no. 6, pp. 1616–1621, 2015.
  - [21] S. F. and J. Gregori, “Rapport I.7 Turbine guide vanes torque estimation,” Lyon, France, 1989.
  - [22] N. N. Kovalev, “The Distributor,” in *Hydroturbines, Design and Construction*, Moscow, Russia, 1961, pp. 198–259.
  - [23] S. Muntean, S. Bernad, R. Susan-Resiga, and I. Anton, “ANALYSIS OF THE GAMM FRANCIS TURBINE DISTRIBUTOR 3D FLOW FOR THE WHOLE OPERATING RANGE AND OPTIMIZATION OF THE GUIDE VANE AXIS LOCATION,” in *The 6th International Conference on Hydraulic Machinery and Hydrodynamics*, 2004, pp. 131–136.
  - [24] C. Devals, T. C. Vu, and F. Guibault, “CFD Analysis for Aligned and Misaligned Guide Vane Torque Prediction and Validation with Experimental Data,” *Int. J. Fluid Mach. Syst.*, vol. 8, no. 3, pp. 132–141, 2015, doi: <http://dx.doi.org/10.5293/IJFMS.2015.8.3.132>.
  - [25] L. Qifei, L. Guangxian, Q. Hui, W. Renben, Z. Zhengjie, and Z. Chaoben, “Experimental Study on Hydraulic Torque of Guide Vane of Pump Turbine under Turbine Working Condition.”
  - [26] B. A. Budiman, D. Suharto, I. Djodikusumo, M. Aziz, and F. B. Juangsa, “Fail-safe Design and Analysis for the Guide Vane of a Hydro Turbine,” *Adv. Mech. Eng.*, vol. 8, no. 7, pp. 1–8, 2016, doi: <https://doi.org/10.1177/1687814016658178>.
  - [27] U. Seidel, “Evaluation of RSI-induced stresses in Francis runners,” *IOP Conf. Ser. Earth Environ. Sci.*, vol. 15, no. 5, p. 052010, 2012.
  - [28] A. Zobeiri, J.-L. Kueny, M. Farhat, and F. Avellan, “Pump-turbine Rotor-Stator Interactions in Generating Mode: Pressure Fluctuation in Distributor Channel,” in *23rd IAHR Symposium - Yokohama*, 2006, pp. 1–10.
  - [29] E. Myrvold, “Numerical analysis of rotor-stator interaction in a Francis turbine guide vane,” Faculty of Science and Technology, 2017.
  - [30] C. Trivedi and M. J. Cervantes, “Fluid-structure interactions in Francis turbines: A perspective review,” *Renew. Sustain. Energy Rev.*, vol. 68, no. 1, pp. 87–101, 2017, doi: <https://doi.org/10.1016/j.rser.2016.09.121>.
  - [31] A. Laouari and A. Ghenaïet, “Predicting unsteady behavior of a small francis turbine at several operating points,” *Renew. Energy*, vol. 133, pp. 712–724, 2019, doi: <https://doi.org/10.1016/j.renene.2018.08.111>.
  - [32] C. Trivedi, M. J. Cervantes, B. K. Gandhi, and O. G. Dahlhaug, “Experimental and Numerical Studies for a High Head Francis Turbine at Several Operating Points,” *J. Fluids Eng.*, vol. 135, no. 11, p. 17, 2013, doi: <https://doi.org/10.1115/1.4024805>.
  - [33] A. KC, B. Thapa, and Y.-H. Lee, “Transient numerical analysis of rotoestator interaction in a Francis turbine,” *Renew. Energy*, vol. 65, pp. 227–235, 2014.
  - [34] X. Zhou, C. Shi, K. Miyagawa, H. Wu, J. Yu, and Z. Ma, “Investigation of Pressure Fluctuation and Pulsating Hydraulic Axial Thrust in Francis Turbines,” *Energies*, vol. 13, 2020, doi: [doi:10.3390/en13071734](https://doi.org/10.3390/en13071734).

- [35] I. Iliev, C. Trivedi, E. Agnalt, and O. G. Dahlhaug, “Variable-speed operation and pressure pulsations in a Francis turbine and a pump-turbine,” *IOP Conf. Ser. Earth Environ. Sci.*, vol. 240, 2019.
- [36] C. Trivedi, E. Agnalt, and O. Gunnar Dahlhaug, “Investigations of unsteady pressure loading in a Francis turbine during variable-speed operation,” *Renew. Energy*, vol. 113, pp. 397–410, 2017, doi: <https://doi.org/10.1016/j.renene.2017.06.005>.
- [37] F. Riegels, *Aerofoil sections-Results from wind-tunnel investigations, theoretical foundations*. London, 1961.
- [38] J. Anderson, “Aerodynamics: Some introductory thoughts,” in *Fundamentals of Aerodynamics*, 6th ed., McGraw Hill Education, 2017, pp. 19–26.
- [39] I. A. Maia and F. S. Junior, “PERFORMANCE ANALYSIS OF TYPICAL AIRFOILS THROUGH NUMERICAL SIMULATION USING FLUID-STRUCTURE INTERACTION,” 2014.
- [40] M. Babic, *Osnovi turbomashina*. .
- [41] “<https://slideplayer.com/slide/7711348/>.” .
- [42] M. Ivanoiu and S. Muntean, “Axial plane airfoil cascade. Graphics for energetical and cavitation analysis in incompressible ideal/perfect fluid,” 2009.
- [43] G. Stepanov, *Гидродинамика решеток турбомашин*. Moscow, Russia, 1962.
- [44] M. Torlak, *Hydraulic Turbines*. Sarajevo: University of Sarajevo-Faculty of Mechanical Engineering, Sarajevo, 2016.
- [45] *Spravochnik*. .
- [46] V. Gerov, *Vodni turbini*. 1973.
- [47] H. Brekke, *Ledeskovler*. .
- [48] M. Nechleba, *Hydraulic Turbines: Their design and equipment*. CONSTABLE & CO LTD, 1957.
- [49] Programme d’action PACER – Energies renouvelables, Conjoncturelles, and Office fédéral Des Questions, “Petites centrales hydrauliques Turbines hydrauliques,” 1995. doi: ISBN 3-905232-54-5.
- [50] S. Granovskiy, V. M. Malishev, V. M. Orgo, and V. M. Smolarov, *Konstrukcii i raschet gidroturbin*. 1974.
- [51] F. O. Ruud, “Stress analysis of hydraulic turbine parts,” in *Engineering monographs*, Denver, Colorado, 1962, p. 29.
- [52] A. Zobeiri, “Investigations of Time Dependent Flow Phenomena in a Turbine and a Pump-Turbine of Francis Type: Rotor-Stator Interactions and Precessing Vortex Rope,” EPFL, Lausanne, Switzerland, 2009.
- [53] B. Nennemann, T. C. Vu, and M. Farhat, “CFD prediction of unsteady wicket gate-runner interaction in Francis turbines: A new standard hydraulic design procedure,” 2005.
- [54] B. Coutu, A., Velagandula, O., Nennemann, “Francis runner forced response technology.”
- [55] E. Agnalt, “Rotor Stator Interaction in Low-Specific Speed Francis Turbines,” Norwegian University of Science and Technology, 2019.
- [56] L. Dixon and C. A. Hall, *Fluid Mechanics and Thermodynamics of Turbomachinery*. Elsevier, 2010.
- [57] A. Noshpal, *Strujnotehnicki merenja i instrumenti*. 2004.
- [58] NTNU, “Francis-99 Test Case-Experimental Study.” <https://www.ntnu.edu/nvks/f99-test-cas1>.
- [59] “CEI IEC INTERNATIONAL STANDARD 60193: Hydraulic turbines, storage pumps

- and pump-turbines – Model acceptance tests.”
- [60] “BS ISO 5168:2005 Measurement of fluid flow — Procedures for the evaluation of uncertainties.”
- [61] G. Strang, “Fourier Series and Integrals,” in *Computational Science and Engineering*, Wellesley-Cambridge Press, 2008.
- [62] A. N. Hengstler Johannes, “Influence of the Fluid-Structure Interaction on the Vibrations of Structures,” ETH Zurich, 2013.
- [63] R. S. H. V, B. F, F. M, and A. F., “Fluid structure coupling in the guide vanes cascade of a pump-turbine scale model,” *OP Conf Ser. Earth Environ. Sci.* 12, 2010.
- [64] M. J. S. Hallen, “Simulation of rotor-stator interactions (RSI’s) in a high head Francis turbine,” 2018.
- [65] M. V. Magnoli and M. Maiwald, “Influence of Hydraulic Design on Stability and on Pressure Pulsations in Francis Turbines at Overload, Part Load and Deep Part Load based on Numerical Simulations and Experimental Model Test Results,” *IOP Conf. Ser. Earth Environ. Sci.*, vol. 22, no. 032013, 2014.
- [66] “ANSYS Workbench Scripting Guide.” .
- [67] D. R. Dahal, S. Chitrakar, A. Kapali, B. S. Thapa, and H. P. Neopane, “Design of Spiral Casing of Francis Turbine for Micro Hydro Applications,” 2019, doi: doi:10.1088/1742-6596/1266/1/012013.
- [68] U. Shrestha and Y. D. Choi, “Improvement of the flow behaviour in the spiral casing of Francis hydro turbine model by shape optimization,” *J. Mech. Sci. Technol.*, vol. 34, no. 9, pp. 3647–3656, 2020.
- [69] P. R. Nakkina, K. A. Prakash, and G. S. Kumar, “A surrogate model-based method to obtain optimal design in spiral casing of Francis turbine,” *Int. J. Math. Model. Numer. Optim.*, vol. 9, no. 2, pp. 105–126, 2019, doi: DOI: 10.1504/IJMMNO.2019.098776.
- [70] P. R. Nakkina, K. A. Prakash, and G. S. Kumar, “Numerical studies on fluid flow characteristics through different configurations of spiral casing,” *Eng. Appl. Comput. Fluid Mech.*, vol. 10, no. 1, pp. 296–310, 2016, doi: DOI: 10.1080/19942060.2016.1149103.
- [71] D. J., S. V.A., A. Roghelia, and V. Chauhan, “Validation of Hydraulic Design of Spiral Casing and Stay Vanes of Francis Turbine Using CFD,” in *Proceedings of the 37th International & 4th National Conference on Fluid Mechanics and Fluid Power*, 2010, pp. 1–9.
- [72] J. Kurokawa and H. Nagahara, “Flow characteristics in spiral casing of water turbine.”
- [73] P.K.Maji and G.Biswas, “Three-dimensional analysis of flow in the spiral casing of a reaction turbine using a differently weighted Petrov Galerkin method,” *Comput. Methods Appl. Mech. Eng.*, vol. 167, no. 1–2, pp. 167–190, 1998, doi: [https://doi.org/10.1016/S0045-7825\(98\)90000-7](https://doi.org/10.1016/S0045-7825(98)90000-7).
- [74] IS7418:1991, *CRITERIA FOR DESIGN OF SPIRAL CASING (Concrete and steel)*. New Delhi, India: Bureau of Indian Standards, 2003.
- [75] M. Benishek, “Spiral Casings,” in *Hydraulic turbines*, Fluid Mech., Belgrade: University of Belgrade.

## APPENDIX

### SELECTED PAPERS PUBLISHED AT REFERENT CONFERENCES AND JOURNALS

1. M. Lazarevikj, Z. Markov, Z. Kostikj, Experimental test rig for blade passage shape influence on pressure distribution investigations, 5<sup>th</sup> International Scientific Conference COMETA 2020, Conference Proceedings ISBN 978-99976-719-8-1, pp.331-338
2. D. Babunski, M. Lazarevikj, E. Zaev, Z. Markov, “Direct tool for generation of the geometry of a Francis turbine guide vane system”, 9<sup>th</sup> Mediterranean Conference on Embedded Computing MECO 2020, DOI 10.1109/MECO49872.2020.9134214, pp.681-684
3. M. Lazarevikj, F. Stojkovski, Z. Markov, I. Iliev, O. G. Dahlhaug, Parameter based tool for Francis turbine guide vane design using coupled MATLAB-ANSYS approach, Journal of Sustainable Energy and Development, DOI: <https://doi.org/10.13044/j.sdewes.d9.0410>